NTNU
Norwegian University of
Science and Technology

Effects of Surface Treatment on Hypoeutectoid Steels and Commercially Pure Copper in a Compound Casting Process with Aluminum A356 Alloy

Aina Opsal Bakke

Chemical Engineering and Biotechnology
Submission date: June 2017
Supervisor: Yanjun Li, IMA

Norwegian University of Science and Technology
Department of Materials Science and Engineering

Abstract

Evidence of climate change has caused industries worldwide to start measures towards reducing greenhouse gas emission. The automotive industry is a large contributor to emission and has therefore demanded production of lighter, and thus less fuel-demanding, vehicles. A suggested method is by substituting steel components with aluminum alloys. However, a complete substitution is not possible as components require specific properties. As a result, the need for multi-material components arises. Compound casting is a process where strong multi-materials of complex shape can be manufactured. Bonding between aluminum and a second metal has proved difficult due to a thermodynamically stable oxide layer forming spontaneously on the aluminum surface.

In this thesis, the effects of various surface treatments on both copper and steel pipes were investigated through a low pressure die casting process. Characterizations of the aluminum-copper and aluminum-steel interfaces as result of the surface treatment were performed. Based on results from the aluminum-steel characterization, a shape casting experiment between aluminum A356 and steel inserts was conducted.

For the low pressure die cast aluminum-steel castings, bonding results improved when using galvanized steel pipes with flux coating. When using a thin zinc-layer, flux coating remained in the interface. No surface treatment caused poor bonding as oxides were entrapped. Ternary brittle $Al_{4.5}FeSi$ particles with various lengths were observed in the interface. Lengths appeared to increase with pouring temperature of the liquid melt. Heat-treated castings showed an increase in the reaction layer thickness, which included formation of a brittle Al_3Fe-layer. In the shape casting experiment, mainly mechanical bonding was achieved due to insufficient heating of the steel insert. Local metallurgical bonding was achieved at the tip of the cone-shaped steel inserts. Flux coating was deemed preferable as several pores were observed in the interface of the non-coated castings. Argon gas flushed through the mold improved bonding ability. For the low pressure die cast aluminum-copper castings, metallurgical bonding was achieved without surface treatment of the copper pipes. The interface showed formation of a eutectic Al_2Cu+(Al) structure. In addition, silicon particles were observed both in the eutectic structure and adjacent to the copper pipe. Flux coating caused poor interfacial bonding due to the formation of magnesium compounds with high melting temperatures preventing further flux reaction.

Samandrag

Auka medvit rundt klimaendringar har gjort at industrien i store delar av verda har sett i gang tiltak for å redusere utslepp av drivhusgassar. Bilindustrien, som er ein stor bidragsytar når det gjeld gassutslepp, stiller difor krav om produksjon av lettare køyrety som vil minke forbruket av drivstoff. Ein måte å oppnå dette på, er å bruke aluminiumslegeringer i staden for stål. Direkte bytte av aluminium og stål kan ikkje gjennomførast sidan komponentane må ha eigenskapar som oppnår spesifikke vilkår. Det har difor vorte nødvendig å produsere eit multi-materiale. Hybridstøyping er ein prosess der sterke multi-materiale med kompleks form kan produserast. På grunn av spontan danning av eit termodynamisk stabilt oksidlag på overflata har aluminium vanskeleg for å binde seg med andre metall.

Denne avhandlinga omfattar forsøk på effekten av ulike overflatebehandlingar på kopar- og stålrøyr gjennom ein lågtrykks presstøypingsprosess. Karakterisering av grensesjiktet som resultat av ulik overflatebehandling mellom aluminium-kopar og aluminium-stål vart gjennomført. Det vart utført eit labskala støypningsforsøk mellom A356 aluminium og stålboltar basert på resultata funne under karakteriseringa.

For lågtrykks presstøypinga mellom aluminium og stål, auka bindingsevna ved bruk av galvaniserte stålrøyr med flussmiddel. Flussmiddelet vart verande i grensesjiktet, når eit tynt sinklag vart brukt. Inga overflatebehandling førte til dårleg binding, eit resultat av at oksid vart verande i grensesjiktet. Sprø $Al_{4.5}FeSi$ partiklar, med ulike lengder, vart observerte i grensesjiktet. Lengda såg ut til å auke med aukande støypetemperatur. Breidda på reaksjonslaget auka ved varmebehandling, som også førte til danning av eit sprøtt Al_3Fe lag. Under støypingsforsøket på labskala vart mekanisk binding danna i dei fleste støypa. Dette har årsak i utilstrekkeleg temperatur i stålboltane. Tuppen av dei kjegleforma stålboltane oppnådde lokal metallurgisk binding. Sidan ein høg tettleik av porar blei funne i grensesjiktet når flussmiddel ikkje vart brukt, vil stålboltar med flussmiddel vere føretrukke. Skyljing av støypeforma med argon gass før støyping, førte til betre bindingsevne. For lågtrykks presstøypinga mellom aluminium og kopar vart metallurgisk binding danna utan bruk av overflatebehandling, og i grensesjiktet vart det då danna ein eutektisk Al_2Cu+(Al) struktur. I tillegg vart silisium partiklar observert både i den eutektiske strukturen og i nærleiken av koparrøyret. Påført flussmiddel førte til dårleg binding i grensesjiktet mellom A356 aluminium og kopar grunna danning av magnesiumsambindingar med høgt smeltepunkt som hindra vidare reaksjon av flussmiddelet.

Preface

This thesis is a continuation of the course ”TMT4500 - Materials Technology, Specialization Project”. The thesis has been carried out in collaboration with Benteler Automotive Farsund AS (BAF), the University in Agder (UiA) and SINTEF Materials and Chemistry in Trondheim as part of the ”AluLean” project. All low pressure die castings investigated were produced in Farsund by BAF. They also provided steel inserts for the lab scale shape casting experiment. Experimental work was mainly performed at the Norwegian University of Science and Technology (NTNU). The lab scale casting experiment was conducted in the SINTEF casting lab.

I would like to thank my supervisor Professor Yanjun Li for help and guidance throughout this thesis; Benteler Automotive Farsund, especially Jan Ove Løland, for providing castings and supplementary materials as well as additional helpful information; Arne Nordmark and Kurt Sandaunet at SINTEF for assistance in both preparing and executing the lab scale shape casting experiment, and additional project collaborators, in specific Geir Grasmo and Morten Onsøien, for educational discussions during project meetings. I would also like to thank Trygve Lindahl Schanche and Yingda Yu at NTNU for guidance in the metallurgy lab and the scanning electron microscope respectively. In addition, I would like to thank my family and friends for encouragements and support, especially my brother for help in proofreading.

Table of Contents

Abstract **i**

Samandrag **ii**

Preface **iii**

List of Tables **ix**

List of Figures **xi**

1 Introduction **1**
- 1.1 Motivation 1
- 1.2 Objectives 2

2 Theoretical Background **5**
- 2.1 Material Properties of Aluminum A356.0 5
- 2.2 Compound Casting 7
  - 2.2.1 Compound Casting of Aluminum-Steel 7
  - 2.2.2 Compound Casting of Aluminum-Copper 8
- 2.3 Wettability of Liquid Aluminum Alloy on a Solid Metal Surface 9
- 2.4 Diffusion and Formation of Intermetallic Phases 10
  - 2.4.1 The Binary Al-Cu System 10
  - 2.4.2 The Binary Al-Fe System 12
  - 2.4.3 The Ternary Al-Fe-Si System 13
- 2.5 Surface Treatment and Coating 14
  - 2.5.1 Removal of Oxide Layers 15
  - 2.5.2 Galvanization of Steel 15
- 2.6 Heat Treatment 17
  - 2.6.1 Heat Treatment of Bimetallic Aluminum-Steel 17
  - 2.6.2 Heat Treatment of Bimetallic Aluminum-Copper 18
- 2.7 Scanning Electron Microscopy 19

2.7.1 Energy-Dispersive X-ray Spectroscopy 19
2.8 Hardness Testing 20
2.8.1 Vickers Hardness Test 21

3 Experimental **23**
3.1 Sample Preparation 24
3.2 Optical Microscope Analysis 25
3.3 SEM Analysis 25
3.4 Vickers Micro-Hardness Testing 25

4 Low Pressure Die Casting of Steel Pipe in Aluminum A356 **27**
4.1 Materials and Process Parameters 27
4.2 Results 28
4.2.1 Effect of No Surface Treatment 28
4.2.2 Effect of Galvanization 32
4.2.3 Effect of Zinc and Flux Coating Combined 36
4.2.4 Effect of Galvanization Combined With Flux Coating 45
4.3 Discussion 54
4.3.1 Effect of Surface Treatment 54
4.3.2 Variations in Interfacial Microstructure Within a Casting 55
4.3.3 Effect of Galvanization Layer Thickness 56
4.3.4 Effect of Heat Treatment 57
4.3.5 Formation of Silicon Particles 58
4.3.6 Formation of Ternary $Al_{4.5}FeSi$ 59
4.4 Conclusions 60

5 Lab Scale Shape Casting of Steel Rod and Aluminum A356 **61**
5.1 Experimental 61
5.1.1 Steel Insert Preparation 62
5.1.2 Casting 63
5.1.3 Sample Preparation 64
5.1.4 SEM Analysis 65
5.1.5 Tempering 65
5.2 Results 66
5.2.1 Blunt Steel Inserts 66
5.2.2 Cone-Shaped Steel Inserts 72
5.3 Discussion 82
5.3.1 Effect of Argon Gas 82
5.3.2 Effect of Temperature on Blunt Steel Inserts 82
5.3.3 Gas Entrapment in the Aluminum-Steel Interface 83
5.3.4 Bonding Effect in Galvanized Cone-Shaped Steel Inserts 84
5.3.5 Bonding Effect in Galvanized Cone-Shaped Steel Inserts With Flux Coating 85
5.3.6 Effect of Tempering 86
5.4 Conclusions 87

6 Low Pressure Die Casting of Copper Pipe in Aluminum A356 89
6.1 Process Parameters 89
6.2 Results 90
6.2.1 Effect of Flux Coating 90
6.2.2 Effect of No Surface Treatment 102
6.3 Discussion 113
6.3.1 Effect of Untreated Copper Pipes 113
6.3.2 Effect of Flux Coated Copper Pipes 114
6.3.3 Effect of Heat Treatment 115
6.3.4 Formation of Silicon Particles 116
6.4 Conclusions 118

7 Overall Conclusions and Future Prospects 119

Bibliography 121

Appendix A 127

Appendix B 134

List of Tables

2.1 Compositions of alloying elements in an A356.0 aluminum alloy 5
2.2 Compositions of equilibrium Al-Cu phases formed from 350°C-500°C . . 11
2.3 Composition of ternary Al-Fe-Si phases at 550°C 14

4.1 Compositions of ST34 and ST37 steel 27
4.2 Process parameters for low pressure die castings of steel pipe in aluminum A356 28
4.3 Compositions and possible phases detected in the aluminum-steel interface in Casting 17 30
4.4 Compositions and possible phases detected in the aluminum-steel interface in Casting 32 34
4.5 Compositions and possible phases detected on the steel pipe used in Casting 16 36
4.6 Compositions and possible phases detected in the aluminum-steel interface in Casting 15 40
4.7 Compositions and possible phases detected in the aluminum-steel interface in Casting 16 43
4.8 Compositions and possible phases detected in the aluminum-steel interface in Casting 14 48
4.9 Compositions and possible phases detected in the aluminum-steel interface in Casting 28 51

5.1 Chemical composition for S355J2 steel 61
5.2 Process parameters for each lab scale shape casting 64
5.3 Results from lab scale shape casting using blunt steel inserts 66
5.4 Compositions and possible phases detected on the aluminum surface in Casting I 69
5.5 Compositions and possible phases detected in the galvanized layer of an unused blunt steel insert 72
5.6 Results from lab scale shape casting using cone-shaped steel inserts . . . 72

5.7 Compositions and possible phases in the aluminum-steel interface in a section at the steel cone tip of Casting O 75
5.8 Compositions and possible phases in the aluminum-steel interface in a section of Casting O 77
5.9 Compositions and possible phases in the aluminum-steel interface in the cone tip of Casting T 78

6.1 Process parameters for aluminum-copper low pressure die casting 89
6.2 Composition and possible phases in the aluminum-copper interface in Casting 37 93
6.3 Compositions and possible phases detected in the aluminum-copper interface in Casting 38 96
6.4 Compositions and possible phases in the aluminum-copper interface in Casting 39 100
6.5 Compositions and possible phases detected in a reaction area in Casting 43 104
6.6 Composition and possible phases detected in the reaction area-copper pipe interface in Casting 43 106
6.7 Compositions and possible phases detected in the aluminum-copper interface in Casting 44 109
6.8 Compositions and possible phases in the reaction area-copper pipe interface in Casting 44 110

7.1 Compositions and possible phases formed across the aluminum-copper interface in Casting 40 128
7.2 Compositions and possible phases formed across the aluminum-copper interface in Casting 42 130
7.3 Compositions and possible phases formed across the aluminum-copper interface in Casting 45 132
7.4 Micro-hardness measured across the interface in Casting 17. 134
7.5 Micro-hardness measured across the interface in Casting 32. 134
7.6 Micro-hardness measured across the interface in Casting 15. 135
7.7 Micro-hardness measured across the interface in Casting 16. 135
7.8 Micro-hardness measured across a section of the interface Casting 14 where the galvanized layer remained unmelted. 135
7.9 Micro-hardness measured across a section of the interface Casting 14 where the galvanized layer melted. 135
7.10 Micro-hardness measured across a section of the interface in Casting 28 where the galvanized layer melted. 135
7.11 Micro-hardness measured across the interface in Casting 37. 136
7.12 Micro-hardness measured across the interface in Casting 38. 136
7.13 Micro-hardness measured across the interface in Casting 39. 136
7.14 Micro-hardness measured across the interface in Casting 43. 136
7.15 Micro-hardness measured across the interface in Casting 44. 136
7.16 Micro-hardness measured across the interface in Casting 40. 137
7.17 Micro-hardness measured across the interface in Casting 42. 137
7.18 Micro-hardness measured across the interface in Casting 45. 137

List of Figures

1.1 The principle of metallurgical bonding 2

2.1 Binary Al-Si phase diagram 6
2.2 Examples of non-wetting and wetting between a liquid droplet and solid surface 9
2.3 The binary Al-Cu phase diagram 11
2.4 The binary Fe-Al phase diagram 12
2.5 Isothermal section of the ternary Al-Fe-Si phase diagram at 600°C 13
2.6 The binary Fe-Zn phase diagram 16
2.7 Theoretical distribution of Fe-Zn phases in a galvanized layer 16
2.8 Principle of formation of characteristic X-rays 20
2.9 Principle of Vickers hardness testing and indentation area 21

3.1 3D illustration of a compound casting produced by Benteler Automotive Farsund AS 23
3.2 Cutting pattern for low pressure die casting samples 24

4.1 Image of Casting 17 after cutting, grinding and polishing 28
4.2 Optical micrograph of the aluminum-steel interface in Casting 17 29
4.3 Micrograph of the aluminum-steel interface used for EDS analysis in Casting 17 30
4.4 Vickers hardness measured across the aluminum-steel interface in Casting 17 31
4.5 Image of Casting 32 after grinding and polishing 32
4.6 Optical micrograph of the aluminum-steel interface in Casting 32 32
4.7 Line scan across the aluminum-steel interface in Casting 32 33
4.8 Micrograph of the aluminum-steel interface in Casting 32 34
4.9 Vickers hardness measured across the aluminum-steel interface in Casting 32 35
4.10 Micrograph of the steel pipe used in Casting 16 36
4.11 Image of Casting 15 after grinding and polishing 37
4.12 Optical micrograph of the aluminum-steel interface in Casting 15 38

4.13 Line scan across the aluminum-steel interface in Casting 15 38
4.14 Micrograph of the aluminum-steel interface in Casting 15 39
4.15 Image of Casting 16 after grinding and polishing 41
4.16 Optical micrograph of the aluminum-steel interface in Casting 16 41
4.17 Line scan across the aluminum-steel interface in Casting 16 42
4.18 Micrograph of the aluminum-steel interface in Casting 16 43
4.19 Vickers hardness measured across the aluminum-steel interface in Casting 15 and 16 44
4.20 Line scan across two different sections of the steel pipe used in Casting 28 45
4.21 Image of Casting 14 after cutting, grinding and polishing 46
4.22 Optical micrograph of a section of the aluminum-steel interface in Casting 14 where the galvanized layer melted 47
4.23 Optical micrograph of a section of the aluminum-steel interface in Casting 14 where the galvanized layer remained intact 47
4.24 Micrograph of the aluminum-steel interface used for EDS analysis in Casting 14 48
4.25 Image of Casting 28 after grinding and polishing 49
4.26 Optical micrograph of the aluminum-steel interface in Casting 28 50
4.27 Micrograph of the aluminum-steel interface in Casting 28 50
4.28 Vickers hardness measured across the aluminum-steel interface for two separate interfaces in Casting 14 and an interface in Casting 28 52

5.1 Steel inserts used in the lab scale shape casting experiment 62
5.2 Casting mold used in lab scale shape casting experiment 63
5.3 Image of a broken casting with blunt steel insert 67
5.4 Images showing the aluminum surfaces from Casting E, I and K 67
5.5 Micrograph of the aluminum surface in Casting I 68
5.6 Line scan across the galvanized layer in an unused steel insert, Casting E and Casting G 70
5.7 Micrograph of the galvanized layer on an unused blunt steel insert 71
5.8 Image of Casting N, O, S and T after cutting 73
5.9 Image of the aluminum-steel interface at the cone tip in Casting O 74
5.10 Micrograph of the aluminum-steel interface in a section at the steel cone tip in Casting O 74
5.11 Image of the aluminum-steel interface at the middle of the cone in Casting O 76
5.12 Micrograph of the aluminum-steel interface in a section of Casting O . . . 76
5.13 Image of the aluminum-steel interface in the cone tip of Casting T 77
5.14 Micrograph of the aluminum-steel interface in the cone tip in Casting T . 78
5.15 Image of Casting N, O and S after tempering 79
5.16 Image of cast aluminum and steel insert for Casting N after tempering and breakage 80
5.17 Image of cast aluminum and steel insert for casting O after tempering and breakage 81

6.1 Image of Casting 37 after grinding and polishing 90
6.2 Optical micrograph of the aluminum-copper interface in Casting 37 . . . 91

6.3 Optical micrograph of a section of the aluminum-copper interface in Casting 37 . . . 92
6.4 Micrograph of the aluminum-copper interface in Casting 37 . . . 93
6.5 Image of Casting 38 after grinding and polishing . . . 94
6.6 Optical micrograph of the aluminum-copper interface in Casting 38 . . . 95
6.7 Micrograph of the aluminum-copper interface in Casting 38 . . . 96
6.8 Image of Casting 39 after grinding and polishing . . . 97
6.9 Optical micrograph of the aluminum-copper interface in Casting 39 . . . 98
6.10 Line scan across the aluminum-copper interface in Casting 39 . . . 98
6.11 Micrograph of the aluminum-copper interface in Casting 39 . . . 99
6.12 Vickers hardness measured across the aluminum-copper interface in Casting 37, 38 and 39 . . . 101
6.13 Image of Casting 43 after grinding and polishing . . . 102
6.14 Optical micrograph of the aluminum-copper interface in Casting 43 . . . 103
6.15 Micrograph of a reaction area in Casting 43 . . . 104
6.16 Micrograph of the reaction area-copper pipe interface in Casting 43 . . . 105
6.17 Image of Casting 44 after grinding and polishing . . . 107
6.18 Optical micrograph of the aluminum-copper interface in Casting 44 . . . 107
6.19 Micrograph of the aluminum-copper interface in Casting 44 . . . 108
6.20 Micrograph of the reaction area-copper pipe interface in Casting 44 . . . 110
6.21 Vickers hardness measured across the aluminum-copper interface in Casting 43 and 44 . . . 111

7.1 Image of Casting 40 and optical micrograph of the aluminum-copper interface 127
7.2 Micrograph of the aluminum-copper interface in Casting 40 . . . 128
7.3 Image of Casting 42 after grinding and polishing . . . 129
7.4 Optical micrograph of the aluminum-copper interface in Casting 42 . . . 129
7.5 Micrograph of the aluminum-copper interface in Casting 42 . . . 130
7.6 Image of Casting 45 after grinding and polishing . . . 131
7.7 Optical micrograph of the aluminum-copper interface in Casting 45 . . . 131
7.8 Micrograph of the aluminum-copper interface in Casting 45 . . . 132
7.9 Vickers hardness measured across the aluminum-copper interface in Casting 40, 42 and 45 . . . 133

Chapter 1

Introduction

1.1 Motivation

According to statistical data collected in 2010, 14.1% of total worldwide greenhouse gas emission originated in the transportation sector, making it the third largest contributor to direct emission. Out of this, 10.2% came directly from road transportation alone [1]. These numbers have increased significantly the last decades, making the European Commission request that by 2020, a 10% reduction in greenhouse gas intensity of vehicle fuels should be achieved [2]. This has led to a demand in the automotive industry to take measures towards reducing emission.

Several solutions towards emission reduction have been suggested. One possibility is to reduce vehicle weight. As the weight decreases, less fuel will be consumed thus less gas will emit. Today, steel is one of the main materials used in vehicle components. High strength combined with low material cost makes steel ideal for mass production. Despite these properties, steel mainly consists of iron, which is considered a relatively heavy material. By substituting steel with a lighter material having similar properties, vehicle weight could be significantly reduced.

Aluminum is known as one of the lightest commercially used metals. Its alloys show properties including high specific strength and good formability [3]. Therefore, it has been suggested to replace steel with aluminum alloys in vehicle production. Aluminum is also beneficial in that it can be recycled infinitely and that the recycling process requires significantly lower energy compared to the production process. However, vehicle components require specific properties and shape based on application. This can be difficult to achieve for one material alone. A necessity for producing multi-material components able to meet such criteria is thus evident. The challenge in achieving this, is that combining different materials often leads to a weak joint. Per now, there is no defined process for creating strong multi-materials and therefore there is a high demand from the automotive industry.

1.2 Objectives

The compound casting process between aluminum A356 alloy and various metals will be the focus of this thesis. In principle, liquid A356 will be cast around a different metal previously inserted in the mold. This is a commonly used method in producing multi-material components, as optimized performance and light weight can be achieved simultaneously. In general, lightweight materials are difficult to bond due to cracks or pores forming in the joint. This is often observed in welding or brazing. Compared to other joining methods, the bonding process can also be reduced in a compound casting process, due to the pre-insertion of additional materials [4].

To produce a strong bimetallic component, metallurgical bonding is necessary. Through chemical reactions and diffusion, an intermetallic layer will be able to form between aluminum A356 and a second metal. Creating a continuous boundary free of cavities, oxide films and brittle intermetallic phases will provide metallurgical instead of mechanical bonding. This will ensure strength in the joint. The principle of metallurgical bonding is shown in Figure 1.1.

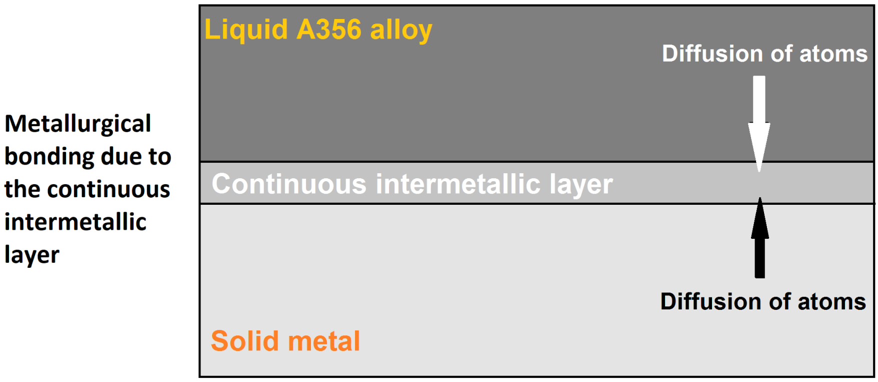

Figure 1.1: Sketch showing the principle of metallurgical bonding. Diffusion causes formation of a continuous intermetallic layer.

A challenge in compound casting with aluminum alloys, is that a thermodynamically stable oxide layer, Al_2O_3, will spontaneously form on the surface [5]. Oxide layers also tend to form on metal surfaces in general. These oxides have considerably higher melting points than the metals and alloys, and can thus hinder construction of a metallurgical bond. Therefore, the effect of different surface treatments and coatings of the metal inserts, as well as temperature variations on both liquid and solid metal will be investigated. Hardness tests will be performed on the intermetallic layers formed to determine potential brittleness.

This thesis is a continuation of the project “Effects of surface treatment in compound casting of aluminum 356.0 onto ST37 steel pipes”. In this thesis, results will be presented in three separate chapters. Further characterization of the interface resulting from low pressure die casting between steel pipes and A356 aluminum alloy will be presented in Chapter 4. Based on the findings from this characterization, a lab scale shape casting experiment between A356 and steel rods was performed. Results are presented in Chapter 5. In addition, a characterization of the interface between commercially pure copper and A356 resulting from low pressure die casting was investigated. Chapter 6 displays said findings.

Chapter 2

Theoretical Background

2.1 Material Properties of Aluminum A356.0

Cast aluminum alloys are classified based on the amount of alloying element or elements. A356.0 belongs to the 3XX.X series which has silicon and copper and/or magnesium as the main alloying elements. The fourth digit indicates if the alloy is a casting or an ingot, in this case 0 for casting. A letter in front represent a slight change in limitations of minor alloying elements compared to the 356.0 alloy [6]. Table 2.1 shows the typical compositions for an A356.0 alloy [6]

Table 2.1: Material compositions of alloying elements in an A356.0 aluminum alloy [6].

Element	Si	Mg	Cu	Fe	Mn	Zn	Ti	Others
wt%	6.5-7.5	0.25-0.45	$\leq$0.20	$\leq$0.20	$\leq$0.10	$\leq$0.10	$\leq$0.20	$\leq$0.15

From Table 2.1 it can be seen that the weight percent of silicon is much higher compared to the other elements. Silicon is a light material with several beneficial casting properties, making alloys from the 3XX.X series ideal for use in vehicle components [7]. For example, silicon will expand upon solidification and oppose shrinkage caused by aluminum, thus preventing hot cracking or tearing. Silicon is also a relatively hard material, which will increase wear resistance [8]. For casting purposes, silicon is the mostly used alloying element due to low viscosity, which increases flow of the melt and enhances ability of the mold filling [7].

With a silicon content of 6.5-7.5wt%, A356.0 alloy can be defined as a hypoeutectic Al-Si alloy as seen in the binary phase diagram in Figure 2.1 [9]. These are commonly used in the automotive industry due to higher ductility compared to hypereutectic Al-Si alloys [10]. From the blue line indicating typical silicon content in A356.0 in Figure 2.1 it can be seen that upon cooling, (Al) will solidify first followed by a eutectic composition, leaving a final structure of Al-Si eutectic distributed in aluminum grains [11]. However, formation of primary silicon particles has been reported in hypoeutectic Al-Si alloys [12]. It is suggested that upon solidification, nucleation of (Al) leaves an excessive amount of silicon in the melt. An undercooling effect from the liquid/solid interface can then cause silicon to nucleate above the eutectic temperature [10] [12].

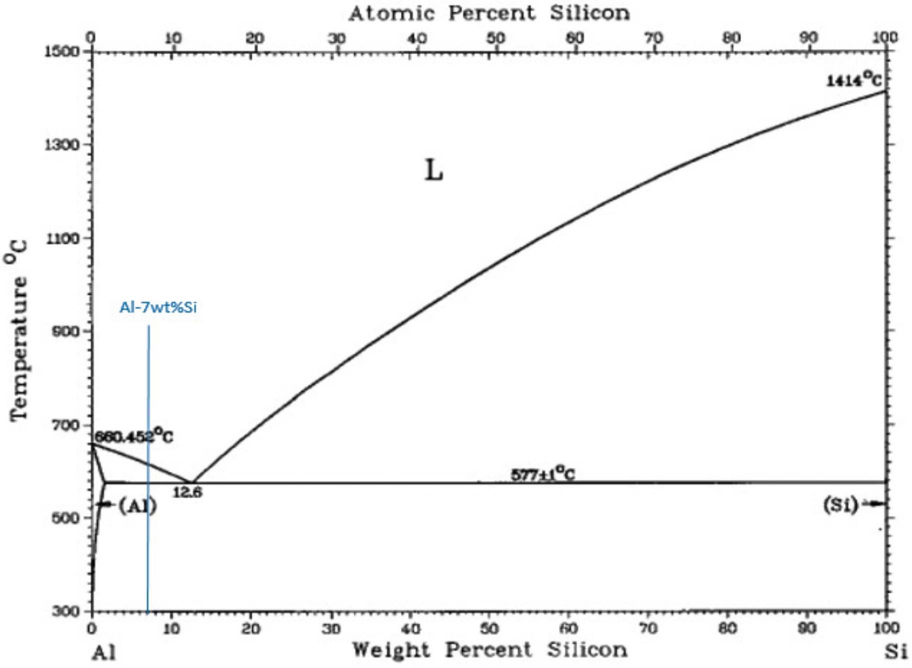

Figure 2.1: Binary Al-Si phase diagram, modified from [11]. The blue line indicates the silicon content typically found in A356.0.

Silicon does not contribute to increased strength itself. Addition of magnesium causes formation of Mg_2Si. This phase is soluble in the alloy, making it possible for precipitation hardening to occur. Strength and hardening is then achieved without significantly reducing ductility [8]. The magnesium and silicon content also enables the alloy for subsequent heat treatment, by which improved strength can be achieved. This makes A356.0 alloy widely used in the automotive industry. Magnesium is in addition often used as an alloying element, as it contributes to corrosion resistance and machinability [7].

2.2 Compound Casting

The casting process is a manufacturing method that has been used for centuries. In principle, casting consists of pouring liquid metal into a mold. The metal is left to solidify in the mold, thus producing a cast component [4]. As the mold is formed based on desired design, it is possible to produce complex shapes that otherwise would be difficult.

Compound casting shares the same principle as the casting process. They differ, however, in that for compound casting two different materials are cast together. One of the materials is a solid component which is inserted into the mold prior to pouring the other liquid material. The goal is to achieve a continuous metallic transition zone between the two materials. This often occurs due to a diffusion reaction zone forming [4]. When the casting solidifies, a multi-material component with varying specific properties is formed.

2.2.1 Compound Casting of Aluminum-Steel

Joining aluminum and steel could provide high advantages in the automotive industry. However, differences in mechanical properties, melting temperature and formation of brittle intermetallic phases, has made joining of aluminum and steel difficult [13]. Iron has a melting point of 1535°C, which compared to 660°C of aluminum, is more than twice as high [14]. Although the melting point of steel is somewhat lower than pure iron, it will still be significantly higher than the liquidus temperature of the A356.0 alloy, which is 615°C [15]. Several experiments on compound casting of aluminum and steel have been executed.

In 2014, Jiang, Fan and C.Li conducted an experiment with compound casting of aluminum ZL114A, which has a similar composition to A356, and structural carbon steel [16]. Three different surface treatments were used on the steel inserts; hot-dip aluminizing in ZL114A, 10% ammonium chloride surface modifier and a combination of the two. In addition, an untreated sample was cast for comparison. Results showed small cavities existing in the interface of the aluminized sample. These were macroscopically visible, but significantly smaller than observed in the untreated sample. Using a coating surface did not lead to any gap formation. However, micrographs displayed no development of a reaction layer and mechanical tests showed no significant improvement in shear stress, suggesting only mechanical bonding. Combining both surface treatments led to formation of a reaction layer as well as a 40% increase in shear stress compared to the untreated sample. Thus it was concluded that using a coating layer could help remove oxides, which would cause enhanced diffusion and formation of a metallurgical bond in the aluminized layer.

Jiang, Fan, G.Li and C.Li published another article in early 2016 on compound casting of aluminum ZL114A onto structural steel inserts [17]. Wettability between aluminum and steel was investigated using a cleaned steel pipe and a steel pipe coated with a thin zinc layer containing 0.1wt% Ni. Castings using zinc-coated steel showed a relatively continuous interface, free of gaps and voids. In addition, significantly higher shear stress was achieved when using zinc-coated steel, indicating formation of a metallurgical bond. Without coating, gaps were observed and no intermetallic reactions had occurred. Jiang et al. concluded that the zinc coating increased wettability between the liquid aluminum and the steel surface. It was also suggested that using temperatures of the poured ZL114A melt above the melting point of zinc enhanced formation of intermetallic phases.

2.2.2 Compound Casting of Aluminum-Copper

Due to the high electrical and thermal conductivity of copper and the light weight and low density of aluminum, a copper-aluminum bimetal could reduce both weight and cost compared to an Al-Cu alloy without significantly reducing conductivity [18]. However, as copper and aluminum have high affinity towards each other, brittle intermetallic phases with high electrical resistance usually form in the interface [18]. Compound casting of aluminum and copper has been studied in recent years due to lower process costs and less dimensional restrictions. These have been the main challenges in various welding processes [19].

In 2009, Divandari and Golpayegani made compound castings of A356 alloy and copper wires, using the lost foam casting method [20]. Wires were inserted into a polystyrene pattern which filled the mold cavity. This polystyrene pattern melted as liquid metal was poured into the mold, producing a copper-A356 bimetallic casting. Wires with diameters of 0.4, 0.8 and 1.2mm were compared. The thinnest wire completely melted and only a small area of Al-Cu phases was observed. Increasing the diameter to 0.8mm resulted in partial melting of the wire. In this case, several intermetallic compounds formed. From the copper wire towards the aluminum matrix, AlCu, Al_2Cu particles and Al_2Cu + Al eutectic phase were distinguished. In addition, primary silicon particles were observed on the copper surface and in the matrix. These particles were also found on the copper surface using a 1.2mm wire diameter, even though no melting of the wire was observed. It was concluded that the formation of silicon particles most likely was due to the cooling effect of the copper wire.

A more recent experiment was published by Liu et al. in 2015 [18]. They achieved sound metallurgical bonding between commercially pure aluminum and copper when thermally spray coating the copper surface with a thin zinc layer. Several intermetallic phases were found in the reaction layer, including Al_4Cu_9, Al_2Cu, Al-Cu eutectic and Cu-rich Al solid solution. An uncoated sample made for comparison, showed only mechanical bonding. In addition, the effect of pouring temperature and applied pressure was investigated by varying the parameters from 680°C to 740°C and 30MPa to 110MPa respectively. Zinc did not melt at the lower temperatures, whereas the reaction layer increased in thickness as the temperature elevated. As both temperatures would be detrimental to bonding, a pouring temperature of 700°C was found to be ideal. Liu et al. also found that the only noteworthy difference with change in applied pressure, was a slight decrease in electrical resistance as the pressure increased.

2.3 Wettability of Liquid Aluminum Alloy on a Solid Metal Surface

Wettability is in this thesis defined as the ability a liquid has to spread on a solid surface. This is an important aspect in the compound casting process, as contact between the liquid and solid material will be crucial for interfacial reactions and thus for metallurgical bonding to occur [21]. Wettability is often measured using a sessile drop method, where a liquid droplet is placed on a solid surface. The contact angle between the liquid droplet and solid surface is then studied over time to determine wettability. Contact angles of less than 90° indicate wetting, with complete wetting being achieved at 0° [22]. Figure 2.2 shows sketched examples of wetting and non-wetting.

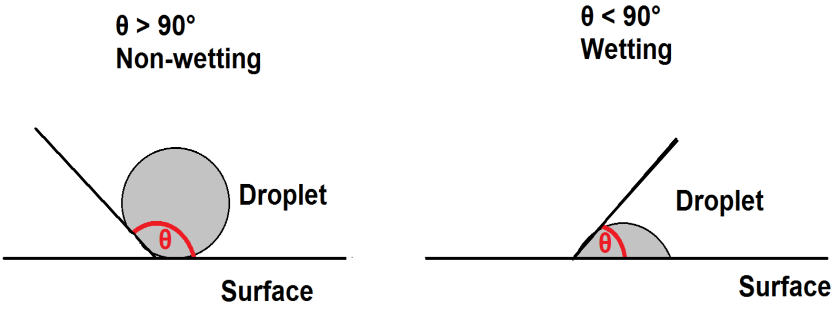

Figure 2.2: Examples of non-wetting and wetting, from left to right respectively, between a liquid droplet and solid surface. The sketch is based on a figure in [22].

Good wettability between a liquid and a solid metal can be achieved if a reaction occurs at the interface. Optimally, both surfaces need to be active participants in the reaction [22]. Al_2O_3 is as mentioned a thermodynamically stable oxide layer, implying low wettability with metallic melts. This is in general the case for oxide layers, as they are considered passive substrates [21]. In a compound casting process, oxide layers might exist on both the liquid and the solid surface. This will significantly reduce wettability and formation of a metallurgical bond. Wetting between aluminum and copper might be difficult to achieve, as oxides will form on the copper surface if exposed to air. The thickness of this oxide layer will increase with increasing temperature [23].

Oxide formation is also an important issue in the hot-dip galvanization process. As shown by Kawano and Renner, a bare iron sample obtained complete wetting by a Zn-Al liquid, whereas a similar liquid on an Al_2O_3 surface was non-wetting [24]. This is due to the bare iron surface being a reactive substrate, thus enhancing spreading and wettability of the liquid. Another important parameter affecting wettability, is temperature. A temperature increase of a solid metal substrate was found to improve the contacting conditions with a liquid droplet [25]. This will provide enhanced wettability, as activity and mobility will increase and activate the surface. Higher mobility also means that there will be an elevation in diffusion and formation of a boundary layer can more easily occur. Wettability speed will therefore also be affected by temperature.

2.4 Diffusion and Formation of Intermetallic Phases

In order to achieve metallurgical bonding between the compound cast materials, a diffusion zone must develop [4]. Diffusion is a function of concentration gradients. For two materials in contact at elevated temperatures, loosely bound atoms will migrate from high concentration areas to low concentration areas. This will create an interdiffusive layer with varying concentrations. How far an atom can migrate into another material, is determined by the diffusion coefficient. The diffusion coefficient is much larger in liquid than solid phase. Therefore, atoms in a liquid will diffuse into a solid and form a diffusion layer on the surface. However, when casting with high temperature liquids, it is believed that some surface atoms of the solid also will loosen from their lattice and diffuse into the liquid [26].

Diffusion is highly dependent on temperature, and will increase with elevation [26]. Based on the process parameters of a casting, the temperature dependency allows formation of several intermetallic phases. These phases will have varying compositions depending on where in the diffusion layer they are formed. Brittle intermetallic phases will create weak bonds and are thus unwanted. Knowledge about formed intermetallic phases is therefore crucial. In compound casting between A356 and steel, most of the intermetallic phases belong to the Fe-Al and Fe-Al-Si systems. Despite excessive research on the ternary Al-Si-Cu system, no ternary phases have been precisely distinguished [27]. Therefore, the binary Al-Cu system will be the most important between A356 and copper.

2.4.1 The Binary Al-Cu System

The binary Al-Cu system is quite complex and several intermetallic phases can form over a variety of temperatures. This can be seen in the binary Al-Cu phase diagram in Figure 2.3. In total, eight intermetallic phases are found in the system. A few of these phases will only form at high temperatures. Phases with similar Greek letter designation have similar compositions. However, as shown by the subscripts, they can have different crystal structures [28]. Table 2.2 shows the Greek letter designation and compositions of five equilibrium phases formed between 350°C and 500°C [29] [30].

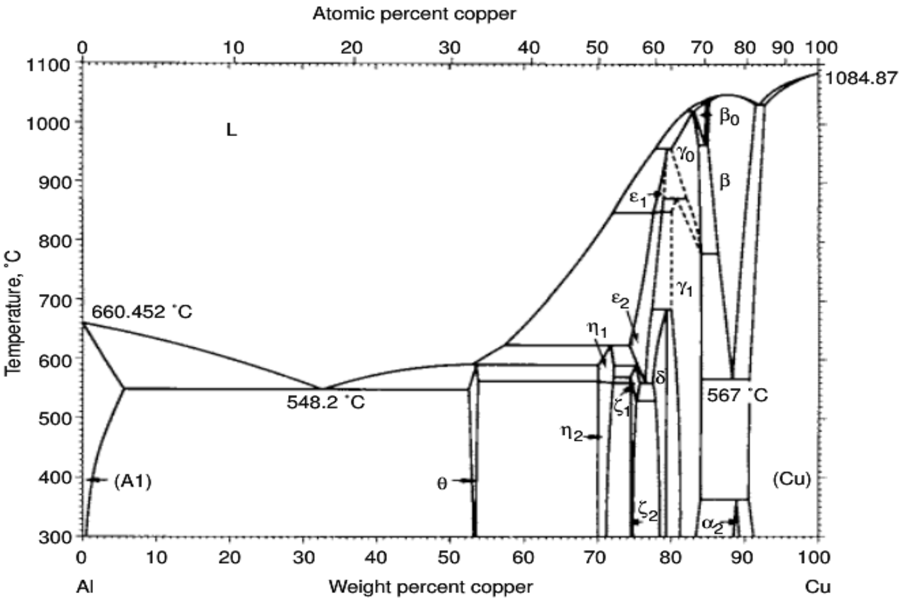

Figure 2.3: The binary Al-Cu phase diagram, captured from [28]. Greek letters indicate intermetallic phases, whereas subscripts show that similar compositions can have different crystal structures.

Table 2.2: Compositions of five equilibrium Al-Cu phases formed between 350°C and 500°C [29] [30].

Phase	Composition
θ	Al_2Cu
η	AlCu
ζ	Al_3Cu_4
δ	Al_2Cu_3
γ	Al_4Cu_9

In contact with liquid aluminum, copper atoms will start dissolving and form a zone with hypereutectic composition close to the copper surface. It is believed that the θ-phase will nucleate first due to its relatively small unit cell compared to the other intermetallic phases [30]. As temperature reaches 548°C, a eutectic structure consisting of Al_2Cu and (Al) will form, as seen in Figure 2.3. Al_2Cu formed on the copper surface will prevent further diffusion of copper into the liquid aluminum [31]. Between Al_2Cu and the copper surface however, copper atoms will continue to diffuse after solidification, causing formation of other intermetallic phases through a solid state phase transformation [30]. As diffusion is temperature dependent, other intermetallic phases formed will vary with both temperature of the liquid aluminum and potential preheating of the solid copper.

As previously mentioned, copper and aluminum have high affinity towards each other, especially above 120°C [30]. This causes formed intermetallic phases to have high bonding energy and a low number of free electrons, making them brittle with high electrical resistivity [32]. To achieve optimal mechanical properties, a thin intermetallic layer is therefore necessary.

2.4.2 The Binary Al-Fe System

Aluminum and iron are the main elements present in the interface between A356 and steel. Therefore, the likelihood of intermetallic Fe-Al phases forming is significant. From the binary Fe-Al phase diagram in Figure 2.4 it can be seen that five intermetallic phases can form between aluminum and iron. FeAl, Fe_3Al, $FeAl_2$, Fe_2Al_5 and $FeAl_3$.

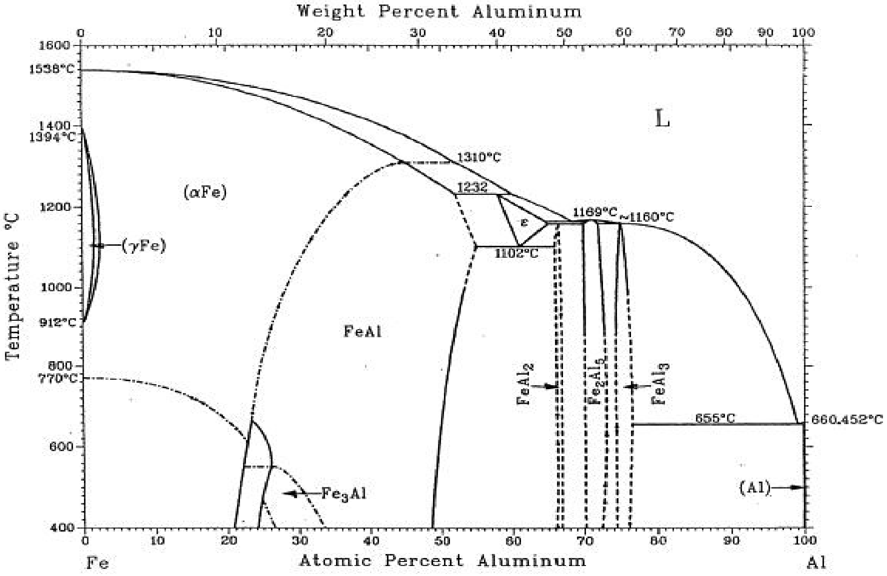

Figure 2.4: The binary Fe-Al phase diagram, captured from [33].

Several experiments have been performed to determine the growth of intermetallic phases between iron and aluminum. When aluminum is in liquid state, it has been found that the growth of Fe-Al phases is dependent on the diffusion of iron atoms. Iron, being solid, will have a much lower diffusion coefficient, causing formation of aluminum-rich phases [34]. Between 550°C and 944°C, formation of Fe_2Al_5 is reported to dominate the reaction layer [35]. This phase grows towards steel with a characteristic tongue-like morphology [35].

In the temperature range between 700°C and 900°C, formation of $FeAl_3$ has been detected between aluminum and the intermetallic Fe_2Al_5 phase [36]. This confirms the formation of aluminum-rich phases at lower temperatures. FeAl and Fe_3Al are formed when high process temperatures are used [34], due to an increase in diffusion of iron atoms at elevated temperatures. These iron-rich phases are more desired, as the increased iron content improves wear resistance and specific strength. $FeAl_2$, Fe_2Al_5 and $FeAl_3$ are considered brittle phases, and are thus unwanted in the interface [34].

2.4.3 The Ternary Al-Fe-Si System

Silicon is often added to reduce the reaction layer between aluminum and iron, and is therefore a commonly used alloying element in the aluminizing process [35]. A thinner reaction layer ensures higher bonding strength, as intermetallic phases often are brittle. Thick reaction layers would therefore significantly weaken the overall component. An addition of 2.5wt% silicon has proved to reduce boundary layer thickness by approximately half compared to pure aluminum. However, exceeding 10wt% silicon will not provide as significant reduction. Silicon is also added to flatten the interface, as irregularities are more susceptible to cracking [37].

In total, eleven intermetallic ternary Al-Fe-Si phases have been distinguished [35]. As seen in the complex ternary phase diagram in Figure 2.5, it is difficult to separate them as they have fairly similar compositions [38]. Table 2.3 provides the Greek letter designation and composition of the ternary intermetallic phases stable at 550°C [39]. It can be seen that τ_1 and τ_9 have identical compositions and are therefore commonly referred to as the τ_{1-9}-phase [39].

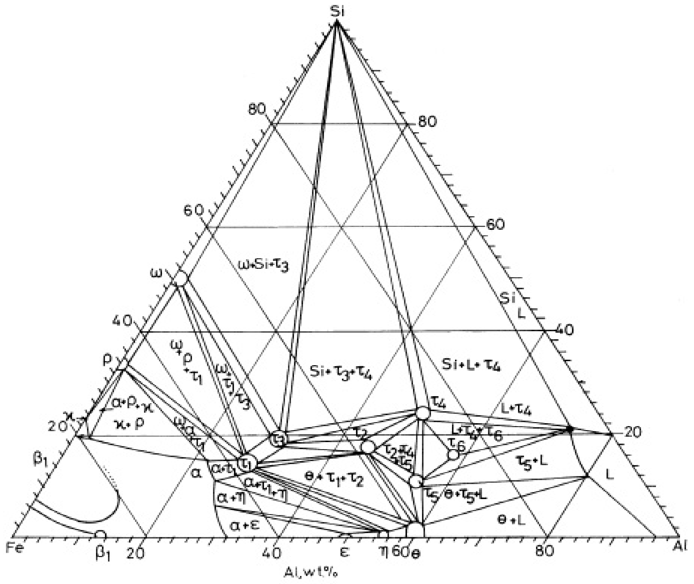

Figure 2.5: Isothermal section of the ternary Al-Fe-Si phase diagram at 600°C, captured from [38]. Intermetallic phases are designated by Greek letters.

Table 2.3: Composition of stable ternary Al-Fe-Si phases at 550°C [39].

Phase	Composition
τ_1	$Al_2Fe_3Si_3$
τ_2	Al_3FeSi
τ_3	Al_2FeSi
τ_4	Al_3FeSi_2
τ_5	$Al_{7.4}Fe_2Si$
τ_6	$Al_{4.5}FeSi$
τ_7	$Al_3Fe_2Si_3$
τ_8	$Al_2Fe_3Si_4$
τ_9	$Al_2Fe_3Si_3$
τ_{10}	$Al_{57-59}Fe_{24-25}Si_{17-18}$
τ_{11}	$Al_4Fe_{1.7}Si$

Under normal cooling conditions the dominant Al-Fe-Si phases forming are τ_5 and τ_6. In addition, if magnesium is present in a sufficient amount, the quaternary π-phase ($Al_8FeMg_3Si_6$) might form [40]. The formation of ternary phases has been studied in the aluminizing process. An addition of 2.5wt% silicon was reported to cause formation of τ_{1-9} in the $FeAl_3$/Fe_2Al_5 interface as well as both cubic and hexagonal τ_5 forming in a reaction layer adjacent to the aluminum. As the silicon content was increased to 5wt% formation of the eutectic τ_6-phase was also observed in the interface [37].

Eutectic τ_6 will form with a platelet structure, which will cause high internal stresses in the interface [41]. This will be detrimental to the mechanical strength in addition to the structure increasing the possibility of crack propagation. Ultimate tensile strength and percent elongation have shown significant reduction with increasing length of τ_6 particles up to 70μm. Further growth showed only a slight reduction [42]. Several methods are suggested to reduce density and growth of the τ_6 particles. Addition of manganese has led to the formation of quaternary $Al_{15}(Fe, Mn)_3Si_2$, which will be less detrimental than τ_6 due to its more equiaxed structure [43]. Modification of cooling rates proved to affect density of τ_6, where increasing cooling rates lead to less formation of the ternary phase [42].

2.5 Surface Treatment and Coating

Alumina, the thermodynamically stable oxide layer that spontaneously forms on the aluminum surface, has a melting point of 2054°C [14]. This is significantly higher than temperatures used in an aluminum casting process. It is also assumed that oxide layers will form both on the steel and the copper surface. The melting points of copper and iron oxides are also considerably higher than commonly used process parameters [14]. Therefore, surface treatment and/or coating of the metal surface will be necessary to avoid the formation of oxide layers and thus achieve metallurgical bonding.

2.5.1 Removal of Oxide Layers

Before coating can be applied to a metal surface, the oxide layer must be removed in order to obtain optimal properties. A common method for cleaning oxide layers off a surface is sandblasting. In this process, sand particles are projected onto a surface using compressed air. Silica is often used, due to a relatively uniform particle size as well as sharp-edged grains. Mechanical properties will remain intact in the process [44].

Oxide layers can also be removed through chemical reactions, called a pickling process. In principal, a chemical solution is applied to the surface, in which a reaction occurs to clean the surface from oxide layers and other contaminants. The chemical solution is mainly acidic, where low alloyed steels often are treated with hydrochloric or sulfuric acid. A disadvantage with this process is that hydrogen from the acids can react with the surface, causing hydrogen embrittlement and making it more exposed to cracks [45].

Chemical solutions applied to a metal surface can also increase wettability and promote reaction in contact with a liquid metal with an oxide layer [16]. Therefore, addition of a chemical solution, sometimes designated as flux coating, might be beneficial towards removing contaminants in a reaction layer. This can ensure proper bonding. Flux coatings usually have lower liquidus line compared to solidus line of the metal. Thus, the flux will melt at lower temperatures and spread across the surface. This will lead to an activation of the flux, so that oxide removal can occur in addition to further prevention of oxidation [46].

For aluminum, flux containing potassium aluminum fluoride has been reported to be beneficial in terms of removing surface oxides. However, in using aluminum alloys with a certain magnesium content, it was found that magnesium will react with the flux. Upon reaction both formation of K_2MgF_4 and MgF_2 were observed [47]. As K_2MgF_4 and MgF_2 have higher melting points than the flux, the ability of the flux to remove surface oxides will be severely reduced. As a suggestion, cesium has been added to the flux. Cesium will more easily react with magnesium and form $CsMgF_3$ and/or $Cs_4Mg_3F_{10}$. These compounds have lower melting points than the flux, and will therefore not intervene with its efficiency [48].

2.5.2 Galvanization of Steel

Galvanization of steel has primarily been used for corrosion protection. This is due to zinc being more electronegative than steel, and will thus work as a sacrificial anode in aqueous solutions [49]. Zinc has also proved to have a positive effect on wettability [17]. In addition, zinc has a relatively low melting point of 420°C [14], which can be beneficial in achieving metallurgical bonding in a compound casting process using steel. Galvanization is often performed through a hot-dip process where steel is dipped in liquid zinc after a surface cleaning process. Zinc atoms will then diffuse into the steel, and vice versa, creating intermetallic phases between the two and thus a protective layer [50].

The intermetallic phases forming between zinc and iron are solemnly based on diffusion [51]. Therefore, several factors might affect the galvanized layer. Increased temperature and time in the bath will increase the diffusion rate, causing a thicker layer to form. Alloying elements are often added to the liquid zinc bath. Low amounts of aluminum are for instance added to prevent formation of intermetallic phases, leading instead to a thin galvanized layer [52]. In addition, the composition of the steel being galvanized will also affect the final layer. An increase in silicon concentration will produce a thicker layer. However, in the concentration range from 0.03wt%-0.14wt% silicon, known as the Sandelin range, the reaction rate is high causing an uncontrollable growth of the galvanized layer [50]. Intermetallic phases in the binary Fe-Zn system are given in the phase diagram in Figure 2.6 [9]. The theoretical distribution of phases formed in a galvanized layer are presented in the following Figure 2.7 [53].

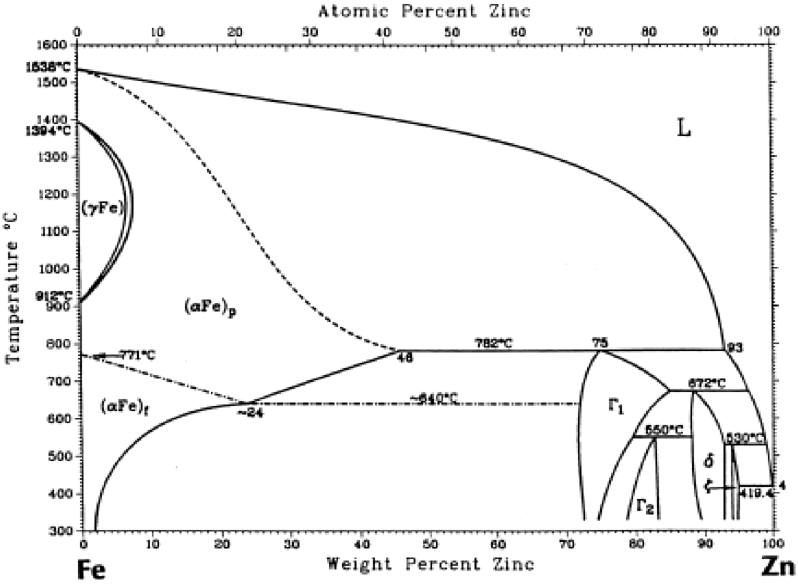

Figure 2.6: Binary phase diagram of Fe-Zn, captured from [9].

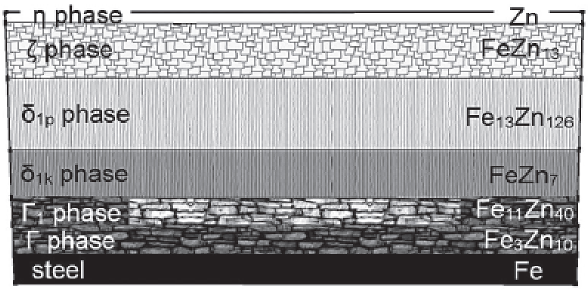

Figure 2.7: Theoretical distribution of Fe-Zn phases in a galvanized layer, captured from [53].

From Figure 2.6 and Figure 2.7 it can be seen that theoretically five intermetallic phases will develop. The ζ-phase, having the highest zinc content, will form first during the hot-dip process. Subsequently, crystals with δ_1 composition will start developing. As this layer grows, a barrier will develop preventing further growth of ζ. The same process will be repeated with the following Γ-phase [53]. These phases differ in both iron content and crystal structure. ζ has a base centered monoclinic structure, whereas δ_1 has a hexagonal crystal structure. Γ_1 and Γ have FCC and BCC respectively [51]. These differences led Okamoto et al. to conclude that while ζ and Γ are relatively ductile phases, δ_1 and Γ_1 are brittle, making a thick galvanized layer unwanted [49].

2.6 Heat Treatment

Aluminum alloys have specific mechanical requirements based on application. To meet these specifications, thermal treatments can be used. Heat treatment is a collective term on processes where temperature modification is used to achieve specific properties for an alloy. Through elevation of temperature it is possible to increase hardness and strength, improve machinability and wear resistance, and relive residual stress [54]. For cast aluminum alloys, a common method includes solution heat treatment followed by quenching and precipitation hardening. The final process step is also known as aging. This combination is designated as T6 heat treatment [54].

A356 is, as previously mentioned, heat treatable due to formation of the hardening Mg_2Si phase during aging. Both ultimate tensile strength and yield strength will increase as a result of Mg_2Si precipitating [55]. Quenching rate, magnesium content and silicon size and structure were found to have great influence on the final mechanical properties. Upon solution heat treatment, magnesium and silicon will dissolve in the aluminum matrix and create a super-saturated solid solution [56]. During this process, eutectic silicon will spheroidize and coarsen depending on the length of the treatment. This will affect ductility, as large brittle particles are more prone to cracking [57]. After the solution heat treatment, the alloy is quenched. Quenching rate will be critical for later precipitation of Mg_2Si. During quenching, vacancies will form in the super-saturated solid solution. These vacancies will later become precipitation sites, and thus determine the density of the hardening Mg_2Si phase [56] [57]. Magnesium content will also affect the amount of hardening phase. A concentration of less than 0.3wt% Mg shows little change after the T6 treatment, as less Mg_2Si will precipitate [58].

2.6.1 Heat Treatment of Bimetallic Aluminum-Steel

Steel is subjected to heat treatment to obtain higher strength and a finer grain structure. This is mainly done by heating the steel to temperatures above 723°C, in which transition into an austenitic structure occurs [7]. As this temperature is above the melting point of the A356 alloy, no significant strength increase can be expected in steel by applying the T6 heat treatment on a bimetallic aluminum-steel component.

Effect of solution heat treatment on a bimetallic plate of A356 and low carbon steel was investigated by Zhe et al. in 2011 [59]. They found that increasing treatment time from 3 to 40 hours lead to an increase from two to four reaction layers as well as a significant enlargement of the reaction zone thickness. Temperature variations did not show any noteworthy effect on morphology of the reaction layers. However, elevation in temperature led to growth of the interface. Similar observations were made by Springer et al. [35], where the interface between bimetallic aluminum-steel and Al5Si-steel components were investigated after annealing. For aluminum-steel the reaction zone grew from 1.9μm to 13.6μm as the temperature increased from 450°C to 600°C. Growth of the reaction zone in the Al5Si-steel component was not as noteworthy. Nonetheless, for both components the heat treatment resulted in a thicker reaction zone. This will be unfavorable for the component due to brittle intermetallic phases being more prone to cracking.

An additional observation reported in both experiments, was formation of Kirkendall voids in the interface between aluminum and the adjacent reaction layer [35] [59]. Kirkendall voids are vacancies or pores that can form in a multi-material component due to different diffusivity of the elements involved [60]. Zhe et al. explained this effect as a result of the dominant reaction layer (Al_5Fe_2) causing aluminum atoms, having higher diffusivity than iron, to diffuse to the Al_5Fe_2/Fe front. This will leave voids in the interface between aluminum and the adjacent reaction layer. As the void concentration grows, the contact surface between the aluminum and the reaction layer will decrease and cause a significant reduction in bonding strength [59].

2.6.2 Heat Treatment of Bimetallic Aluminum-Copper

Aluminum-copper alloys are often subjected to solution heat treatment, forming the hardening Al_2Cu-phase in the same manner as mentioned for Mg_2Si [54]. Commercially pure copper however, is not prone to any heat treatment as no hardening phases will form. However, several experiments have been performed to observe the effect of heat treatment on bimetallic aluminum-copper sheets. No research was found on heat treatment of cast aluminum-copper.

Cheng and Weng reported that for an aluminum clad copper sheet, the reaction zone increased from 1.4μm at 300°C to 18μm at 500°C [61]. The latter had a distinguishable four-layer structure, determined as Al_2Cu, AlCu, Al_3Cu_4 and Al_4Cu_9 from aluminum to copper respectively. In a similar experiment, Cheng et al. performed peel tests on aluminum-copper sheets [62]. These tests showed that as the annealing temperature exceeded 400°C, the fracture surface transformed from ductile to brittle. This was concluded to be a result of the increased thickness of the reaction zone, especially the brittle intermetallic phases AlCu and Al_3Cu_4.

Lee, Bang and Jung found that the increased reaction zone thickness due to annealing, lead to a significant decrease in electrical conductivity. Upon tensile testing, the fracture site moved from the heat-treated aluminum to the reaction layer as the thickness increased [63]. However, Sheng et al. reported that a low temperature heat treatment at 423K for two hours caused a smooth transition in the aluminum copper interface, without any evident transition layer. Increasing temperature and time weakened the bonding strength due to the growth of a transition layer. In addition, small Al_2O_3 particles precipitated along the interface between aluminum and the adjacent reaction layer at high temperatures. These were deemed to have no harmful effect on the bonding strength, but could potentially be detrimental if the density increased [64].

2.7 Scanning Electron Microscopy

To investigate the formation of a diffusion boundary and a possible intermetallic zone between materials in a compound cast, use of a high magnification microscope is necessary. Optical microscopes often do not offer high enough magnification to observe all wanted characterizations. Instead, a scanning electron microscope (SEM) can provide high resolution images down to approximately 1nm-10nm [65].

SEM uses a thin, focused electron beam to scan a sample. As electrons are used, the microscope is highly beneficial for metallic samples as they already are conductive materials. It is however important that the sample surface is free from oily contaminants, as this can affect both aperture and sample. When the electron beam swipes the sample, several different signals are emitted. These include secondary electrons, backscattered electrons, characteristic X-rays, Auger electrons and photons of various energies [66].

Secondary and backscattered electrons are the signals most used to produce an image, also known as a micrograph. Secondary electrons (SE) will gradually lose their kinetic energy when escaping the sample, leading to an inelastic scatter of electrons detected by the detector. This inelasticity allows secondary electrons to provide topographical contrast in the image [65]. Backscattered electrons (BSE) are primary electrons which are elastically scattered at angles exceeding 90°. These electrons are highly dependent on the atomic number of a sample. Increasing the atomic number leads to ejection of more backscattered electrons. In the micrograph, brightness will increase as the atomic number of the element increases [66].

2.7.1 Energy-Dispersive X-ray Spectroscopy

Energy-dispersive X-ray spectroscopy, also known as EDS, is a method used in the SEM to characterize elements found in a sample. In principle, a primary photon can have high enough energy to cause an electron in the specimen to excite from its shell, thus leaving a vacancy. To regain its low-energy state, another outer-shell electron will fill the vacancy and in the process, eject a photon [66]. Figure 2.8 shows a sketch of this principle.

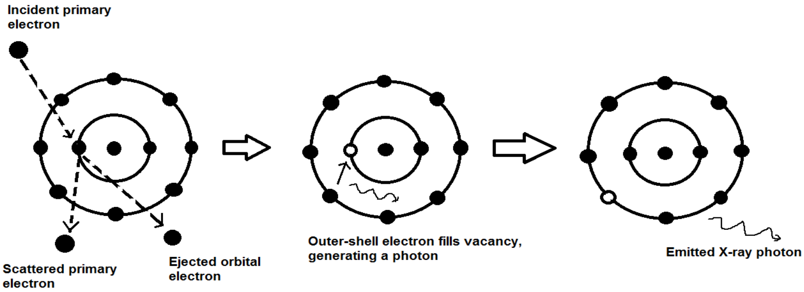

Figure 2.8: Sketch showing the principle of formation of characteristic X-rays. The sketch is based on a figure found in [66].

The photons emitted will have characteristic energies. These energies depend on which electron shells the electron transition occurs between, as well as in what element the photon is emitted. Detecting these energies can give basis for making an X-ray spectrum where sample elements can be identified through known energy peaks. During EDS, X-rays pass through a thin window, often made of beryllium, into a silicon crystal detector. From this detector, the energies are converted into signal pulses which can be read by a computer, thus producing an X-ray spectrum [67]. However, EDS has a disadvantage when it comes to elements with atomic numbers lower than 11 [66]. This is due to the beryllium window absorbing low energy photons, preventing them from reaching the detector [67].

2.8 Hardness Testing

The term hardness has a variety of definitions based on what field of work it is used in. On a general basis, it can be defined as a material's resistance towards deformation [68]. Therefore, hardness testing has been used as a way of determining a materials toughness. A variety of hardness tests are available. The most commonly used are static indentation tests where a force is applied by an indenter on the material. Ratio between the force applied and the area of the indentation determines the hardness [69]. Rockwell, Vickers and Brinell are the most common static indentation tests.

An advantage with hardness tests is that they can be performed on both macro- and microscale. Micro-hardness tests are performed with loads under 1kgf. These are usually used if higher precision is required or the test piece is too small for macro-testing [70]. Even though hardness is determined by applied force and indentation area, it is considered a reference value scale. Indenter shape, applied force and holding time of force need to be specified for hardness measurements. This means that hardness values using Vickers cannot be compared to those of Brinell or Rockwell without further specification [69].

Several properties of a material can be determined based on hardness. For instance, experiments have shown that hardness is proportional to tensile strength, and can therefore also be related to the yield strength of a material [71]. In addition, hardness is higher for alloys than pure metals because of bonds forming between dissimilar atoms. These have higher strength compared to the pure metal bond and thus cause alloys to be more resistant to deformation. Grain size also affects hardness, where hardness increases with reduced grain size [69].

2.8.1 Vickers Hardness Test

The principle of a Vickers hardness test is to apply load on a square pyramid-shaped indenter with an angle of 136° between two opposing faces. The indenter is made of diamond which allows hardness detection of all materials [70]. Figure 2.9 shows the principle indentation mark made in a material and quantities measured thereafter.

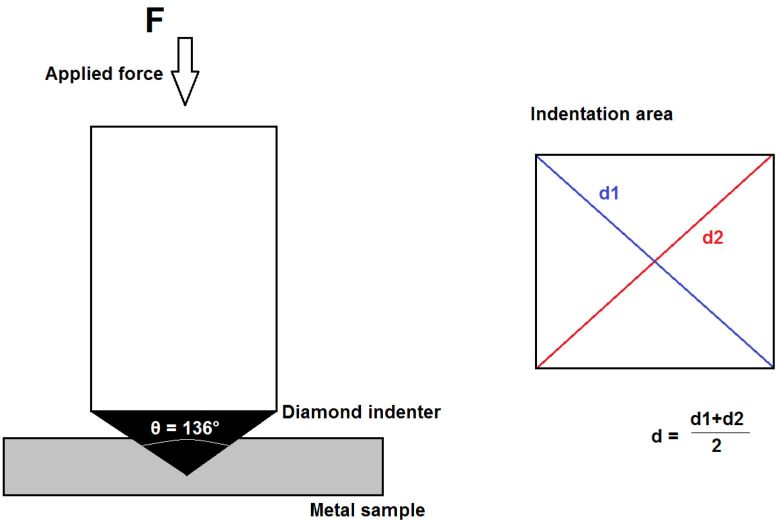

Figure 2.9: Principle of Vickers hardness testing and indentation area. The sketch is based on a figure found in [72].

From Figure 2.9 it can be seen that by measuring the diagonals of the indentation area and knowing the indenter angle, an expression for this area can be derived. This is shown in Equation (2.1) [71].

$$A = \frac{d^2}{2 \cdot sin(\frac{\theta}{2})} = \frac{d^2}{2 \cdot sin(\frac{136^\circ}{2})} = \frac{d^2}{1.854} \tag{2.1}$$

Here A is the indentation area, d is the average measured diagonal and θ is the angle between the two opposing faces of the indenter. Hardness using Vickers is given as the ratio between applied force and surface area of indentation in the material. Combining this with the result from Equation (2.1), gives the hardness expression shown in Equation(2.2) [72].

$$HV = \frac{F}{A} = \frac{1.854 \cdot F}{d^2} \tag{2.2}$$

Where F is the applied force given in kilogram force, and d is given in millimeters.

The proportionality between applied force and indentation surface, as seen in Equation (2.2), indicates that the hardness value does not depend on test force [72]. Therefore, a wide range of hardness can be determined in a continuous scale which is not the case for Rockwell tests [70]. Due to this, there are few limitations regarding sample hardness and thickness when using the Vickers test [72]. It can also be adapted to micro-hardness testing with loads below 1kgf [71]. However, a Vickers device is sensitive to vibrations for low loads which could give some uncertainty in the measurements. Also, surface preparation is often needed before testing can be performed [72].

Chapter 3

Experimental

Characterization of the interfaces in the low pressure die cast aluminum-steel and aluminum-copper castings was performed using similar sample preparation and testing methods. Experimental procedures for both bimetallic components will therefore be presented collectively in this chapter. Process parameters for each casting will be given under their respective chapters.

Low pressure die casting experiments were performed by Benteler Automotive Farsund AS (BAF). Further investigations of the aluminum-steel and aluminum-copper interfaces were therefore performed on finished castings. A 3D illustration of the compound casting component is presented in Figure 3.1. The upper yellow part in the figure contains the aluminum A356-covered pipes which were investigated.

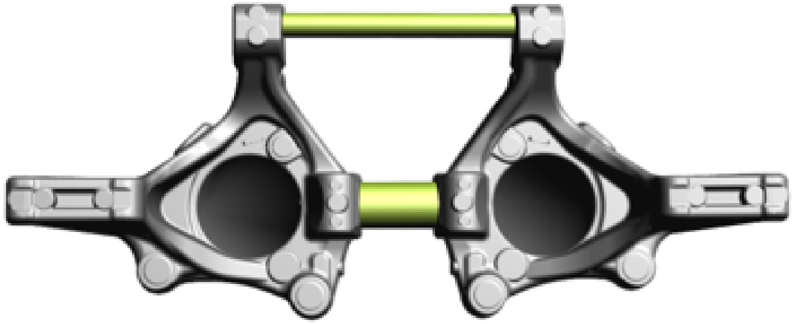

Figure 3.1: 3D illustration of the compound casting produced by Benteler Automotive Farsund AS. The upper yellow area was used for further investigation.

All steel pipes were sandblasted before additional surface treatments, copper pipes were thoroughly cleaned with ethanol. The galvanization process was performed by an external company, using a standard hot-dip process. Flux coating was painted on the steel and copper pipes. The flux used was NOCOLOK® Cs Flux, which is a mixture of $K_{1-3}AlF_{3-6}$ and $CsAlF_4$. This flux has a melting range of 558°C-566°C [73]. Heat treatment subsequent to casting was performed in Benteler Automotive Farsund AS' facilities using a T6 treatment. First castings were solution heat treated at 540°C, quenched to 70°C then artificially aged at 180°C.

3.1 Sample Preparation

All samples were prepared using the following procedure. The samples were cut from the provided castings using a Struers Labotom-15 with blade 40A35. All samples were cut from the same sides to a length of approximately 1cm as illustrated in Figure 3.2.

Figure 3.2: Cutting pattern for low pressure die casting samples.

Using a Struers LaboPol-21 the samples were ground starting from grinding paper 320 up to 4000 grits. Finally, the samples were polished using a Struers Tegramin-20. First with DiaPro Mol B 3μm diamond suspension followed by DiaPro Nap B 1μm diamond suspension until no scratches were observed on the sample surface in an optical microscope. Between polishing, the samples were cleaned with soap and water followed by 96vol% ethanol. They were then placed in a beaker filled with 96vol% ethanol and lowered into the bath of a 5510 Branson ultrasonic cleaner for approximately five minutes. This was to prevent larger diamond particles from contaminating the polishing papers.

3.2 Optical Microscope Analysis

A Leica MEF4M optical microscope was used to investigate possible reaction zones and defects in the interface. Optical micrographs were taken using magnifications from 5x to 100x.

3.3 SEM Analysis

A Zeiss Supra 55VP field emission scanning electron microscope was used to take high magnification micrographs of each sample. An acceleration voltage of 15kV was used, while the working distance was set to 10mm. Both secondary electron images and backscattered electron images were captured. The backscattered electron micrograph was in addition used to perform energy-dispersive X-ray spectroscopy (EDS) and line scans of the interfaces.

3.4 Vickers Micro-Hardness Testing

Hardness measurements were taken across the interface of each casting sample using a Leica VMHT MOT micro-hardness tester with 25g force and 10 seconds holding time. Before testing, a sample with calibrated hardness was used to ensure precise measurements.

Chapter 4

Low Pressure Die Casting of Steel Pipe in Aluminum A356

4.1 Materials and Process Parameters

The experimental procedure for sample preparation for the aluminum-steel castings were presented in Chapter 3. Two different steels were used in this low pressure die casting process. Compositions of these steels are presented in Table 4.1. Here it is assumed that ST34 is equal to the ASTM standard A283 grade A [74], while ST37 is equal to A284 grade C [75].

Table 4.1: Compositions of steels used in low pressure die casting of steel pipe in aluminum A356.

	Composition [wt%]						
	C	Mn	S	P	Si	Cu	Fe
ST34 [74]	0.14	0.9	0.05	0.04	0.04	$\geq$0.2	bal.
ST37 [75]	0.36	0.9	0.05	0.04	0.15-0.4	-	bal.

Process parameters for each of the castings investigated are presented in Table 4.2. Heat treatment was performed using the T6 process as described in Chapter 3.

Table 4.2: Process parameters for low pressure die castings of steel pipe in aluminum A356. Data was obtained from Benteler Automotive Farsund AS.

Casting	Pipe material	Pipe temperature [°C]	Galvanization	Flux coating	Metal pouring temperature [°C] (manually measured)	Heat treatment (T6)
14[a]	ST37	>100	X	X	700	-
15	ST34	>60	X[b]	X	715	X
16	ST34	>60	X[b]	X	707	-
17[a, c]	ST37	>100	-	-	700	-
28	ST37	>200	X	X	713	-
32	ST37	>200	X	-	711	X

[a] Casting produced in a separate batch
[b] No galvanization was performed, but a zinc-layer was believed to exist
[c] Casting cut from a section with thicker A356 layer

4.2 Results

Despite multiple process parameters differing for the investigated castings, results will be presented based on surface treatment. Other variations within the subsections will be specified for each casting and further considered in the following discussion. Values for hardness measurements made across the aluminum-steel interface for each casting is provided in Appendix B.

4.2.1 Effect of No Surface Treatment

Casting 17 was, as seen in Table 4.2, cut from a section with a thicker layer of cast aluminum. When cut in the longitudinal direction from the similar section as the other castings, shown in Figure 3.2, the steel pipe loosened from one of the halves cut. This implied poor bonding between the cast aluminum and steel. When cut in the similar direction in a section with a thicker layer of cast aluminum, the steel pipe remained in the casting. Further investigation of the aluminum-steel interface in Casting 17 was therefore made on the latter section. An image of this section after grinding and polishing is shown in Figure 4.1.

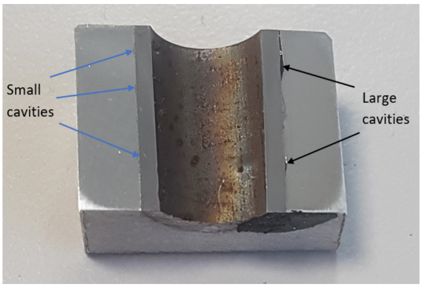

Figure 4.1: Image of Casting 17 after cutting, grinding and polishing. One side of the steel pipe has several small cavities in the interface as shown by the blue arrows. The opposite side has large interfacial cavities, noted by the black arrows.

Figure 4.1 shows that the aluminum-steel interface varies on opposite sides of the cut steel pipe. One side shows small cavities, given by blue arrows. On the other side, larger cavities can be seen by the black arrows. This difference indicates varying temperature and metal flow during mold filling, thus affecting interfacial bonding. The black area observed on the lower right end is part of a carbon conductive tab used under a previous SEM analysis.

To determine if a reaction zone had formed in the interface, optical microscopy was used. An optical micrograph of a section of the aluminum-steel interface in Casting 17 is shown in Figure 4.2.

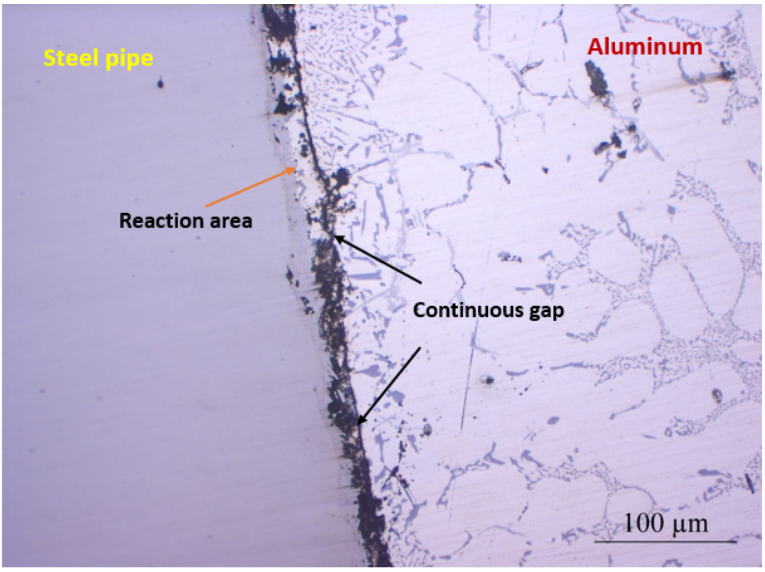

Figure 4.2: Optical micrograph of the aluminum-steel interface in Casting 17. A reaction area between the steel pipe and cast aluminum has occurred in the section, shown by an orange arrow. Despite the reaction area, a continuous gap throughout the interface can be seen by the black arrows.

Overall, the aluminum-steel interface in Figure 4.2 shows poor bonding. A continuous gap has formed between the steel pipe and cast aluminum as shown by the black arrows. However, as a reaction area between the two was detected, presented by the orange arrow, local bonding between the steel pipe and the cast aluminum has occurred. This would imply that the gap most likely became continuous upon solidification. Irregularities of the steel pipe surface in the reaction area could indicate growth of an intermetallic phase. The remaining part of the steel pipe surface also shows irregularities, which suggests that despite no reaction, the cast aluminum has influenced the surface structure.

Further investigation of a reaction zone in the aluminum-steel interface of Casting 17 was performed using EDS. A micrograph of the interface is given in Figure 4.3. Compositions of the red circled areas shown throughout the micrograph were analyzed. Results from the analysis are presented in Table 4.3.

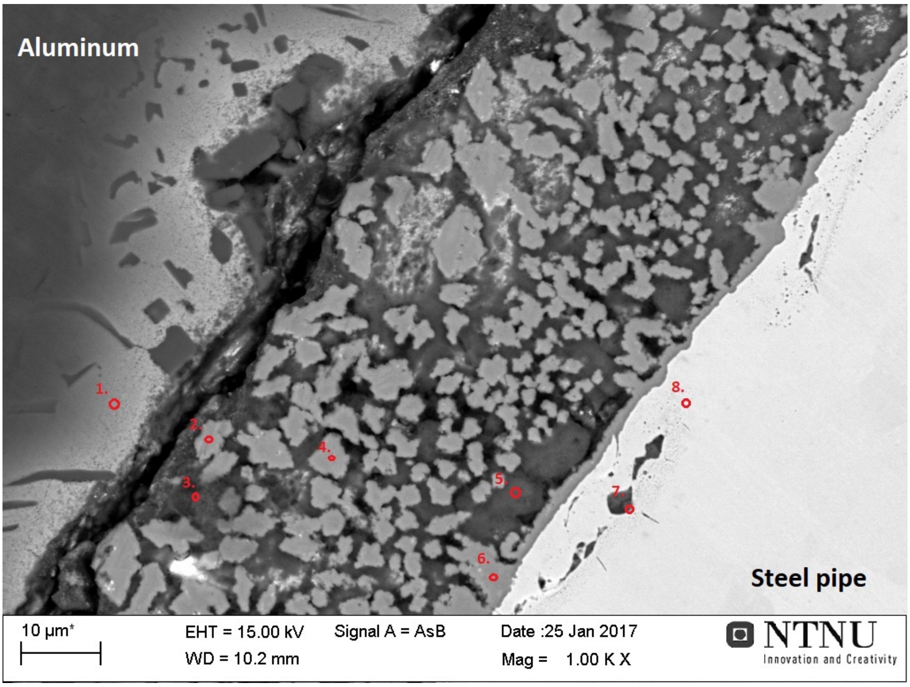

Figure 4.3: Micrograph of the aluminum-steel interface in a selected section of Casting 17. Red circles indicate areas analyzed using EDS. Results from the EDS analysis are presented in Table 4.3.

Table 4.3: Compositions and possible phases, analyzed using EDS, across the aluminum-steel interface in Casting 17 showed by red circled areas in Figure 4.3.

Area	Composition [at%]				Possible phase
	Al	Si	Fe	O	
1	100	-	-	-	(Al)
2	71.60	7.96	20.44	-	$Al_{7.4}Fe_2Si$
3	64.74	-	-	35.26	(Al) + O
4	70.65	6.81	22.54	-	$Al_{7.4}Fe_2Si$
5	70.87	-	-	29.13	(Al) + O
6	67.31	8.32	24.37	-	$Al_{7.4}Fe_2Si$
7	-	-	100	-	Fe
8	-	-	100	-	Fe

Table 4.3 shows that aluminum was detected in all areas despite those analyzed on the steel pipe surface, as seen in Figure 4.3. This indicates that there has been contact between the cast aluminum and the steel pipe. Area 2, 4 and 6 also show that formation of a ternary phase has occurred in the interface. This phase appears both as a layer on the steel pipe and as particles in the interface. Compositions found coincides with the $Al_{7.4}Fe_2Si$ phase, implying diffusion of iron atoms into the melt. However, in areas between these ternary particles, only aluminum and oxygen were detected. Although the compositions measured for these areas, as in Area 3 and 5, does not coincide with alumina, Al_2O_3, the significant oxygen concentration indicates a mixture of oxides and aluminum. This shows that despite a reaction occurring with the steel pipe, no proper metallurgical bond has formed.

The aluminum-steel interface in Casting 17 was further tested through Vickers hardness measurements. Figure 4.4 shows the tested interface, along with the measured hardness. From the optical micrograph it can be seen that the tests were performed over a reaction area.

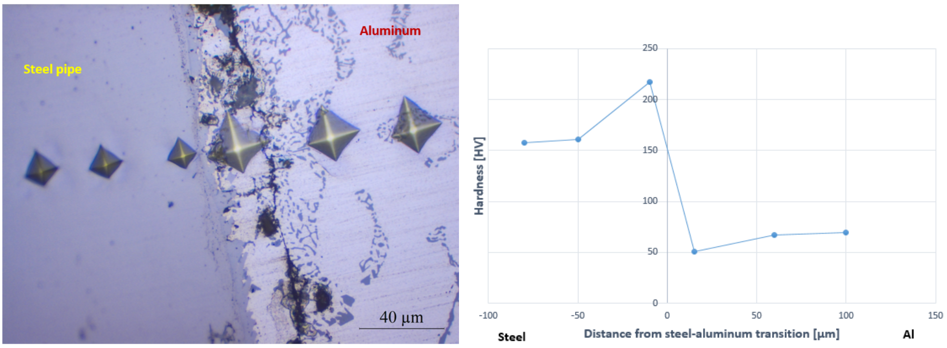

Figure 4.4: Vickers hardness measured across the aluminum-steel interface of a section in Casting 17. Steel-aluminum transition is set as transition from the steel pipe to the cast aluminum.

Figure 4.4 shows that despite a reaction area, no significant variation in hardness was observed in the interface. There is a slight increase in hardness measured in the indentation in the steel pipe adjacent to the surface. This might be due to proximity of the $Al_{7.4}Fe_2Si$-phase, as could be seen formed on the steel surface in Figure 4.3. It should also be noted that in the interface between the steel pipe and the visible crack, hardness measured is somewhat lower compared to the cast aluminum. The EDS analysis in Table 4.3, showed significant detection of oxygen in this area which might cause a porous structure displaying lower hardness than the cast aluminum.

4.2.2 Effect of Galvanization

Casting 32 used a steel pipe which was galvanized and preheated to approximately 200°C, as seen in Table 4.2. A356 melt was poured at a temperature of 711°C. The casting was subsequently heat treated using the T6 process. An image of the casting was taken after grinding and polishing. This is given in Figure 4.5. Several cavities can be observed throughout the aluminum-steel interface. Some of these are pointed out by blue arrows.

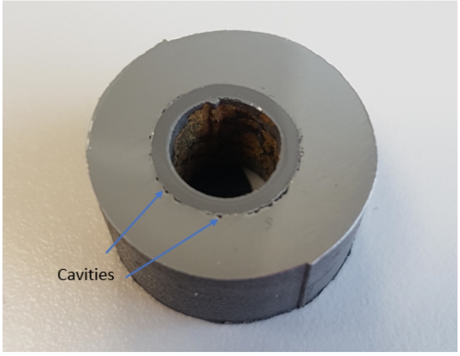

Figure 4.5: Image of Casting 32 after grinding and polishing. Several cavities are observed in the interface between aluminum and steel, as indicated by blue arrows.

Optical microscopy was used to determine if a reaction zone had formed in the interface between the steel pipe and cast aluminum, despite the observed cavities. Figure 4.6 shows an optical micrograph of an interfacial section in Casting 32. The characteristic particle structure of the galvanized layer was not detected in the casting.

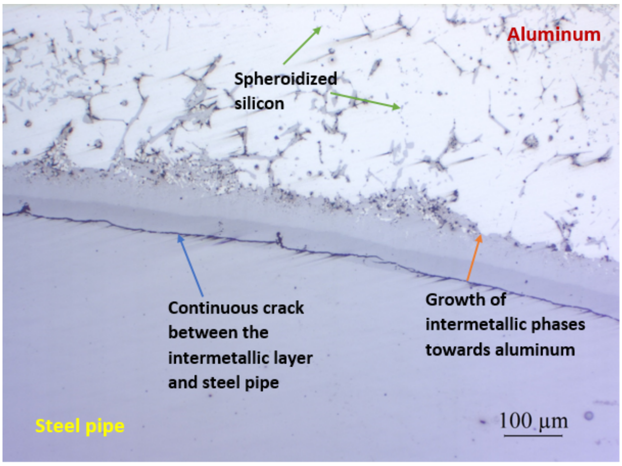

Figure 4.6: Optical micrograph of the aluminum-steel interface in Casting 32. An orange arrow shows growth of intermetallic phases towards the cast aluminum. A crack is observed between this layer and the steel pipe, as noted by the blue arrow. Green arrows show spheroidized silicon due to heat treatment.

From Figure 4.6 growth of a reaction zone from the steel surface towards the cast aluminum is observed. This is indicated by an orange arrow. Based on color in the optical micrograph, it appears as if two separate intermetallic layers have formed in the reaction zone. Between the steel pipe and the adjacent layer, a continuous crack can be observed, as noted by a blue arrow. The interface between the cast aluminum and the intermetallic layer shows no apparent defects, indicating continuous bonding. This intermetallic layer shows an irregular structure where some particles appears to have separated from the layer and entered the cast aluminum. Thickness of the reaction zone remained somewhat uniform throughout this section of the casting, despite the mentioned irregularities. It should also be noted that eutectic silicon particles in the bulk of the aluminum casting have spheroidized as a result of the heat treatment, as noted by the green arrows in Figure 4.6. To determine if two intermetallic layers had formed, a line scan was performed over the same section. This line scan is provided in Figure 4.7.

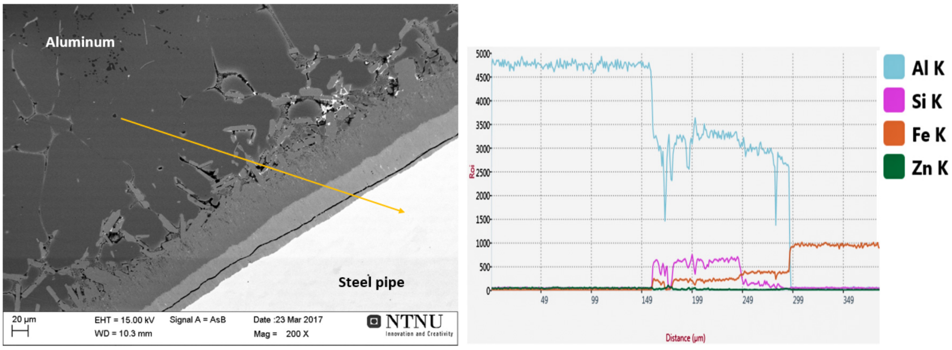

Figure 4.7: EDS line scan across the aluminum-steel interface in Casting 32. The scan follows the yellow line in the micrograph. X-axis gives distance from starting point, whereas y-axis shows intensity of element detected. Elements found are designated with different colors given in the graph.

As shown by the line scan in Figure 4.7, the iron content showed by an orange line increases with decreasing distance to the steel pipe surface. It then remains constant until it reaches the brighter layer where it increases further. Aluminum, given by a light-blue line, shows an opposite trend. The pink line representing silicon is barely detected until the first intermetallic layer is reached, where it increases to approximately twice that of iron. When reaching the bright grey layer at the steel pipe surface, the silicon content drops significantly. This confirms that at least two different intermetallic layers indeed have formed. An average thickness of the reaction zone was measured to 127μm. The section in which the line scan passes, shows sign of porosities between the cast aluminum and intermetallic layer. This indicates presence of oxygen which would imply that bonding is not ideal.

Compositions of the interfacial phases in Casting 32 were investigated using EDS. A section is shown in the micrograph in Figure 4.8. Between the cast aluminum and the adjacent intermetallic layer, a large cavity is observed. On each side of the cavity a smaller gap separating the reaction layer and the cast aluminum can be seen. The numbered red circles in the micrograph indicate areas analyzed by EDS. Results from the analysis are presented in Table 4.4.

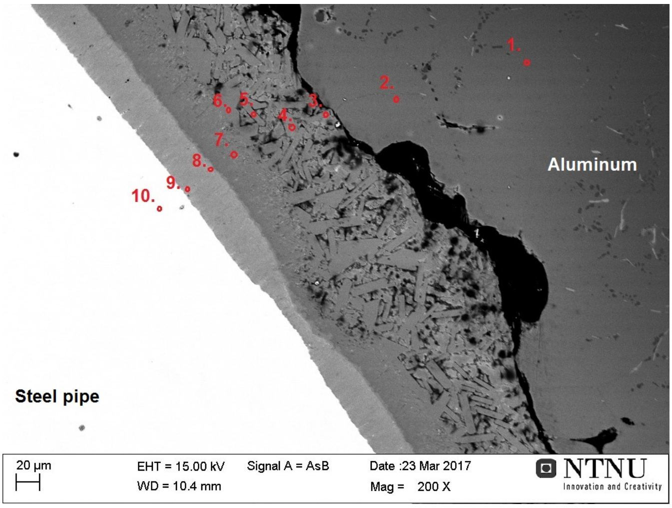

Figure 4.8: Micrograph of the aluminum-steel interface in Casting 32. Red circled areas were analyzed using EDS. Results from the analysis are presented in Table 4.4.

Table 4.4: Compositions and possible phases, analyzed using EDS, across the aluminum-steel interface in Casting 32 showed by red circled areas in Figure 4.8.

Area	Composition [at%]					Possible phase
	Al	Fe	Si	Zn	O	
1	96.54	-	-	3.46	-	(Al) + Zn
2	93.05	-	1.31	5.64	-	(Al) + Zn
3	64.27	10.59	20.03	2.01	3.10	Al_3FeSi_2
4	68.43	12.64	18.93	-	-	Al_3FeSi_2
5	77.57	6.32	10.95	5.17	-	-
6	68.31	12.69	19.00	-	-	Al_3FeSi_2
7	68.10	10.96	18.77	2.16	-	Al_3FeSi_2
8	70.51	18.20	9.98	1.32	-	$Al_{7.4}Fe_2Si$
9	70.70	21.09	2.91	1.29	4.00	Al_3Fe
10	-	100	-	-	-	Fe

Low concentrations of zinc are detected in Area 1 and 2 as seen in Table 4.4. Figure 4.27 shows that these areas are on the cast aluminum side of the gap. This indicates that some zinc from the galvanized layer has diffused into the cast aluminum. In the reaction zone the detected compositions confirmed formation of multiple intermetallic layers, and thus that the galvanized layer has melted. Area 3, 4, 6 and 7 have relatively similar compositions and are therefore believed to be the same phase. High concentrations of both iron and silicon implies formation of a ternary phase, most likely Al_3FeSi_2. In Area 5, the iron content is significantly lower in comparison to the surrounding areas. The composition in this area does not coincide with any known ternary Al-Fe-Si phase. Area 8 and 9 found in the intermetallic layer adjacent to the steel surface, have similar aluminum and iron contents, while the silicon content varies. The composition in Area 8, which has a higher amount of silicon, coincides with the ternary $Al_{7.4}Fe_2Si$ phase. Area 9 is most likely the binary Al_3Fe-phase, implying that despite the similar brightness in the two areas, two separate phases have formed. This might be a result of the heat treatment.

Hardness was also measured across the aluminum-steel interface in Casting 32. The results are presented in Figure 4.9, where the optical micrograph shows the interfacial section in which the measurements were performed.

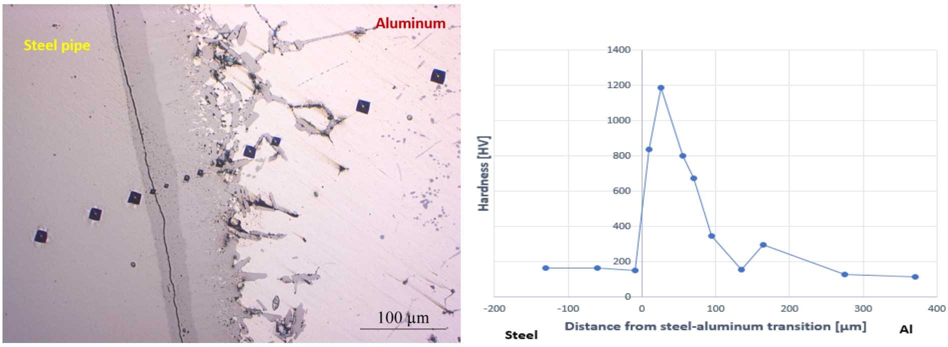

Figure 4.9: Vickers hardness measured across the aluminum-steel interface of a section in Casting 32. Steel-aluminum transition is set as transition from the steel pipe to the adjacent intermetallic phase.

The hardness measurements in Figure 4.9 show that hardness is between four and six times higher in the intermetallic layers compared to both the steel pipe and cast aluminum. Hardness varies for the intermetallic phases, with the highest measurement most likely made for the Al_3Fe layer based on the EDS analysis in Table 4.4. Within the intermetallic layer adjacent to the cast aluminum, determined to be Al_3FeSi_2, hardness decreases towards the cast aluminum. This could be due to the particle structure observed in Figure 4.9 where cast aluminum, with lower hardness, is present between particles. Hardness of the cast aluminum itself, has approximately the same value as the steel pipe. As aluminum is softer than steel, this implies a strength increase as a result of the heat treatment.

4.2.3 Effect of Zinc and Flux Coating Combined

For Casting 15 and 16, the steel pipe was preheated to 60°C and flux coated prior to casting. No galvanization was performed on the steel pipes. However, a zinc-layer was believed to be present on the surface based on observations prior to casting. To determine if a zinc-layer was present, a micrograph was taken of the outer surface of the steel pipe in Casting 16 without A356 cast around. This is shown in Figure 4.10, where the red circled areas were analyzed using EDS. Results from the analysis are provided in Table 4.5.

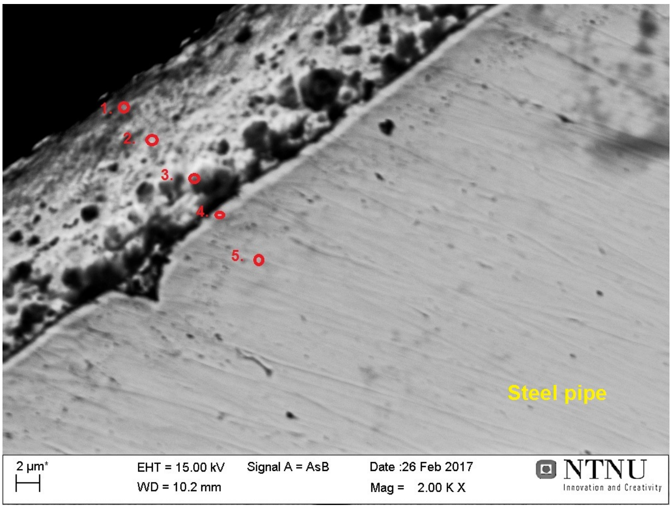

Figure 4.10: Micrograph of the steel pipe used in Casting 16. Red circles indicate areas analyzed using EDS. Results from the EDS analysis are presented in Table 4.5.

Table 4.5: Compositions and possible phases, analyzed using EDS, across the steel pipe used in Casting 16 showed by red circled areas in Figure 4.10.

Area	Composition [at%]			Possible phase
	Zn	O	Fe	
1	100	-	-	Zn
2	86.88	13.12	-	Zn with O impurity
3	83.03	16.97	-	Zn with O impurity
4	51.34	48.66	-	ZnO
5	6.15	-	93.85	Fe

Table 4.5 shows that zinc exists in all areas investigated, confirming a zinc-layer on the steel pipe. The layer has a thickness of approximately 12μm. However, the high concentration of oxygen detected gives a rather porous layer, which is also seen in Figure 4.10 where several

dark areas are present. In addition, ZnO appears to have formed between the zinc-layer and the steel surface, as seen in Area 4. This could explain the poor bonding between the two. Iron was not detected in the zinc-layer and thus no binary Fe-Zn phases formed. Area 5 shows detection of both iron and zinc, but as the iron content is too high to coincide with any binary phase, this is most likely due to diffusion of zinc into the steel surface.

Characterization of the aluminum-steel interface in Casting 15 and 16 was performed after determining the zinc coated layer. Results from the characterization will be presented separately, while hardness measurements of the two will be compared at the end of this subsection.

Casting 15 had a liquid aluminum pouring temperature of 715°C, as shown in Table 4.2. In addition, heat treatment using the T6 process was performed subsequent to casting. After grinding and polishing an image was taken of Casting 15. This is shown in Figure 4.11.

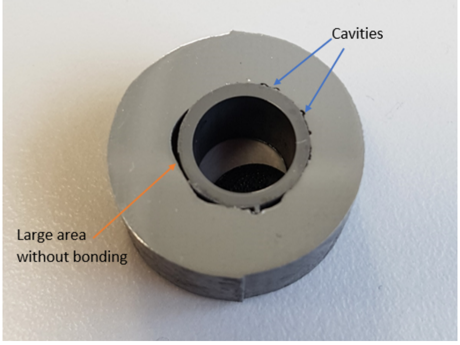

Figure 4.11: Image of Casting 15 after grinding and polishing. A large non-bonding area is shown by the orange arrow. Several cavities observed in the interface between steel and aluminum are noted by blue arrows.

Figure 4.11 shows that there is poor bonding between the cast aluminum and the steel pipe almost throughout the casting. A large area, making up approximately half the interface, shows no bonding and presumably poor wettability, as shown by the orange arrow. This area has a substantial continuous cavity. The remaining part of the casting shows multiple relatively large cavities, some which are noted by the blue arrows. Formation of a potential reaction layer in this area was further examined using an optical microscope. Figure 4.12 shows an optical micrograph of the interface in Casting 15.

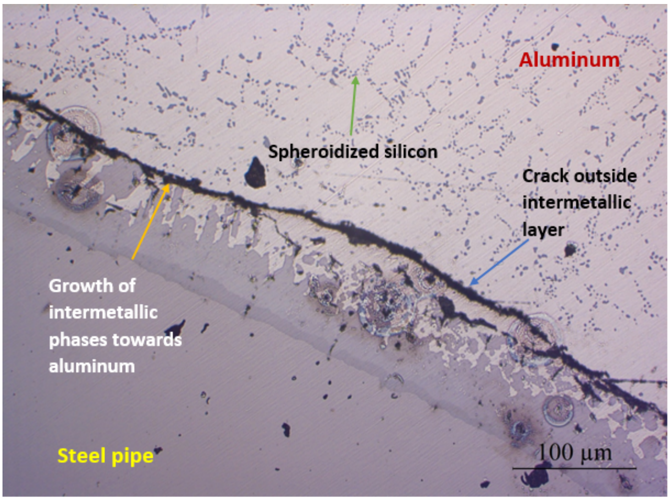

Figure 4.12: Optical micrograph of the aluminum-steel interface in Casting 15. A yellow arrow indicates growth of multiple intermetallic phases towards the cast aluminum, while a blue arrow shows a crack outside these phases. Spheroidized silicon is noted by a green arrow.

On the steel pipe surface, growth of intermetallic phases towards the cast aluminum was observed. This is indicated by the yellow arrow in Figure 4.12. Based on colors in the optical micrograph, there appears to be two different intermetallic phases formed. A crack has occurred in the cast aluminum outside the intermetallic layer, shown by a blue arrow. In addition, the eutectic silicon has spheroidized as a result of the heat treatment. This is noted by a green arrow. An EDS line scan using SEM was performed on the same section in the casting. This is shown in Figure 4.13.

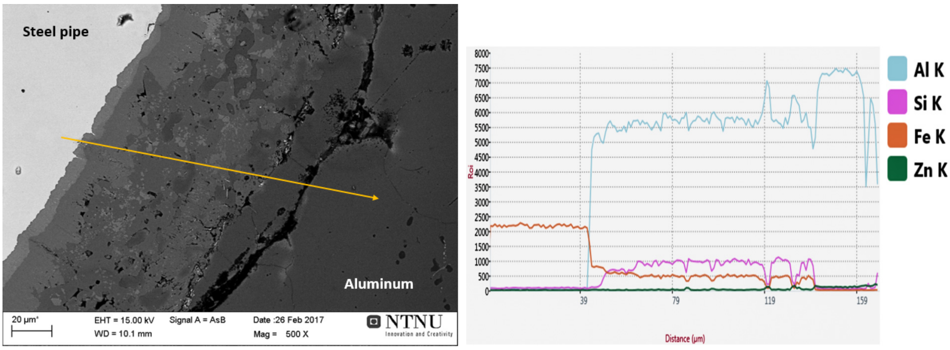

Figure 4.13: EDS line scan across the aluminum-steel interface in Casting 15. The scan follows the yellow line in the micrograph. X-axis gives distance from starting point, whereas y-axis shows intensity of element detected. Elements found are designated with different colors given in the graph.

The orange line representing iron in Figure 4.13, decreases towards the cast aluminum. Adjacent to the steel surface almost no aluminum or silicon, represented by light-blue and pink lines respectively, are detected. The aluminum content increases significantly and remains somewhat constant as the scan continues over the reaction layer. Silicon shows a similar trend, except with a lower concentration detected. Zinc however, represented by the dark-green line, is barely present in the reaction layer which implies that the zinc-layer has melted. A somewhat higher zinc content is detected at the end of the line scan which could indicate some diffusion into the cast aluminum. If the reaction layer spans from the steel surface until no iron is detected, the thickness of the reaction layer is measured to be approximately 145μm. It should also be noted that the section in which the micrograph was taken, shows irregularities in the contrast observed in the interface. This could imply that multiple intermetallic phases formed, but that their compositions were too similar to be distinguished by the line scan.

Figure 4.14 shows a section of Casting 15 with a different structure than observed in Figure 4.13. EDS was used to analyze compositions of intermetallic phases formed in this section. Red circles in Figure 4.14 indicate areas that were analyzed. Results from the analysis are provided in Table 4.6.

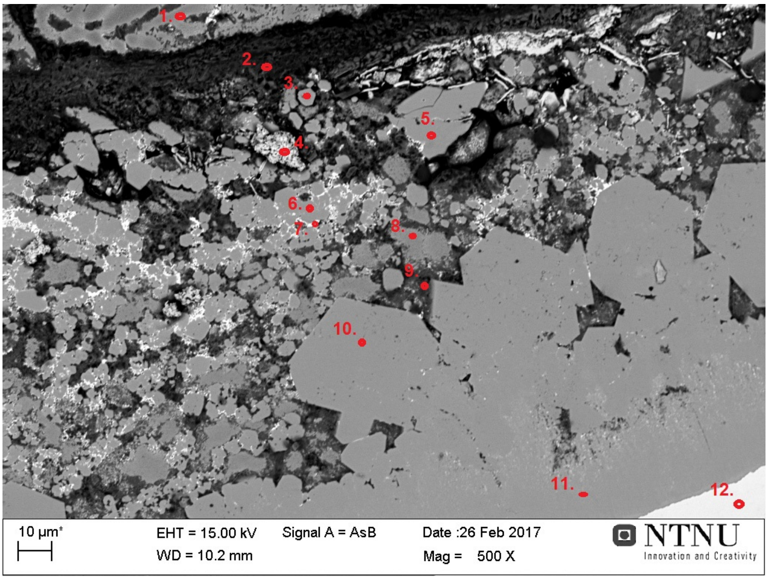

Figure 4.14: Micrograph of the aluminum-steel interface in Casting 15. Red circled areas were analyzed using EDS. Results of the analysis are presented in Table 4.6.

Table 4.6: Chemical compositions and possible phases, analyzed using EDS, across the aluminum-steel interface in Casting 15 showed by red circled areas in Figure 4.14.

Area	Composition [at%]								Possible phase
	Al	Fe	Zn	Si	Mg	K	F	O	
1	84.77	-	15.23	-	-	-	-	-	(Al) + Zn
2	17.93	-	4.59	-	12.38	8.85	28.26	27.99	Flux residue
3	71.85	17.01	4.78	6.36	-	-	-	-	$Al_{7.4}Fe_2Si$
4	-	0.89	53.35	-	-	-	-	45.77	ZnO
5	71.06	16.79	5.11	7.03	-	-	-	-	$Al_{7.4}Fe_2Si$
6	71.85	19.96	3.45	4.74	-	-	-	-	$Al_{7.4}Fe_2Si$
7	38.73	-	61.27	-	-	-	-	-	(Al) + Zn
8	84.17	-	15.83	-	-	-	-	-	(Al) + Zn
9	55.80	-	13.00	-	-	-	-	31.20	(Al) + Zn
10	71.86	17.17	4.65	6.32	-	-	-	-	$Al_{7.4}Fe_2Si$
11	74.47	23.66	-	1.87	-	-	-	-	Al_3Fe
12	-	100	-	-	-	-	-	-	Fe

Presence of zinc throughout the interface, as seen in Table 4.6 indicates that the detected zinc-layer has not diffused into the cast aluminum and instead remained in the interface. A dark porous layer can be seen in Figure 4.14 between the cast aluminum found in Area 1 and the reaction layer identified in the remaining areas. Detection of magnesium, potassium fluoride and oxygen in this layer, as given by Area 2, implies that the dark layer consists of flux residue. Relatively high concentrations of oxygen were also detected in Area 4 and 9, especially in Area 4. The composition here coincides with formation of ZnO. This shows that oxide removal has been incomplete and therefore no proper bonding was achieved.

Compositions in Area 3, 5, 6 and 10 are fairly similar. Therefore, they are assumed to be the same ternary Al-Fe-Si phase, most likely $Al_{7.4}Fe_2Si$. In Area 11 the iron content is higher and silicon lower compared to the abovementioned areas. A contrast difference can also be observed between Area 10 and 11 in Figure 4.14, which would imply different phases. With an aluminum-iron ratio of 3.15, it is believed that in Area 11 at the steel pipe surface the binary Al_3Fe phase has formed.

Casting 16 had similar process parameters as Casting 15, except the metal pouring temperature being 707°C and no subsequent heat treatment was performed. A macroscopic investigation was made on the casting after grinding and polishing. This can be seen in Figure 4.15. The blue arrow shows a relatively large cavity detected in the aluminum-steel interface. However, compared to the image of Casting 15 in Figure 4.11, the interface shows significantly less defects. This would imply that the heat treatment is not beneficial for interfacial bonding.

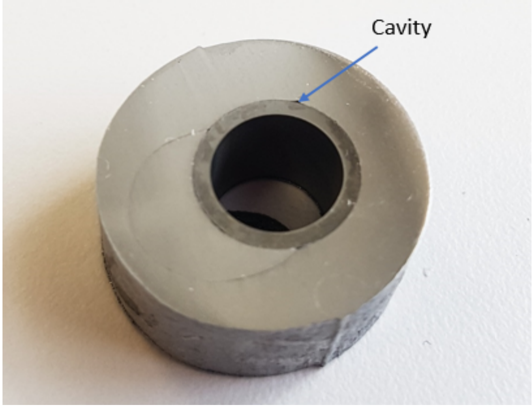

Figure 4.15: Image of Casting 16 after grinding and polishing. The blue arrow indicates a relatively large cavity.

As seen in Figure 4.15, only a few defects were observed in the aluminum-steel interface in Casting 16. To determine if a reaction zone had formed between the steel pipe and the cast aluminum, optical microscopy was used. An optical micrograph is given in Figure 4.16.

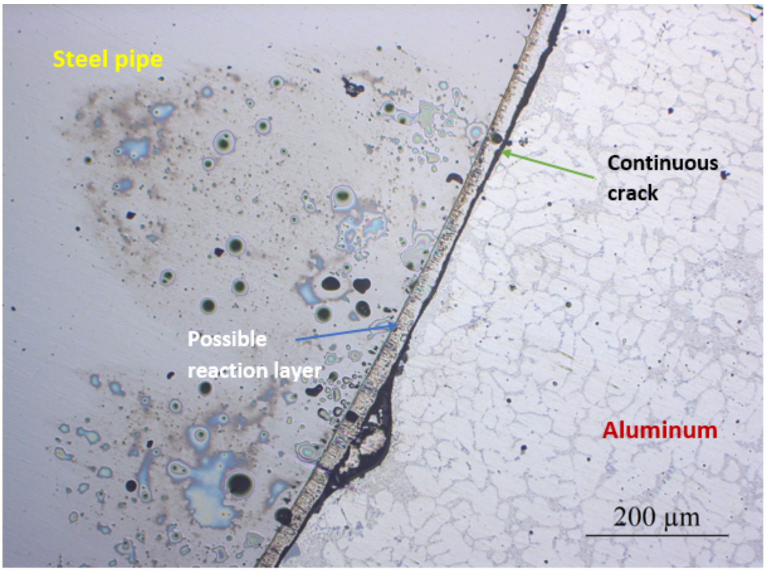

Figure 4.16: Optical micrograph of the aluminum-steel interface in Casting 16. The blue arrow shows a potential intermetallic layer, while a continuous crack in the aluminum-steel interface is noted by a green arrow.

A possible reaction layer formed on the steel pipe surface, as indicated by the blue arrow in Figure 4.16. This layer appears to be somewhat uniform and shows growth towards the cast aluminum. However, a continuous crack is observed between the potential reaction layer and the cast aluminum, shown by the green arrow. Based on color in the optical micrograph, the crack appears to vary between being in the reaction layer-cast aluminum interface and go through the cast aluminum. To determine composition of the potential reaction layer, a line scan was performed across the same section in Casting 16. This is shown in Figure 4.17.

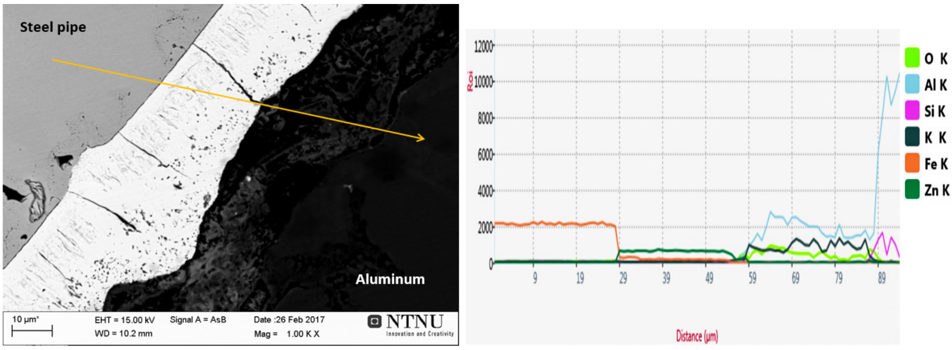

Figure 4.17: EDS line scan across the aluminum-steel interface in Casting 16. The scan follows the yellow line shown in the micrograph. X-axis gives distance from starting point, whereas y-axis shows intensity of element detected. Elements found are designated with different colors given in the graph.

From the line scan in Figure 4.17, it can be seen that an intermetallic layer has formed on the steel surface. The dark-green and orange lines, representing zinc and iron respectively, are detected in this layer which implies formation of a binary Fe-Zn phase. The zinc-layer detected on the steel pipe showed no Fe-Zn phases, which would indicate formation upon casting due to the elevating temperature causing diffusion of iron. Outside the layer, the light-blue line representing aluminum starts to increase. This suggests contact between the cast aluminum and the reaction layer. However, as shown by the light-green and green-blue lines, representing oxygen and potassium respectively, the bonding is not optimal. The detection of potassium is most likely due to flux residue. Since oxygen also is detected, this implies that the flux has not been able to remove all oxides from the aluminum melt.

A section with structure differing from that observed in Figure 4.17 was also detected in Casting 16. This section showed growth of intermetallic phases at the steel pipe. It was further investigated using SEM and EDS, as shown by red circled areas in Figure 4.18. Compositions determined through the EDS analysis are presented in Table 4.7.

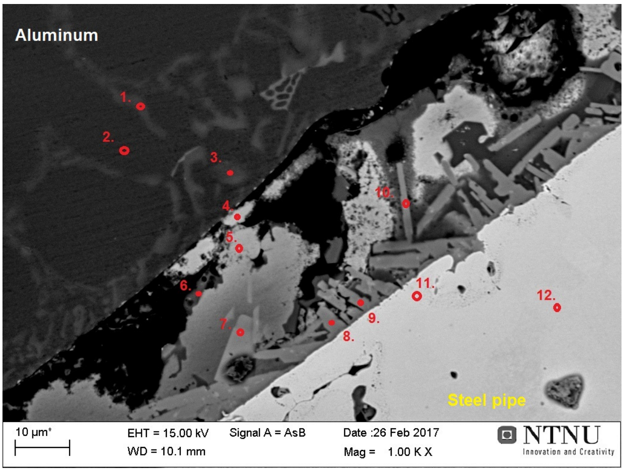

Figure 4.18: Micrograph of the aluminum-steel interface in Casting 16. Red circles indicate areas analyzed using EDS. Results from the EDS analysis are presented in Table 4.7.

Table 4.7: Compositions and possible phases, analyzed using EDS, across the aluminum-steel interface in Casting 16 showed by red circled areas in Figure 4.18.

Area	Composition [at%]					Possible phase
	Al	Fe	Si	Zn	O	
1	71.41	-	28.59	-	-	Eutectic Al-Si
2	98.90	-	1.10	-	-	(Al)
3	39.17	-	60.83	-	-	Eutectic Al-Si
4	77.22	-	22.78	-	-	Eutectic Al-Si
5	75.21	-	-	24.79	-	(Al) + Zn
6	13.24	1.06	23.97	36.76	24.97	(Al) + (Si) + Zn
7	78.35	7.67	9.91	4.07	-	$Al_{4.5}FeSi$
8	68.07	14.45	15.75	1.73	-	$Al_{4.5}FeSi$
9	66.39	5.65	5.63	7.27	15.06	$Al_{4.5}FeSi$
10	67.65	6.52	7.79	7.94	10.11	$Al_{4.5}FeSi$
11	54.90	33.96	9.27	1.87	-	Al_2Fe
12	-	100	-	-	-	Fe

As shown in Table 4.7 aluminum was detected until the steel surface, suggesting that the zinc-layer melted in this section. Figure 4.18 shows growth of a phase on the steel surface. The atomic ratio provided from the composition in Area 8 indicate that this phase is the ternary eutectic $Al_{4.5}FeSi$ phase. Particles of this phase have lengths varying from $4\mu m$ to $27\mu m$, approximately. Areas 9 and 10 however, show compositions differing from Area 8, with a high concentration of zinc. Still, due to similar iron and silicon content in these sections, formation of $Al_{4.5}FeSi$ is suggested. In Area 9 and 10 a relatively high concentration of oxygen is also detected, indicating that oxides have not been properly removed. This can also be seen in Area 6. Figure 4.18 shows that despite formation of intermetallic phases, there are large black areas which could be cavities or flux residue. Thus, no good bonding was observed in this section.

Hardness measurements made across the aluminum-steel interface in both Casting 15 and 16 are provided in Figure 4.19

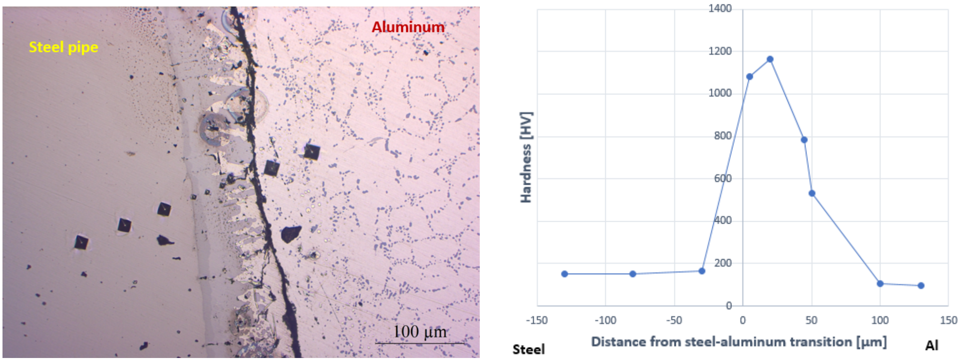

(a) Vickers hardness measured across the interface in Casting 15. Steel-aluminum transition is set as transition from steel to intermetallic layer.

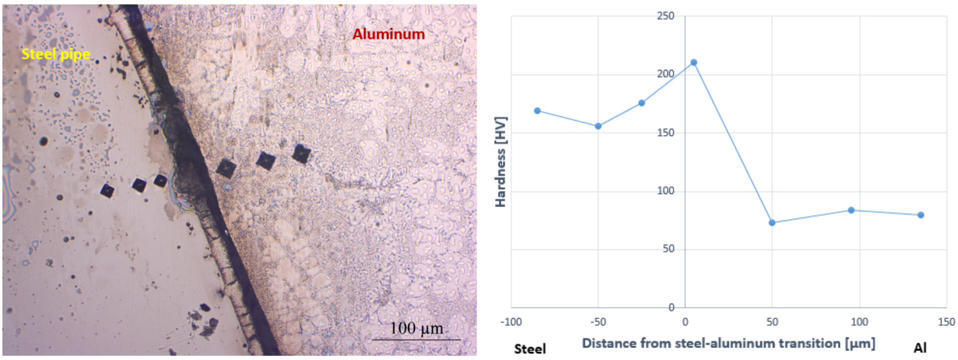

(b) Vickers hardness measured across the interface in Casting 16. Steel-aluminum transition is set as transition from steel to intermetallic layer.

Figure 4.19: Vickers hardness measured across the aluminum-steel interface in Casting 15 and 16.

Figure 4.19 shows variation in the interfaces observed for Casting 15 and 16. In Casting 15, hardness of the intermetallic layers are almost six times higher than that measured for both the cast aluminum and the steel pipe. Hardness in the two layers observable by color only vary slightly. A larger difference can be seen within the intermetallic layer adjacent to the cast aluminum, as the hardness decreases in the growth direction. This is believed to be due to the non-uniformity of the layer causing adjacent aluminum to be included in a larger scale as the measurements approach the cast aluminum. It should also be noted that by comparing Casting 15 and 16, the measured hardness of the cast aluminum has increased from 80HV to 100HV in Casting 15. This would imply that hardness has increased in the cast aluminum as a result of heat treatment. In Casting 16, only a slight increase in hardness could be observed in the interface compared to the steel pipe. Although the indentation is not very visible in the optical micrograph in Figure 4.19b, this measurement was performed on the layer determined to be binary Fe-Zn in Figure 4.17. Comparing the two optical micrographs also shows that a thicker reaction layer has formed in Casting 15, most likely due to the heat treatment.

4.2.4 Effect of Galvanization Combined With Flux Coating

Casting 14 and 28 had a galvanized layer with flux coating. Characterization of the interfaces will be presented separately, while hardness tests will be compared at the end of this subsection. The galvanization of Casting 14 and 28 was performed by the same company and was believed to have similar structure despite being produced in two separate batches. Structure of the galvanized layer was determined by performing a line scan across various sections of the steel pipe used in Casting 28. Two of these are shown in Figure 4.20.

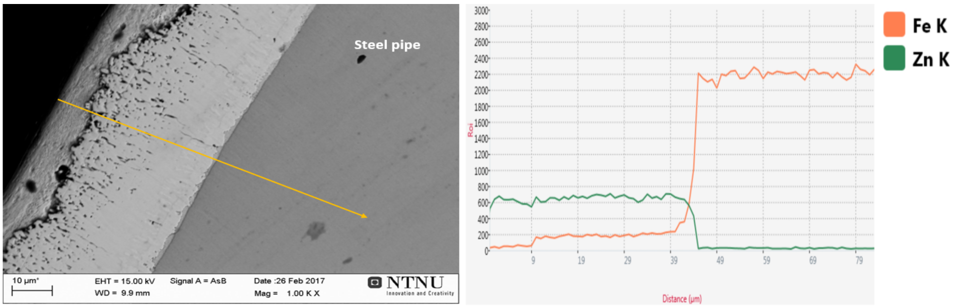

(a) Line scan of one section of the steel pipe used in Casting 28.

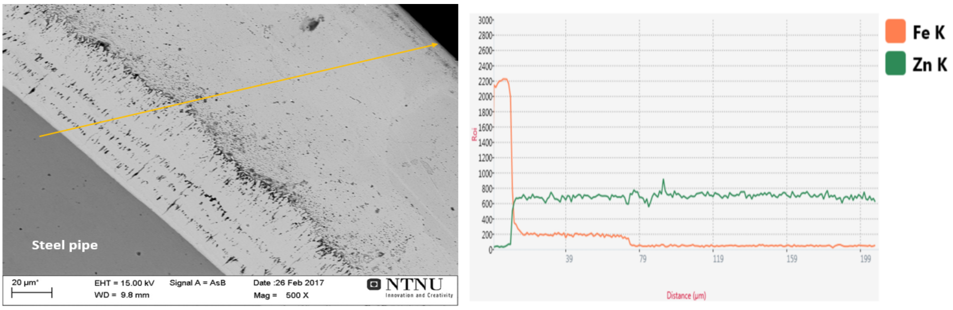

(b) Line scan of one section of the steel pipe used in Casting 28.

Figure 4.20: EDS line scan across two sections of the steel pipe in Casting 28. The scan follows the yellow line. X-axis gives distance from the starting point, y-axis shows intensity of element detected. Elements are designated by different colors given in the graph.

Both line scans in Figure 4.20 show that iron, given by the orange line, is detected throughout the galvanized layer. This implies formation of binary Fe-Zn. As the iron content decreases outwards in the layer for both sections, it indicates that multiple binary compounds have formed. In addition, the binary layer adjacent to the steel pipe shows variations in the structure, whereas the outer layer is more uniform. By comparing the sections in Figure 4.20a and 4.20b, it is evident that there is a large variation in the galvanized layer thickness. In Figure 4.20a the layer thickness is measured to approximately 40μm, while in Figure 4.20b it is approximately 165μm, over four times as thick. This shows that the galvanized layer is non-uniform.

Casting 14 was produced in a previous batch, and was therefore cut along the longitudinal section for further inspection. Process parameters provided in Table 4.2 show that the casting had a metal pouring temperature of 700°C while the steel pipe was preheated to approximately 100°C. A macroscopic photograph of one of the halves cut from Casting 14 is shown in Figure 4.21 after grinding and polishing.

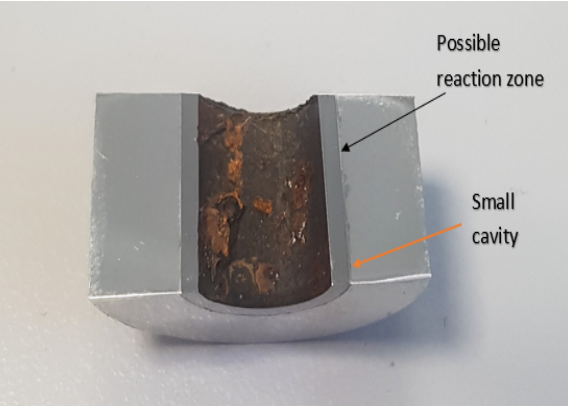

Figure 4.21: Image of Casting 14 after cutting, grinding and polishing. The black arrow indicates a possible reaction zone, whereas the orange shows a small interfacial cavity.

Figure 4.21 shows that the interface varies on opposite sides of the cut casting. On the left side, no apparent defects can be observed in the aluminum-steel interface. The right side shows a macroscopically visible cavity in the aluminum-steel interface, as indicated by the orange arrow. In addition, a possible reaction zone might have formed based on color difference in the interface as seen by the black arrow. The differences in the interface on opposite sides of the cut casting, suggest local variations in temperature upon casting. Optical microscopy was used to examine if any difference could exist in the interfacial structure along the cut sides of Casting 14. Figure 4.22 and 4.23 show two structures found in different sections of the casting.

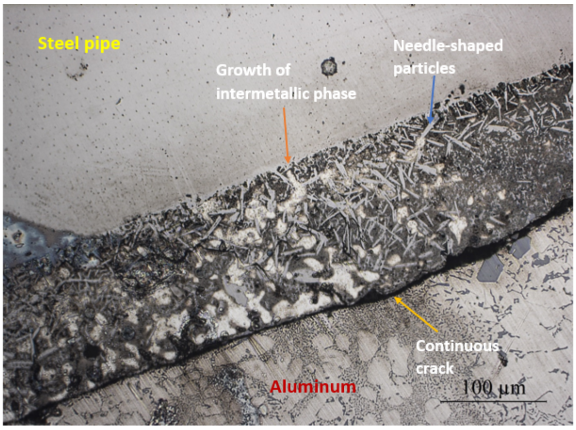

Figure 4.22: Optical micrograph of a section of the aluminum-steel interface in Casting 14 where the galvanized layer melted. Growth of an intermetallic phase from the steel pipe is noted by the orange arrow, whereas the blue arrow indicates needle-shaped particles in the interface. The yellow arrow shows a continuous crack between the reaction zone and the cast aluminum.

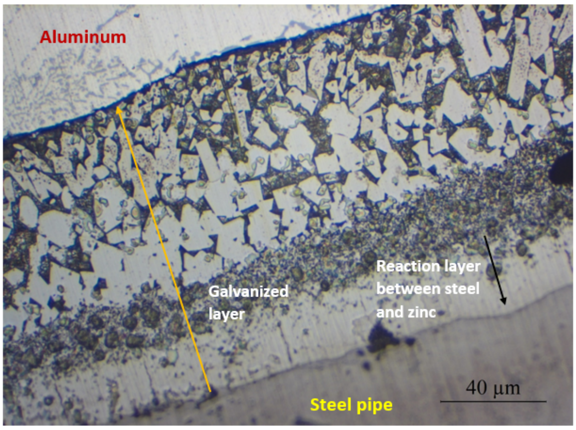

Figure 4.23: Optical micrograph of a section of the aluminum-steel interface in Casting 14 where the galvanized layer remained intact. The yellow arrow shows a structure recognized as a galvanization layer. A black arrow indicates that a reaction zone has occurred between steel and zinc in the galvanized layer.

From the two optical micrographs in Figure 4.22 and 4.23, two different structures are found in the interface in Casting 14. Figure 4.22 shows a section with growth of an intermetallic phase on the steel surface, as indicated by the orange arrow. In the interface, needle-shaped particles were observed, designated by the blue arrow. These coincide with the shape observed for the intermetallic phase formed on the steel surface. The yellow arrow shows that there is a continuous crack between the reaction layer and the cast aluminum, indicating poor bonding. In Figure 4.23, the large particles in the interface are recognized as those originally formed in the galvanized layer, implying that it did not melt upon casting. Thickness of the galvanized layer is indicated by the yellow arrow, which is measured to approximately 123μm. A reaction zone formed between zinc in the galvanized layer and steel, as shown by the black arrow. However, no such reaction zone is observed between the cast aluminum and galvanized layer, indicating that the outer part of the galvanized layer has not melted in this section. Still, no obvious crack is observed and thus the bonding is believed to be sufficient.

Further investigations using EDS were performed on the section in Figure 4.22. Chemical compositions measured are provided in the micrograph in Figure 4.24 and Table 4.8.

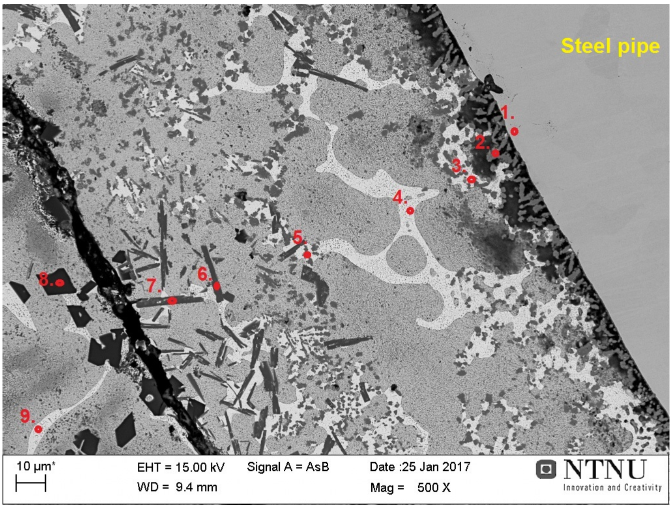

Figure 4.24: Micrograph of the aluminum-steel interface in a selected section of Casting 14. Red circles indicate areas analyzed using EDS. Results from the EDS analysis are presented in Table 4.8.

Table 4.8: Compositions and possible phases, analyzed using EDS, across the aluminum-steel interface in Casting 14 showed by red circled areas in Figure 4.24.

Area	Composition [at%]				Possible phase
	Al	Fe	Si	Zn	
1	-	98.11	-	1.89	Fe
2	65.93	17.52	8.09	8.47	$Al_{7.4}Fe_2Si$
3	10.67	1.43	-	87.90	Zn + (Al)
4	-	-	-	100	Zn
5	63.92	19.37	9.54	7.17	$Al_{7.4}Fe_2Si$
6	53.83	16.10	27.78	2.28	Al_3FeSi_2
7	63.90	14.77	17.92	3.41	$Al_{4.5}FeSi$
8	-	-	98.95	1.05	Si
9	4.52	-	-	95.48	Zn

From Table 4.8 it can be seen that aluminum is detected throughout the section investigated, indicating that the galvanized layer has remelted and mixed with aluminum. However, it is worth noting that relatively high concentrations of zinc were also detected throughout the interface. Especially in Areas 3, 4 and 9, implying that zinc-rich intermetallic particles might have precipitated in the aluminum melt. The phase growing adjacent to the steel surface, shown in Area 2 in Figure 4.24, is believed to be ternary $Al_{7.4}Fe_2Si$ based on the atomic ratios found in Table 4.8. Areas 5, 6 and 7 are all needle-shaped particles found in the interface. These appear to be ternary Al-Fe-Si phases with various composition, as given in Table 4.8. Length of the particles varies from approximately 5μm to 30μm. A plate-shaped particle observed in Area 8 has 98.95 at% silicon, implying formation of a primary silicon particle. It can be seen in Figure 4.24 that several particles with similar contrast and shape have formed in the same area, indicating formation of a large number of silicon particles. A crack can also be seen propagating through the area where the particles formed.

Casting 28 had similar process parameters as Casting 14, except that the steel pipe was preheated to 200°C and the metal pouring temperature was 713°C. An image of the casting after grinding and polishing is shown in Figure 4.25.

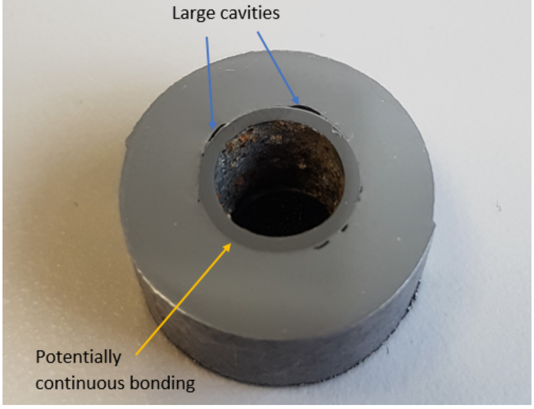

Figure 4.25: Image of Casting 28 after grinding and polishing. The blue arrows indicate large cavities between the cast aluminum and steel pipe. An area with potentially continuous bonding is noted by the yellow arrow.

Overall, several large cavities can be seen in the aluminum-steel interface in Figure 4.25. Some of these are indicated by blue arrows. An area of the interface showed potentially continuous bonding, noted by a yellow arrow. Further investigation of the interfacial area was done using an optical microscope. An optical micrograph from the aluminum-steel interface is shown in Figure 4.26.

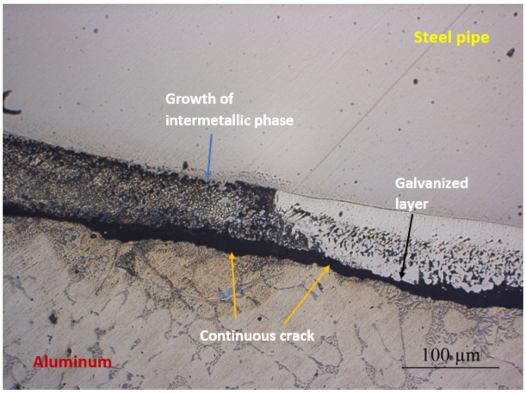

Figure 4.26: Optical micrograph of the aluminum-steel interface in Casting 28. Growth of an intermetallic phase from the steel pipe is shown by a blue arrow. The layer indicated by the black arrow is recognized as the galvanized layer. A continuous crack between the interfacial layer and cast aluminum is noted by the yellow arrows.

In Figure 4.26, it can be seen that the structure of the aluminum-steel interface varies in this section of Casting 28. The blue arrow on the left shows growth of an intermetallic phase from the steel pipe towards the cast aluminum. On the right side, the structure is recognized as the galvanized layer previously observed in Figure 4.20. Thickness of the galvanized layer is indicated by the black arrow and was measured to be approximately 70μm. A continuous crack is observed between the interfacial layer and the cast aluminum.

As seen in the image in Figure 4.25, one area of the interface appeared to have continuous bonding. Further investigation of this area was performed using EDS. The red circles in Figure 4.27 show the areas where the composition analysis was performed. The analysis results are presented in Table 4.9.

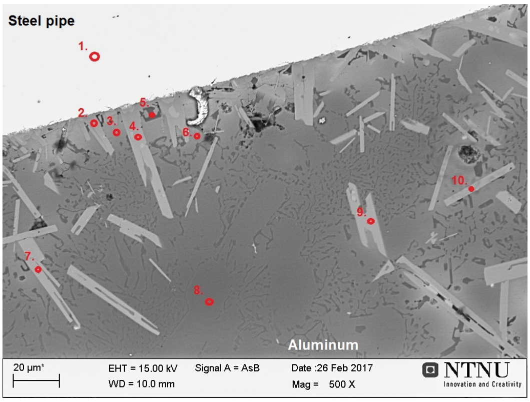

Figure 4.27: Micrograph of the aluminum-steel interface in Casting 28. Red circles indicate areas analyzed using EDS. Results from the EDS analysis are presented in Table 4.9.

Table 4.9: Chemical compositions and possible phases, analyzed using EDS, across the aluminum-steel interface in Casting 28 showed by red circled areas in Figure 4.27.

Area	Composition [at%]						Possible phase
	Al	Fe	Si	Zn	Mg	O	
1	-	100	-	-	-	-	Fe
2	62.12	17.10	16.38	1.40	-	-	$Al_{4.5}FeSi$
3	69.15	14.63	14.74	1.49	-	-	$Al_{4.5}FeSi$
4	89.15	1.35	-	9.51	-	-	(Al) + Zn
5	56.92	12.52	18.23	1.80	10.54	-	Al-Si-Fe-Mg phase
6	24.33	34.77	17.45	1.45	-	21.99	$Al_2Fe_3Si_3$
7	68.77	8.91	20.27	2.05	-	-	Al_3FeSi_2
8	97.94	-	-	2.06	-	-	(Al)
9	82.27	5.19	8.78	3.76	-	-	(Al) + $Al_{4.5}FeSi$
10	91.36	-	-	8.64	-	-	(Al) + Zn

The micrograph in Figure 4.27 shows that a sound metallurgical bond has formed between the steel pipe and cast aluminum. From Table 4.9, it is evident that aluminum was detected until the steel surface, thus indicating complete melting of the galvanized layer. Several particles with platelet structure are observed in the micrograph. Based on contrast, the particles appear to have similar compositions. However, the EDS results in Table 4.9 show that iron content decreases in particles further from the steel surface. Area 2 and 3 show similar compositions with ratios suggesting formation of ternary $Al_{4.5}FeSi$ at the steel surface. In Area 7, a similar particle appears to have composition coinciding with the ternary Al_3FeSi_2-phase. The particles can also be seen to have lengths varying from approximately 7μm to 50μm.

In Area 5 a significant concentration of magnesium is detected, which could indicate formation of a quaternary Al-Fe-Si-Mg phase. The composition does however not coincide with the known Al_5Si_2MgFe phase. Dark areas in the micrograph are most likely pores, which is confirmed in Area 6, where a large amount of oxygen is detected. The composition in this area does not coincide with any know ternary Al-Fe-Si phase. This could be due to oxygen impurity interfering with the analysis. However, it is suggested to be ternary $Al_2Fe_3Si_3$, which has the most similar composition compared to detected elements.

Hardness tests performed across the aluminum-steel interface in Casting 14 and 28 are presented in Figure 4.28. For Casting 14 hardness across two different interfacial sections were measured. Figure 4.28a shows a section where the galvanized layer remained unmelted, while Figure 4.28b shows a section where the galvanized layer melted and intermetallic phases formed.

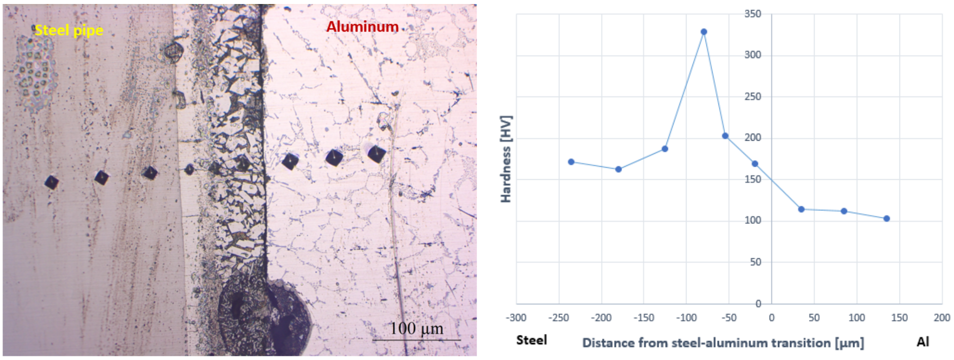

(a) Vickers hardness measured across the interface of a section in Casting 14 where the galvanized layer did not melt. Steel-aluminum transition is set as transition from the galvanized layer to cast aluminum.

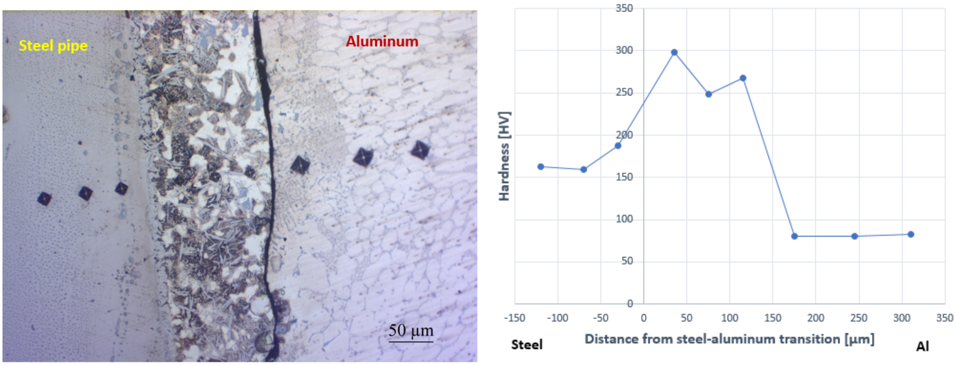

(b) Vickers hardness measured across the interface of a section in Casting 14 where the galvanized layer melted. Steel-aluminum transition is set as transition from steel to intermetallic layer.

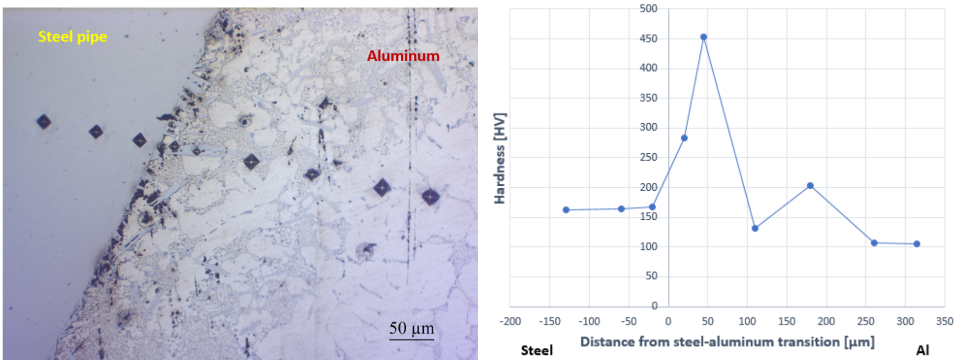

(c) Vickers hardness measured across the interface in Casting 28. Steel-aluminum transition is set as transition from steel surface to cast aluminum.

Figure 4.28: Vickers hardness measured across the aluminum-steel interface for two separate interfaces in Casting 14 and an interface in Casting 28.

Figure 4.28 shows that hardness increases in the interface for both castings. For the section in Casting 14 where the galvanized layer remained intact, hardness decreased in the layer towards the cast aluminum. In addition, the hardness measured in the galvanized layer adjacent to the steel surface is higher compared to the interface in which the galvanized layer melted. Adjacent to the cast aluminum, measurements in the galvanized layer had approximately similar value as measured in the steel pipe. For the second section in Casting 14, shown in Figure 4.28b, a slight increase in hardness is observed for the indentation in the steel pipe closest to the surface. This could imply that the intermetallic phase formed on the surface also might affect the nearby steel. Variations in the measured hardness are observed in the interface, which could be due to the inconsistent density of the needle-shaped particles observed. Higher hardness was measured in the interface of Casting 28 which also showed formation of needle-shaped particles. The second measurement on the aluminum side shows the hardness of one of these particles. It can be seen that this hardness is more than twice that of the steel pipe. Also worth noting is the increase in hardness observed for one of the positions in the cast aluminum. Based on the structure given in the optical micrograph in Figure 4.28c, the increase in hardness can be explained by the surrounding amount of eutectic silicon for the mentioned position.

4.3 Discussion

Different phenomena and results were observed for the aluminum-steel castings. These will be discussed separately in the following subsections.

4.3.1 Effect of Surface Treatment

Overall, none of the investigated castings showed proper metallurgical bonding throughout the aluminum-steel interface. However, several areas of local bonding indicated the effect of the surface treatment used on the steel pipes.

In Casting 17, several cavities were macroscopically visible as seen in Figure 4.1. The optical micrograph in Figure 4.2 showed that a large continuous gap separated the cast aluminum and the steel pipe, with only a small reaction area suggesting contact. The EDS analysis of this reaction area showed significant detection of oxygen in the interface. Although the formation of ternary $Al_{7.4}Fe_2Si$ indicates that a reaction has occurred between the cast aluminum and steel pipe, the oxygen present implies poor bonding. Oxides on the liquid aluminum surface will most likely vary in thickness, thus allowing reactions to occur in certain areas of the steel pipe. As the steel pipe loosened from the cast aluminum when cutting the thin section of Casting 17, the oxide layers most likely prevented wetting which caused only mechanical bonding. The thicker section probably showed formation of an intermetallic phase due to the thicker layer of cast aluminum allowing the temperature to stay elevated for a longer period, and thus increasing the possibility of iron diffusing.

When only using a galvanized layer, metallurgical bonding was achieved as seen in Figure 4.6. However, the intermetallic phase adjacent to the cast aluminum showed signs of porosities, seen in Figure 4.7. In some areas, large cavities were observed in the interface between the cast aluminum and the adjacent intermetallic phase, seen in Figure 4.8. This indicates that although intermetallic phases have formed, oxygen is still present in the interface which will prevent a continuous metallurgical bond. Casting 16 which had similar surface coating as Casting 15, a thin zinc-layer and flux coating, showed poor bonding. As provided in Table 4.7, both oxygen and flux residue remained in the interface which will cause discontinuous bonding. Due to Casting 15 and 16 having identical surface treatment, the bonding observed for Casting 15 in Figure 4.12 is believed to be a result of the subsequent heat treatment. The interface in Casting 32 strongly resembles the interface in Casting 15, seen in Figure 4.6 and 4.12 respectively, and thus it is possible that the bonding observed in Casting 32 also is a result of the heat treatment. Therefore, it is difficult to determine the effect of the galvanized layer alone. However, the observed porosities in the interface suggests that oxygen will be present in the interface when using galvanized steel pipes.

Casting 14 and 28 had a galvanized layer with flux coating. Although some defects were observed throughout the aluminum-steel interface, both castings showed areas of continuous metallurgical bonding. The section in Casting 14 where the galvanized layer did not melt, seen in Figure 4.23, shows good bonding with the cast aluminum. This would imply that the flux coating has been able to remove oxides and thus enhance wettability between the cast aluminum and the galvanized layer. Figure 4.24 shows a section in Casting 14 where the galvanized layer melted. Despite the obvious crack, no oxygen was detected in the interface which implies proper metallurgical bonding. The crack has most likely occurred upon solidification, and is thus not a direct result of the surface treatment. Casting 28 had sections where no bonding was apparent, as seen in Figure 4.26. However, local areas of continuous metallurgical bonding were observed in the casting, seen in Figure 4.27. Although the bonding observed in this section indicates that the flux coating has improved wettability, oxygen was detected in the interface. This could be a result of the higher pouring temperature and preheating temperature of the steel pipe in Casting 28 compared to Casting 14. This might cause thicker oxide layers to form, which will be more difficult to remove. Nonetheless, the combination of a galvanized layer and flux coating showed better bonding compared to the other surface treatments, despite bonding forming only in certain areas.

4.3.2 Variations in Interfacial Microstructure Within a Casting

Significant differences in the interfacial microstructure were observed within Casting 14, 16 and 28. This can be seen in Figure 4.22 and 4.23 for Casting 14, Figure 4.16 and 4.18 for Casting 16 and Figure 4.26 for Casting 28. The difference in microstructure is mainly due to the galvanized layer, or zinc-layer in Casting 16, melting or not. These differences were focused on in Casting 14. It is however likely that similar reasons caused the observed differences in Casting 16 and 28 as well.

Casting 14 was determined to portray best bonding from the castings investigated in the project assignment in the fall of 2016. This was believed to be due to the flux coating removing surface oxides on the aluminum melt, thus creating proper bonding between the cast aluminum and galvanized layer. In this project, the microstructure studied showed that when an unmelted galvanization layer exists, bonding between the galvanized layer and cast aluminum showed no defects, as shown in Figure 4.23.

Upon cutting Casting 14 along the longitudinal direction, an additional microstructure was observed. As seen in Figure 4.22, the interface included growth of an intermetallic phase on the steel surface as well as formation of needle-shaped particles. A continuous crack was also observed between the cast aluminum and the reaction layer, showing that proper bonding was not achieved throughout. As given in Table 4.8, aluminum detection in the reaction layer showed that the galvanized layer had melted and that there was contact between the cast aluminum and the steel surface. It is therefore likely that the crack occurred upon solidification.

Figure 4.22 and 4.23 show two areas from the interface in Casting 14 where the galvanized layer melted and remained intact respectively. Considering the binary Fe-Zn phase diagram in Figure 2.6, the pouring temperature of 700°C is above peritectic temperature for both ζ and δ, which are the first phases to form during hot-dip galvanization. This implies that melting of the galvanized layer should have occurred to some extent for both the interfacial areas. As it has not, the metal flow might have variations in temperature which cause variations in microstructure formed at the interface. It also implies the importance of sufficient temperature to obtain a reaction at the steel surface.

While the interface with remaining galvanization layer showed better bonding properties, hardness testing revealed higher hardness obtained for this interface as seen by comparing the measurements in Figure 4.28. However, higher hardness is only observed in the phase adjacent to the steel surface in the galvanized layer. This could indicate formation of multiple Fe-Zn phases, where the increased hardness might be related to the brittle δ-phase. In the reaction layer where the galvanized layer had melted, relatively high hardness was measured. As the reaction layer is thicker and showed formation of stress-inducing particles, the risk of fracture will probably be higher in this interface.

4.3.3 Effect of Galvanization Layer Thickness

The zinc-layer found on the steel pipe in Casting 16, showed high amounts of porosity and oxygen as seen in Figure 4.10 and Table 4.5. Thickness of the layer was measured to approximately 12μm. In addition, a ZnO layer had formed on the steel surface. This could be detrimental to bonding, due to the low wettability and high melting temperatures of oxides. The presence of oxides is also likely to impact the hardness measurements. As seen in Figure 4.19, hardness increased in the zinc-layer compared to the steel pipe. Pure zinc have lower hardness than steel. Oxides are however, known to be hard and brittle. No binary Fe-Zn phases were found in the zinc-layer, indicating that the zinc-layer was not applied through the hot-dip galvanization process. This might also be due to the silicon content in the steel used for Casting 16, as seen in Table 4.1, lying in the Sandelin range [50]. Upon hot-dipping that might have resulted in an uncontrolled growth of the galvanization layer. The galvanized layer seen in Casting 28 however, showed the characteristic formation of binary Fe-Zn phases which occurs due to diffusion of iron atoms in the hot-dip galvanization process. Figure 4.20a and 4.20b show that thickness of the layer varied from 40μm to 165μm. As such large variations were measured over a small area, it is unknown if the variation continued throughout the whole pipe surface, which also makes it difficult to determine preferred layer thickness.

The images of Casting 16 in Figure 4.15 and Casting 28 in Figure 4.25, show defects in the interface. A higher number of cavities are however observed for Casting 28. This could be due to the higher preheating temperature causing thicker oxides on the steel pipe prior to casting. Areas where the galvanized layer had melted, were however found for both Casting 16 and 28 presented in Figure 4.18 and 4.27 respectively. Table 4.7 shows that growth of the binary Al_2Fe as well as the ternary $Al_{4.5}FeSi$ has occurred on the steel surface in Casting 16. This implies that the zinc-layer has melted, meaning that wetting must have taken place. However, the interface displays several dark areas believed to be either trapped oxygen or flux residue, which could be a result of the high oxygen concentration detected in the zinc-layer. The flux coating might not be sufficient enough to remove oxides from both the cast aluminum and steel pipe surface, which will result in a decreased interfacial strength. In addition, no smooth transition from the cast aluminum melt to the reaction layer can be observed in Figure 4.18, which indicates that the bonding is poor. Nonetheless, the reaction layer is quite narrow measuring approximately 30μm, which will overall be beneficial in achieving a strong bond between the two materials. This would imply that if a thin zinc-layer with less oxygen was used, better bonding could be achieved and the reaction layer would be less detrimental to the bonding strength than observed for thicker intermetallic layers.

Considering the micrograph for Casting 28 in Figure 4.27, a sound metallurgical bonding without significant defects in the interface was found. Although formation of ternary needle-shaped particles also formed here, their composition did not always coincide with the brittle $Al_{4.5}FeSi$. Oxygen was detected adjacent to the steel surface, showing that the interface was not ideal. Nevertheless, no flux residue or excessive amounts of zinc were detected. This implies that when functioning optimally the flux will cause wetting in which melting of the galvanized layer can occur and a solid metallurgical bond can form. As seen from the hardness testing in Figure 4.28c, despite the intermetallic phases formed having significantly higher hardness, the reaction area is below 100μm. Although this is over three times thicker than for Casting 16, based on structure of the interface it is believed that a proper galvanization layer with flux coating is better than a thin zinc-layer with flux coating.

4.3.4 Effect of Heat Treatment

Casting 15 and 32 were both subjected to the T6 heat treatment subsequent to casting. The interface in Casting 15 shows large areas with poor wetting where no bonding has occurred, as well as several cavities. Process parameters, presented in Table 4.2, were almost identical to Casting 16 which as mentioned displayed rather few defects in the interface. The temperature used in the solution heat treatment, 540°C, is higher than the melting point of zinc and the peritectic point of the binary $Zn_{13}Fe$ phase. This implies that parts of the interface might remelt and cause oxygen to gather into larger sections, which could explain the difference in the interface in Casting 15 and 16. A similar effect might be seen for Casting 32 in Figure 4.5, but not to the same extent.

By comparing the optical micrographs for Casting 15 and 32, in Figure 4.12 and 4.6 respectively, several similarities were detected. Upon solution heat treatment, the eutectic silicon has spheroidized in both castings. However, no significant coarsening has occurred. This indicates that the solution heat treatment has not been excessive, which will benefit the mechanical properties of the cast aluminum. Coarse silicon particles, being brittle, could reduce ductility and increase internal stress due to the crystal structure being different than aluminum. Another similarity in the two castings, is the growth of a reaction layer on the steel surface. As the optical micrographs show, the intermetallic layer on the steel surface is somewhat uniform, while the one adjacent to the cast aluminum displays a tongue-like morphology. Thickness of the overall reaction layer however, varies in the two castings. As also seen in the optical micrographs from the hardness measurements in Figure 4.9 and 4.19, the reaction layer for Casting 32 is approximately twice that of Casting 15. This could be due to the thickness of the galvanized layer in Casting 32 resulting in a thicker reaction layer, and thus a larger fraction of intermetallic phase formation.

In the optical micrograph for Casting 15 in Figure 4.12, a crack can be seen outside the intermetallic layer. This is believed to have occurred during casting as growth of the intermetallic phases most likely occurred upon heat treatment. The micrograph given in Figure 4.14 and EDS results in Table 4.6 show that a flux residue layer remains outside the intermetallic phases. Potassium and fluoride are salts, which will be brittle and are likely to crack upon solidification shrinkage. In addition, oxygen was detected outside the formed $Al_{7.4}Fe_2Si$-phase where a porous structure was observed. This shows that the heat treatment did not improve wettability of the flux coating.

For Casting 32 a continuous crack formed in the intermetallic layer on the steel pipe as seen in Figure 4.7. EDS results from Table 4.4 conclude that two different phases have formed in the intermetallic layer on the steel surface, despite no apparent contrast change. Hardness measured for Casting 32 in Figure 4.19 might also confirm this, as the hardness significantly varies for the two indentations in the mentioned intermetallic layer. As these appear on each side of the crack, it could imply that the crack occurred after heat treatment. Assuming that the ternary $Al_{7.4}Fe_2Si$ forms on the steel surface upon casting, then brittle Al_3Fe forms as a result of increased diffusion of iron atoms upon heat treatment. $Al_{7.4}Fe_2Si$ and Al_3Fe have different shrinkage upon solidification. Quenching to 70°C might then cause a fracture in the interface between the two phases. Ternary Al_3FeSi_2 is believed to have formed during casting, based on the low concentration of silicon observed in the cast aluminum adjacent to the intermetallic layer in Figure 4.9.

Hardness measurements for both Casting 15 and 32, in Figure 4.19a and 4.9 respectively, show that hardness of the cast aluminum has increased to almost similar value as for the steel pipe. Compared to hardness tests for the other castings in Figure 4.4, 4.19b and 4.28, no difference in hardness was measured for the steel pipe. As the solution heat treatment temperature was 540°C, it is not sufficient for the microstructure in steel to change, thus no increased hardness could be expected. Comparing these four figures also show that, disregarding the unmelted galvanization layer, reaction layers are thicker for the heat-treated castings. In addition, hardness of the intermetallic phases forming are significantly higher. Hardness is often connected to brittleness, which would imply that although strength has increased for the cast aluminum, a thicker, more brittle interface has resulted from the heat treatment. This could prove to be more detrimental to bonding strength than the positive strength increase in the cast aluminum.

4.3.5 Formation of Silicon Particles

A silicon particle was detected in Casting 14, as seen in Area 8 in Table 4.8. Several particles with similar shape and contrast were observed nearby the determined particle in Figure 4.24, implying that these also were silicon. As A356 is a hypoeutectic alloy considering the binary Al-Si system, final structure is expected to be eutectic Al-Si and aluminum solid solution, (Al). However, as reported by Wang et al., formation of silicon particles has been observed in hypoeutectic alloys [12].

Wang et al. suggested that the undercooling effect at the solid/liquid interface of nucleated (Al) caused nucleation of silicon. In the micrograph in Figure 4.24, most particles have formed adjacent to areas with high concentrations of zinc. Zinc has a melting temperature of 420°C, meaning that it will remain in a molten state when aluminum starts to nucleate.

Amount of nucleated aluminum will increase, which might cause segregation of the molten zinc. Therefore, an undercooling effect could result from the nucleated aluminum/molten zinc interface, causing silicon to nucleate and grow upon further cooling.

Silicon particles formed in Figure 4.24 appears to lie adjacent to a crack, where some also have been fractured during crack formation. The particles are relatively large and as silicon is known to be brittle, there is a chance that the crack originated in a silicon particle and propagated further through the particles. Due to coarseness and different orientation compared to the cast aluminum, internal stress might form around the particles, which make them prone to fracturing upon solidification.

Only Casting 14 showed detection of silicon particles. Based on the process parameters given in Table 4.2, the main difference compared to the other castings, is that a lower metal pouring temperature was used. With a lower pouring temperature, time before reaching the liquidus line for aluminum decreases. Therefore, silicon can nucleate and grow. In addition, a lower pouring temperature might cause less diffusion of zinc into the cast aluminum, thus allowing for segregation to occur upon solidification.

4.3.6 Formation of Ternary $Al_{4.5}FeSi$

Formation of the ternary eutectic $Al_{4.5}FeSi$ phase was observed in Casting 14, 16 and 28. This phase is usually one of the dominant phases to form under normal cooling [40]. The investigated castings were all air cooled, allowing formation of a eutectic structure. Area of formation varied in the three castings. For Casting 16, seen in Figure 4.18, ternary particles formed on the steel surface. Iron present in the interface would be due to diffusion from the steel surface as no iron was detected in the zinc-layer. This could explain why particles only were observed at the surface. In Casting 14 and 28, Figure 4.24 and 4.27 respectively, particles formed in the interface. When the galvanized layer melts, iron from the binary Fe-Zn phases will be present in the interface and thus eutectic particles can form upon air-cooling. For Casting 28, particles were also observed at the steel surface. This could be due to higher preheating and pouring temperature causing increased diffusion of iron atoms compared to Casting 14.

$Al_{4.5}FeSi$ has a characteristic platelet structure, which often projects as a needle-shape in micrographs. This type of structure can cause internal stress which could weaken the interfacial strength. In addition, the phase is considered brittle which makes a high density of $Al_{4.5}FeSi$ both prone to fracturing and further propagation of the fracture. If present, small particles will be the least detrimental to the interface. By comparing lengths of the particles formed, it was found that the largest particle observed in Casting 28 was approximately 20μm longer than those in Casting 14 and 16. Compared to Casting 14, this could be due to the higher metal pouring temperature causing a slower cooling rate which then allows further diffusion and growth of the ternary phase. In Casting 16, as mentioned, formation of the ternary phase is due to diffusion of iron atoms from the steel surface, which will be more limited than similar atoms in a melt. For the heat treated castings, Casting 15 and 32, no formation of $Al_{4.5}FeSi$ was observed in the interface, likely due to some remelting in the interface which would cause further diffusion thus allowing more iron-rich phases to form.

4.4 Conclusions

No surface treatment caused poor bonding, with high detection of oxygen in the interface. When using galvanized steel pipes, pores were observed between the formed reaction layer and the cast aluminum. The zinc-layer detected showed high amounts of porosity. Thickness of this coating was significantly smaller than that measured in the galvanized samples, which provided a thinner reaction layer. However, the interface was filled with flux residue and oxides, showing that this combination of surface treatments was non-beneficial. The best bonding properties were achieved when using galvanized steel pipes with flux coating.

The interfacial microstructure varied in different areas of the castings. This implied temperature variation during the casting process. Without the melting of the galvanized layer, less oxygen was observed in the interface. Hardness tests showed that higher hardness was measured in the galvanized layer compared to the reaction layer that formed when the galvanized layer melted. Tests also showed that the hardness remained increased over a thicker section where a reaction layer formed.

Formation of needle-shaped $Al_{4.5}FeSi$ particles were observed in the interface of the non-heat treated castings. Lengths of the particles were found to increase when higher metal pouring temperature and preheating temperature of the steel pipe were used. Silicon particles also formed in the interface. These were believed to have nucleated due to an undercooling effect in the interface between molten zinc, which remained in the reaction area, and nucleated aluminum.

Heat treatment increased the hardness of the aluminum alloy, whereas the steel pipe showed no difference. In addition, the T6 process caused spheroidization of the eutectic silicon, and increased thickness of the reaction layer. No formation of the eutectic $Al_{4.5}FeSi$ phase was observed for the heat treated castings, but brittle Al_3Fe formed on the steel surface. Therefore, heat treatment was deemed non-beneficial for bonding strength.

Chapter 5

Lab Scale Shape Casting of Steel Rod and Aluminum A356

5.1 Experimental

An S355J2 steel rod was used to prepare inserts with cone and blunt ends. Composition of the steel is given in Table 5.1 [76].

Table 5.1: Chemical composition for S355J2 steel [76].

Element	C	Si	Mn	P	S	Cu	Fe
wt%	≤0.24	≤0.55	≤1.60	≤0.025	≤0.025	≤0.55	bal.

In total seven cone-end inserts with length of 88mm and a 45° cone angle, as well as 20 55mm long blunt inserts were made. Both types had a diameter of 27.6mm. Shape and measurements of the steel inserts are shown in Figure 5.1.

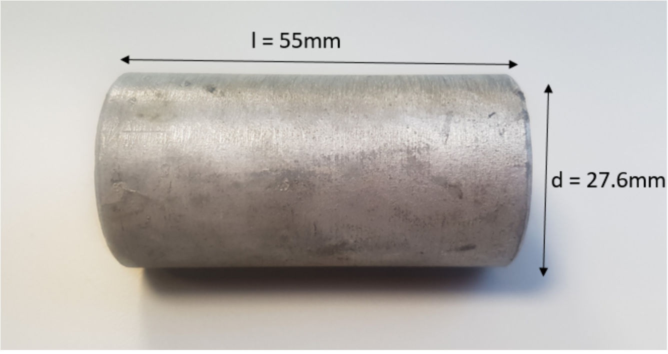

(a) Measurements of steel inserts with blunt end.

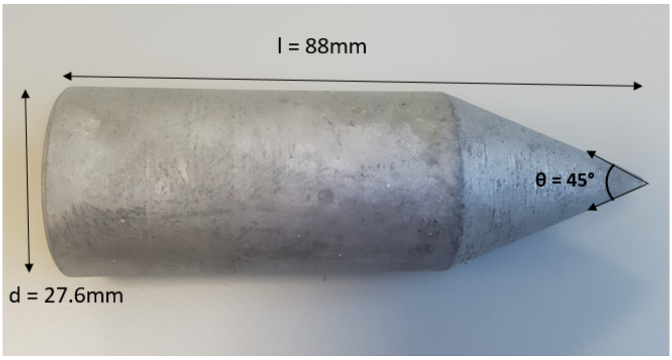

(b) Measurements of steel inserts with cone end.

Figure 5.1: Prepared steel inserts with measurements for the lab scale shape casting experiment.

5.1.1 Steel Insert Preparation

All inserts were galvanized after machining. The galvanization process was performed by an external company, FerroZink. This procedure included pre-treatment of the inserts in acidic baths followed by hot-dip galvanizing in a centrifuge, leaving a galvanized layer on the steel inserts. After galvanization, the inserts were cleaned with a 76vol% ethanol solution.

Half of each shaped insert was then painted with an aqueous solution of Nocolock® Cs flux. 5.2g flux was mixed with 10.2g of water, making a flux concentration of approximately 51%. To obtain a thin uniform layer, a small paintbrush was used. The inserts were then left to air-dry before casting.

5.1.2 Casting

A356 aluminum alloy was melted in a Morgan furnace with a set temperature of 815°C. A steel mold with geometry as shown in Figure 5.2 was used. A Tool-Temp oil aggregate was connected to the mold to provide heating. Two thermocouples were also connected to the mold, one to the top half and one to the bottom, to ensure constant temperature of 280°C. The steel insert was placed in one end of the mold as shown in Figure 5.2. In the other end a small steel bolt was placed to prevent spilling.

Figure 5.2: Casting mold used in lab scale shape casting experiment. The yellow area indicates placement of the steel inserts.

Molten metal was removed from the furnace with a ladle. A thermocouple was used to measure temperature before pouring. Metal was poured with a constant rate to guarantee complete filling of the mold. For some castings, argon gas was filled into the mold by using a plastic tube and a flow rate of approximately 5 L/min. The gas tube was then removed instantly prior to pouring. Other castings had inserts which were preheated to approximately 100°C by being placed on the furnace surface. Due to process complications, the casting parameters varied consecutively. These are summarized for each casting in Table 5.2.

Table 5.2: Process parameters for each lab scale shape casting.

Casting number	Insert shape[a]	Surface treatment[b]	Argon prior to pouring	Preheating[c]	Pouring temperature [°C]
A	B	G	50sec	None	751
B	B	G	None	None	758
C	B	G	None	None	760
D	B	G	1min	None	760
E	B	G	1min	None	770
F	B	G	1min	5min	770
G	B	G + F	1min	None	775
H	B	G + F	1min	None	770
I	B	G + F	1min	None	765
J	B	G + F	1min	100°C	760
K	B	G	1min	280°C[d]	790
L	B	G	2 min	100°C + 2 min	769
M	B	G + F	2 min	100°C + 2 min	775
N	C	G + F	1min	100°C + 2 min	750
O	C	G + F	1min	100°C	774
P	C	G + F	<1min	100°C	772
Q	C	G + F	1min	100°C + 3 min	774
R	C	G	1 min	100°C	772
S	C	G	2 min	100°C + 2 min	762
T	C	G	3 min	100°C + 3 min	768

[a] B-Blunt, C-Cone
[b] G-Galvanized, F-Flux coating
[c] Minutes indicate time in mold prior to pouring
[d] Insert placed in mold for 1h, assumed to have mold temperature

5.1.3 Sample Preparation

Castings with cone-shaped steel inserts which remained bound upon mold removal, were sent to the NTNU workshop for cutting in half along the length direction. A selection of castings was then cut to smaller samples using a Struers Labotom-15 with blade 40A35. After cutting the samples were mounted, using either Epofix or Claroxin. Epofix had a mixing ratio of 25 parts resin and 3 parts hardener, whereas for Claroxin 10 parts powder and 6 parts liquid hardener was used. All were measured by weight. Samples were ground using a Struers LaboPol-21 from grinding paper 220 to 4000 grits, followed by polishing on a Struers Tegramin-20 with DiaPro Mol B 3μm diamond suspension followed by DiaPro Nap B 1μm diamond suspension until no scratches were observed on the sample surface in an optical microscope. Between polishing, samples were cleaned with soap and water followed by 96vol% ethanol. They were then placed in a beaker filled with 96vol% ethanol and lowered into the bath of a 5510 Branson ultrasonic cleaner for five minutes, to prevent larger diamond particles from contaminating the polishing papers. Finally, the samples were placed in a Memmert drying oven at 74°C for overnight degassing before SEM analysis.

5.1.4 SEM Analysis

A Zeiss Supra 55VP field emission scanning electron microscope was used to take high magnification micrographs of each sample. An acceleration voltage of 15kV was used, while the working distance was set to 10mm. Both secondary electron images and backscattered electron images were captured. The backscattered electron micrograph was in addition used to perform energy-dispersive X-ray spectroscopy and line scans of the samples.

5.1.5 Tempering

Casting N, O and S were tempered using a Nabertherm P300 furnace. Each casting was heated separately for 15 minutes at 540°C and then left to air-cool.

5.2 Results

Results will be presented in two sections, based on shape of the steel inserts used in the casting experiment.

5.2.1 Blunt Steel Inserts

As presented in Table 5.2, process parameters for each casting differed slightly. The resulting bonding from each casting is given in Table 5.3. Applied force mentioned in this table indicates human force applied to the casting to verify the bonding strength.

Table 5.3: Results from each casting using blunt steel inserts under the lab scale shape casting experiment.

Casting	Resulting bonding
A	Good after mold removal, broke when force applied.
B	No bonding apparent
C	No bonding apparent
D	Broke during mold removal
E	Broke during mold removal
F	Good after mold removal, broke when force applied
G	Broke during mold removal
H	Broke during mold removal
I	Broke during mold removal
J	Broke during mold removal
K	Broke during mold removal
L	Good after mold removal, broke when force applied
M	Broke during mold removal

Table 5.3 shows that overall, no casting with strong bonding was made. For Casting B and Casting C argon gas was not used. This resulted in the steel insert loosening from the cast aluminum alloy upon opening the mold. No contact between the two could be observed, and thus the necessity of argon in the mold was determined. Process parameters for Casting A, F and L, differed slightly. However, neither one of them had an applied flux coating, indicating that the flux coating was non-beneficial for this casting process. These castings were still connected upon removal from the mold. Nevertheless, when human force was applied to the bimetallic casting, the two metals broke apart suggesting only mechanical bonding. Also worth noting is that increasing temperature of the poured aluminum melt and preheating temperature of the insert showed no difference in the resulting bonding, as seen for Casting K and Casting M. An image representing a casting which broke during mold removal is shown in Figure 5.3.

Figure 5.3: Image of a casting with blunt steel insert which broke upon mold removal.

Although none of the castings show good bonding, some results are worth further investigation. The aluminum surface which had been in contact with the steel insert, showed varying surface topography based on surface treatment of the steel insert. Difference in the aluminum surface for castings with only galvanization and with an additional flux coating is shown in Figure 5.4, represented by Casting E and Casting I respectively. Casting K, which was preheated to approximately 282°C also showed some interesting features and is therefore included in Figure 5.4.

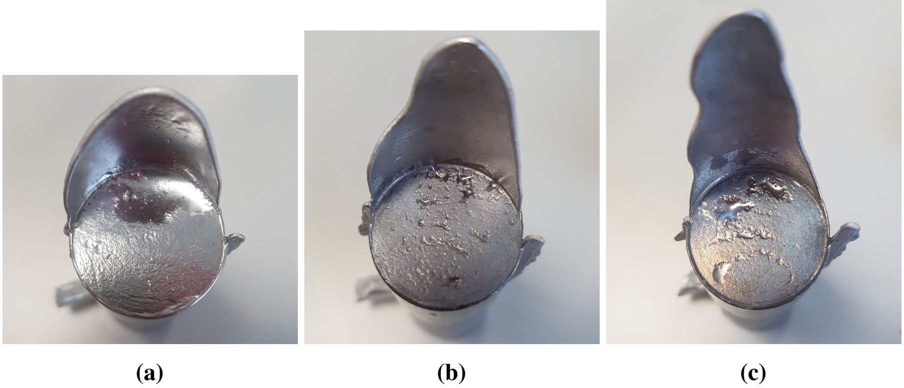

(a) **(b)** **(c)**

Figure 5.4: Images showing the aluminum surface from Casting E, I and K.
(**a**) Image of aluminum surface from Casting E, without flux coating. A large indent from entrapped gas can be seen on the upper half of the surface.
(**b**) Image of aluminum surface from Casting I, with flux coating. Several pores can be seen throughout the surface.
(**c**) Image of aluminum surface from Casting K, without flux coating but with elongated preheating. Several pores can be seen throughout the surface.

Figure 5.4 shows that for Casting E, where no flux coating was applied, a large indentation can be observed on the aluminum surface. This indentation represents almost a third of the surface, and suggests entrapment of gas resulting in a relatively large bubble. When flux coating was applied to the steel insert, the opposing aluminum surface shows a different topography as seen for Casting I. Instead of one large indentation, several small have formed throughout the surface. These have a characterization more similar to pores. Overall, the indentation area is considerably smaller in Casting I compared to Casting E, suggesting that the flux has functioned to some extent. For Casting K, which had no flux coating, the aluminum surface appears to have a structure more similar to that of Casting I. Several pores can be seen throughout the surface. Although they are slightly larger than observed for Casting I, it seems as if less gas has been entrapped compared to Casting E. The increased length of overflow in Casting K is most likely due to both increased insert and pouring temperature.

To determine if any reaction had occurred in Casting I, the aluminum surface was investigated using SEM and EDS. The micrograph in Figure 5.5 shows the structure of a section in the aluminum surface. Red circles indicate areas which were analyzed using EDS. Results from this analysis are presented in Table 5.4.

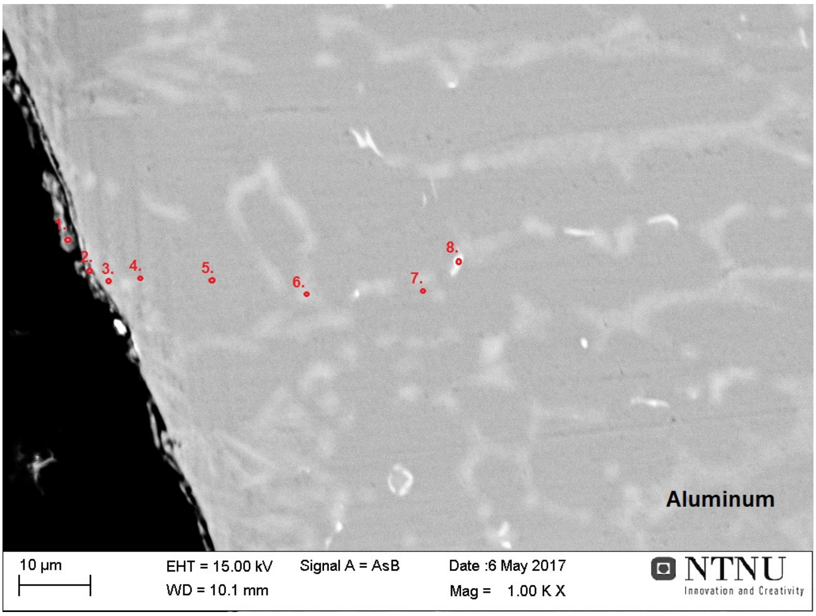

Figure 5.5: Micrograph of the aluminum surface in Casting I. Red circled areas were analyzed using EDS. Results from the analysis are presented in Table 5.4.

Table 5.4: Compositions and possible phases, analyzed using EDS, on the aluminum surface in Casting I showed by red circled areas in Figure 5.5.

Area	Composition [at%]								Possible phase
	Al	Si	Mg	K	Cs	F	O	Ar	
1	55.51	15.01	2.62	1.32	-	8.76	16.78	-	Flux residue
2	29.15	9.88	8.95	5.25	1.15	28.18	17.44	-	Flux residue
3	83.47	12.63	1.30	-	-	-	-	2.60	Eutectic Al-Si
4	95.33	0.94	-	-	-	-	-	3.73	(Al)
5	96.28	-	-	-	-	-	-	3.72	(Al)
6	55.52	44.48	-	-	-	-	-	-	Eutectic Al-Si
7	61.18	32.82	-	-	-	-	-	-	Eutectic Al-Si
8	80.13	17.36	-	-	-	-	-	2.52	Eutectic Al-Si

Figure 5.5 shows that there are some irregularities on the aluminum surface, as was previously observed as pores in Figure 5.4. In addition, a thin discontinuous layer can be observed on the surface. Compositions found for Area 1 and Area 2 in Table 5.4 show detection of potassium, cesium and fluoride, suggesting that this layer is flux residue. This indicates that there has been some reaction between the flux and the cast aluminum. However, the relatively high percentage of oxygen identified in these areas implies that the flux has not functioned properly as an oxide remover. Also worth noting is the detection of magnesium in Area 1 and Area 2, which in both cases significantly exceeds the magnesium content in the A356 alloy. Magnesium was also found in Area 3, but to a much smaller degree. Areas 4, 5, 6, 7 and 8 showed characteristics of eutectic Al-Si, with higher silicon content measured in the areas where eutectic silicon could be observed in Figure 5.5. Argon was also detected in these areas, which would imply some diffusion of argon into the melt upon casting.

Since some of the castings only broke after a force was applied, EDS was used to determine if any melting of the galvanized layer had occurred. Line scans were performed on Casting E and G, where the latter had an additional flux coating. These were compared to an unused steel insert. Line scans performed over the galvanized layer of the unused insert, Casting E and G are shown in Figure 5.6.

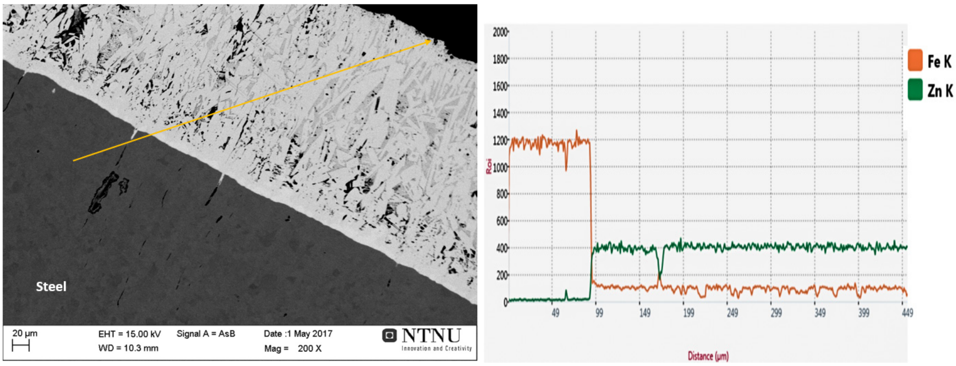

(a) Line scan performed across the galvanized layer in an unused steel insert.

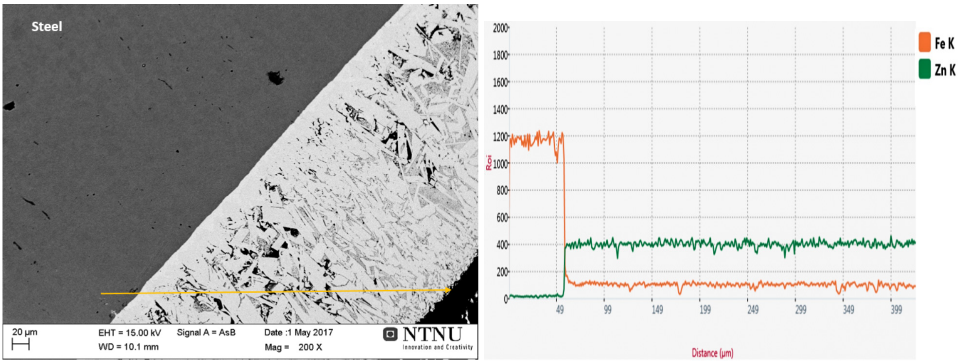

(b) Line scan performed across the galvanized layer in Casting E.

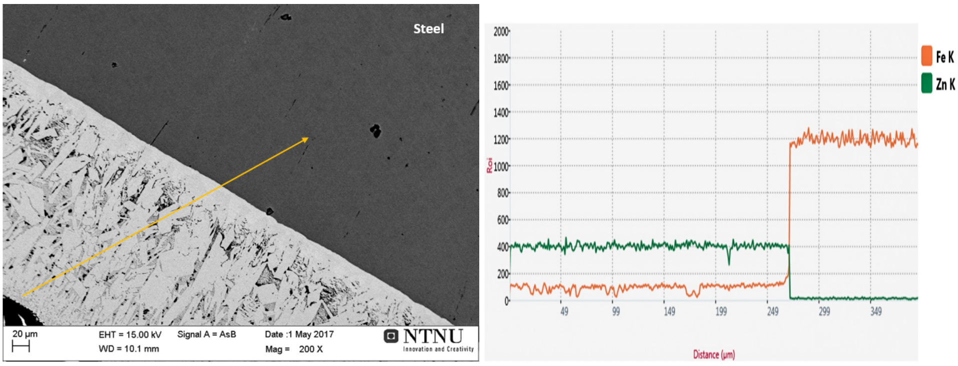

(c) Line scan performed across the galvanized layer in Casting G.

Figure 5.6: EDS line scan across the galvanized layer in an unused steel insert, Casting E and Casting G. The scan follows the yellow line. X-axis gives distance from starting point, whereas y-axis shows intensity of element detected. Elements found are designated with different colors given in the graph.

The line scans in Figure 5.6 show that the galvanized layer has similar composition on both used and unused inserts. Iron, given by the orange line, is detected and remains relatively constant throughout the layer. This indicates formation of a binary Fe-Zn phase. Based on the structure observed in the micrographs, the binary phase has grown into large columnar particles stretching from the steel surface. The layer also appears to be uniform, as no noteworthy variation is observed on the surface. In the unused steel insert, thickness of the galvanized layer was measured to be approximately 260μm. Compared to approximately 268μm and 253μm measured as layer thickness for Casting E and Casting G respectively, no significant difference exists. This implies that no melting of the galvanized layer has occurred for the castings.

A more thorough characterization of the galvanized layer was performed on the unused steel insert using EDS. Figure 5.7 shows a micrograph of the galvanized layer. Red circled areas were analyzed using EDS. Results from the analysis are provided in Table 5.5.

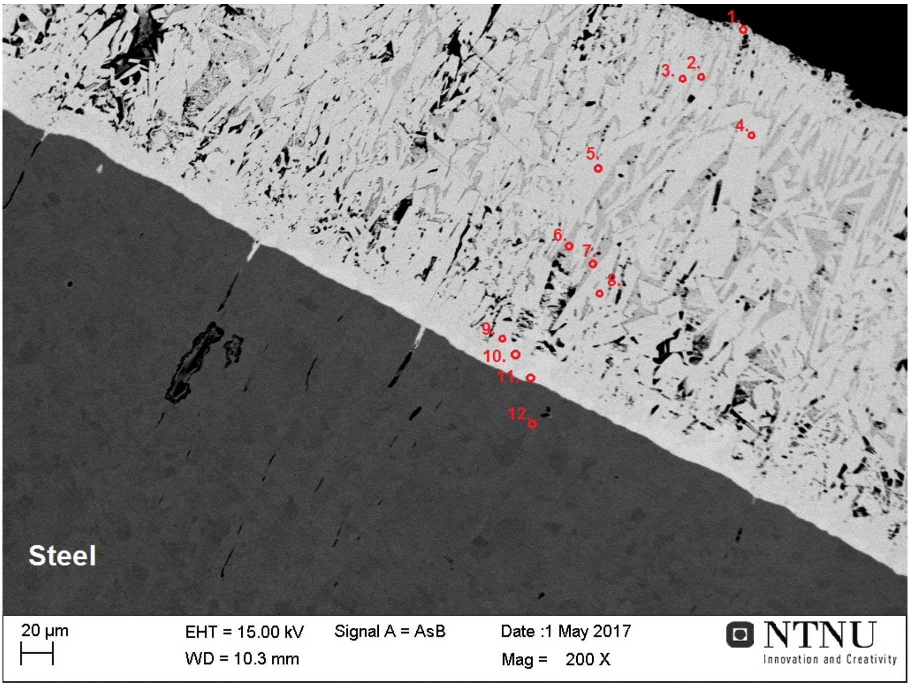

Figure 5.7: Micrograph of the galvanized layer on an unused blunt steel insert. Red circled areas were analyzed using EDS. Results of the analysis are presented in Table 5.5

Table 5.5: Compositions and possible phases, analyzed using EDS, across the galvanized layer of an unused blunt steel insert showed by red circled areas in Figure 5.7.

Area	Composition [at%]			Possible phase
	Zn	Fe	Mn	
1	100	-	-	Zn
2	93.09	6.91	-	$Zn_{13}Fe$
3	93.43	6.57	-	$Zn_{13}Fe$
4	93.43	6.57	-	$Zn_{13}Fe$
5	93.29	6.71	-	$Zn_{13}Fe$
6	100	-	-	Zn
7	100	-	-	Zn
8	93.43	6.58	-	$Zn_{13}Fe$
9	93.29	6.71	-	$Zn_{13}Fe$
10	93.16	6.84	-	$Zn_{13}Fe$
11	92.62	7.38	-	$Zn_{13}Fe$
12	-	98.35	1.65	Fe

Results given in Table 5.5 show that the compositions found in areas within a particle are similar. Area 2, 3, 4, 5, 8, 9, 10 and 11 imply that the particles formed in the galvanized layer are binary $Zn_{13}Fe$. Between particles and on the surface of the layer, only zinc was detected. This is given by the composition in Area 1, 6 and 7. No oxygen was detected in the layer. However, the micrograph in Figure 5.7 shows several black areas throughout the layer, especially adjacent to the steel surface where particles first start to form. These areas are believed to be oxygen or oxides, which would imply that the layer is not optimal.

5.2.2 Cone-Shaped Steel Inserts

Results from each casting using cone shaped steel inserts are presented in Table 5.6. As some of the steel inserts in several of the castings appeared to be bound with the cast aluminum, they were cut in half to investigate the aluminum steel interface. Results after cutting are also presented in Table 5.6.

Table 5.6: Results from each casting in the lab scale shape casting experiment using cone-shaped steel inserts, after casting and subsequent cutting.

Casting	Observed bonding after casting	Observed bonding after cutting
N	Good after mold removal	One half good after cutting
O	Good after mold removal	Both halves good after cutting
P	Good after mold removal	Both halves broke upon cutting
Q	Good after mold removal	Both halves broke upon cutting
R	Broke during mold removal	-
S	Good after mold removal	One half good after cutting
T	Good after mold removal	One half good after cutting

Table 5.6 shows that compared to the blunt steel inserts, the majority of the castings using cone-shaped steel inserts remained connected after casting. Casting R was the only casting in which the steel insert and cast aluminum were separated upon removal from the mold. From the process parameters given in Table 5.2, it appears that a combination of longer holding time and argon gas flow in the mold has improved bonding, as both Casting S and T showed good bonding properties after casting. All castings using flux coating displayed good bonding upon mold removal. However, upon cutting both Casting P and Q broke, implying only mechanical bonding in the interface. In Casting O, which had almost identical process parameters compared to Casting P, both halves remained intact after cutting. Halves from the castings which remained bound after cutting are shown in the image in Figure 5.8.

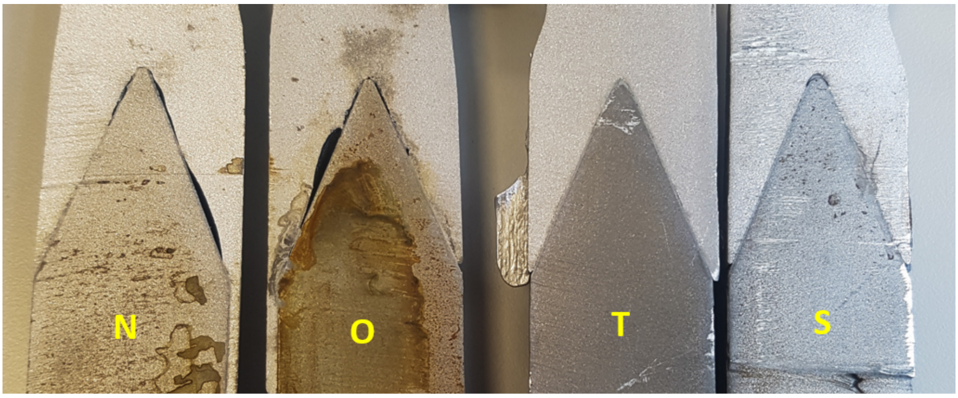

Figure 5.8: Image of Casting N, O, S and T after cutting.

As seen in Figure 5.8, Casting N and O have large cavities in the interface, most likely due to entrapped gas in these areas. These castings had a flux coating, which would imply that the flux has not functioned properly. However, areas of bonding with no detrimental gas impurity can be observed in other sections of the interface. Casting S and T show no defects in the interface. Instead, continuous bonding can be observed throughout Casting T and S, despite a small inclusion in the tip of the latter. This could also be due to cutting.

Casting O was further cut to investigate the aluminum-steel interface. Two different sections were cut to compare the temperature effect, one of the interface at the cone tip and one approximately at the middle of the cone. An image of the interface at the cone tip after grinding and polishing is shown in Figure 5.9.

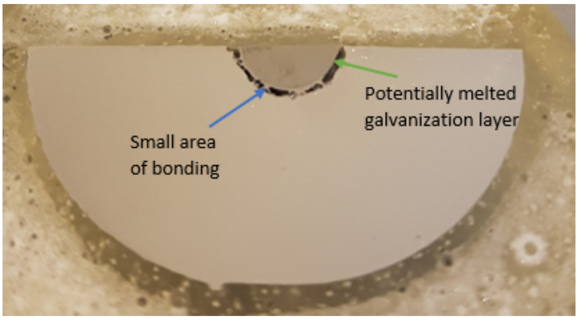

Figure 5.9: Image of the aluminum-steel interface at the cone tip in Casting O. A small area of bonding is shown by a blue arrow, whereas the green arrow indicates an area where the galvanized layer has melted.

Overall, Figure 5.9 shows that the bonding observed for Casting O in Figure 5.8 is not good. A large gap between the steel insert and cast aluminum can be seen almost throughout the interface. However, small areas of bonding, as the one indicated with a blue arrow, were observed. In addition, a thin layer with brighter color can be seen on the steel surface. This is believed to be the galvanized layer. As indicated by a green arrow, the thin layer cannot be observed around the entire steel surface, thus implying melting of the galvanized layer. To further determine if melting had occurred, an analysis of the interface using EDS was performed. A micrograph of the interface in Casting O is given in Figure 5.10. Results of the analysis of the red circled areas in Figure 5.10 are provided in Table 5.7.

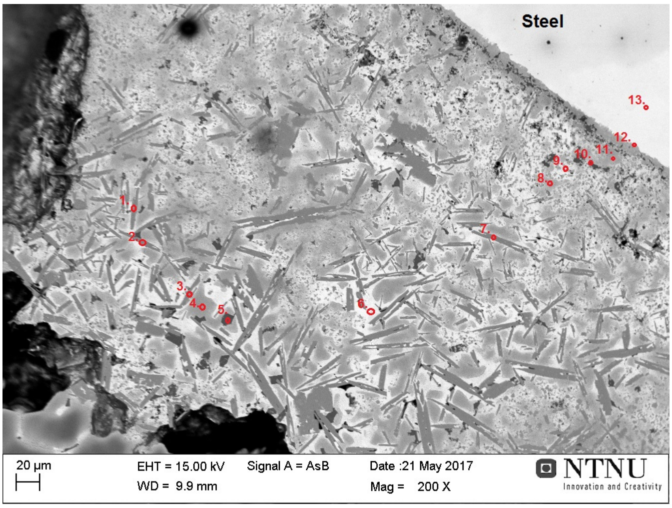

Figure 5.10: Micrograph of the aluminum-steel interface in a section at the steel cone tip in Casting O. Red circled areas were analyzed using EDS. Results from the analysis are presented in Table 5.7.

Table 5.7: Compositions and possible phases, analyzed using EDS, across the aluminum-steel interface in a section at the steel cone tip in Casting O showed by red circled areas in Figure 5.10.

Area	Composition [at%]					Possible phase
	Al	Si	Fe	Zn	Mn	
1	64.82	15.68	13.46	6.03	-	$Al_{4.5}FeSi$
2	64.83	17.11	15.41	2.64	-	$Al_{4.5}FeSi$
3	65.09	16.41	14.78	3.72	-	$Al_{4.5}FeSi$
4	79.30	-	-	20.70	-	(Al) + Zn
5	1.41	98.59	-	-	-	Si
6	43.77	-	-	56.23	-	(Al) + Zn
7	64.26	11.30	8.55	15.89	-	$Al_{4.5}FeSi$
8	74.03	-	-	25.97	-	(Al) + Zn
9	50.36	-	-	49.64	-	(Al) + Zn
10	32.05	53.14	-	14.81	-	(Al) + Si + Zn
11	77.95	-	-	22.05	-	(Al) + Zn
12	9.37	-	86.73	3.90	-	(Al) + Fe
13	-	-	95.89	-	4.11	Fe

Figure 5.10 shows that large needle-shaped particles formed locally in the aluminum-steel interface in this section of Casting O. These particles showed lengths varying from approximately 10μm to 112μm, with both length and density increasing as distance from the steel surface increases. Compositions found for Area 1, 2, 3 and 7 in Table 5.7, indicates that the needle-shaped particles are most likely ternary $Al_{4.5}FeSi$. As this phase has a characteristic platelet structure, this is believed to be correct despite detection of zinc in these areas. In Figure 5.10, large cavities can also be seen in the interface. However, a small area showing local bonding can be observed in the lower left corner. Detection of aluminum throughout the interface suggests that the galvanized layer has melted and that the bonding observed is metallurgical. Areas between the detected particles, show high concentration of zinc indicating incomplete melting and diffusion of the galvanized layer.

Several white areas were observed in Figure 5.10. Area 6 and 9 show that these areas have higher zinc concentration compared to adjacent grey areas, implying segregation of zinc. This appears to occur around the needle-shaped particles. Darker particles with more square appearance could be observed in the interface. Area 5, representing one of these particles, shows mainly detection of silicon suggesting formation of silicon particles. A dark area without any specific structure also showed high percentage of silicon, as seen in Area 10. Due to the additional aluminum and zinc detection in this area, it is most likely due to segregation of silicon rather than a silicon particle. Area 12, on the steel surface, has a composition that would suggest formation of binary Al-Fe. However, as no binary phases coincides with the element detection, the aluminum concentration is believed to be due to diffusion.

The interface observed when a section was cut from approximately the middle of the cone in Casting O is shown in Figure 5.11. The image was taken after grinding and polishing of the sample.

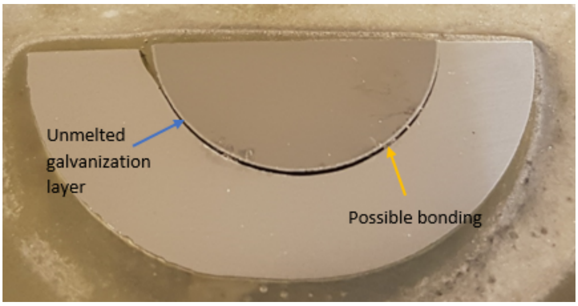

Figure 5.11: Image of the aluminum-steel interface at the middle of the cone in Casting O. A thin layer is observed on the steel surface, recognized as unmelted galvanization layer and indicated by a blue arrow. The yellow arrow shows an area of possible bonding.

Figure 5.11 shows a large continuous gap between the steel insert and the cast aluminum, indicating that no bonding has formed between the two. However, in certain areas, there appears to be material present in the gap, implying a possibility of local bonding in the area. One such area is indicated by the yellow arrow. A thin film, recognized as the galvanized layer can be observed on the steel surface, as noted by the blue arrow. The continuity of the film suggests that no melting of the layer has occurred in this section of Casting O. Further examination of the interface was performed using SEM, as seen in the micrograph in Figure 5.12. No bonding was found between the cast aluminum and the galvanized steel insert. Red circled areas in Figure 5.12 were analyzed using EDS. Results of the analysis are presented in Table 5.8.

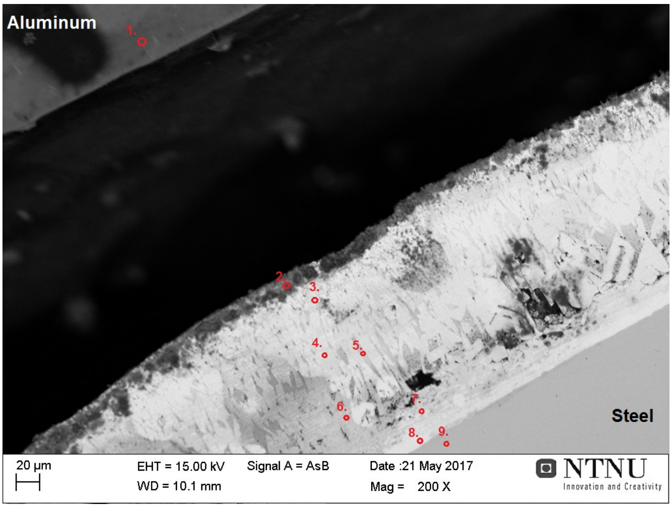

Figure 5.12: Micrograph of the aluminum-steel interface in a section of Casting O. Red circled areas were analyzed using EDS. Results from the analysis are presented in Table 5.8.

Table 5.8: Compositions and possible phases, analyzed using EDS, across the aluminum-steel interface in a section of Casting O showed in Figure 5.12.

Area	Composition [at%]					Possible phase
	Al	Fe	Zn	Ar	O	
1	98.25	-	-	1.75	-	(Al)
2	-	2.90	56.21	-	40.89	ZnO
3	-	6.89	93.11	-	-	$Zn_{13}Fe$
4	-	6.83	93.17	-	-	$Zn_{13}Fe$
5	-	-	82.21	-	17.79	Zn + O
6	-	6.77	93.23	-	-	$Zn_{13}Fe$
7	-	7.07	92.93	-	-	$Zn_{13}Fe$
8	-	11.08	88.92	-	-	Zn_7Fe
9	-	100	-	-	-	(Al) + Zn

The composition for Area 1 in Table 5.8 shows that a small concentration of argon was detected in the cast aluminum, suggesting some diffusion upon casting. A somewhat darker film can be seen on the surface of the galvanized layer. High concentration of oxygen measured in this film, as given by Area 2, implies formation of ZnO which could explain the poor bonding in the interface. Oxygen is also detected in Area 5, indicating presence of oxygen in the galvanized layer.

Figure 5.12 shows large particles in the galvanized layer. These were found to be the binary $Zn_{13}Fe$-phase, as seen from the compositions in Area 3, 4, 6 and 7. This coincides with the results found from the unused blunt steel insert in Figure 5.7. However, a second binary phase with higher iron content appears to have formed on the steel surface. Based on the composition found in Area 8, this phase is most likely Zn_7Fe. Nonetheless, the phases detected indicate that there has been no remelting of the galvanized layer.

Casting T was also further cut. However, when the tip was cut, the cast aluminum and steel insert separated from each other in the remaining part of the casting. This implied only mechanical bonding in this area of the casting. The tip, in which the steel remained bound in the cast aluminum, was ground and polished. An image was taken following this procedure, as shown in Figure 5.13.

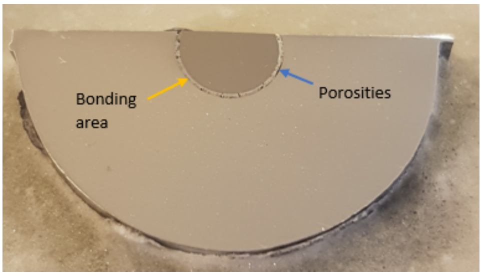

Figure 5.13: Image of the aluminum-steel interface in the cone tip of Casting T. Porosities can be observed in the interface as shown by the blue arrow. The yellow arrow indicates an area of bonding.

Figure 5.13 shows that compared to the interfaces in Casting O displayed in Figure 5.9 and Figure 5.11, no apparent gap is observed in Casting T. Instead, porosities were observed in the interface, as noted by the blue arrow. Based on color on the steel surface, it seems that the galvanized layer has not melted. Nonetheless, an area of bonding can be seen, as shown by the yellow arrow. To determine if bonding had occurred, a micrograph was taken of the interface. This is given in Figure 5.14. Composition of the red circled areas in the micrograph were analyzed using EDS. Results of the analysis are presented in Table 5.9.

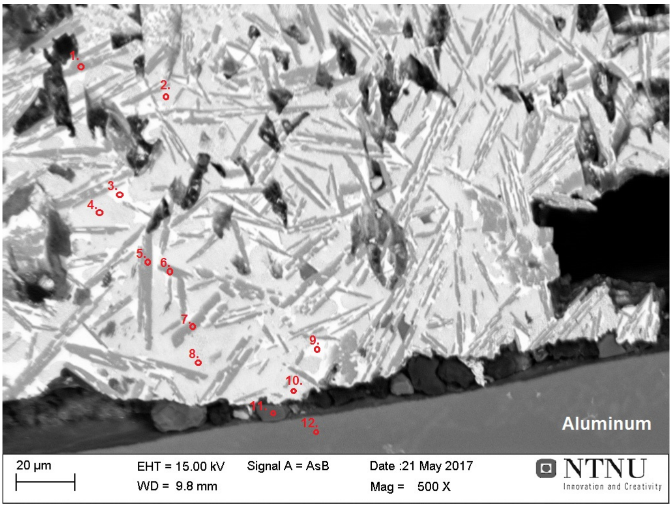

Figure 5.14: Micrograph of the aluminum-steel interface in the cone tip in Casting T. Red circled areas were analyzed using EDS. Results from the analysis are presented in Table 5.9.

Table 5.9: Compositions and possible phases, analyzed using EDS, across the aluminum-steel interface in a section at the steel cone tip in Casting T showed by red circled areas in Figure 5.14.

Area	Composition [at%]				Possible phase
	Al	Si	Fe	Zn	
1	61.14	17.99	16.48	4.39	$Al_{4.5}FeSi$
2	43.23	-	-	56.77	(Al) + Zn
3	6.21	-	-	93.79	Zn
4	41.40	-	-	58.60	(Al) + Zn
5	62.71	18.50	15.30	3.49	$Al_{4.5}FeSi$
6	64.72	16.94	15.46	2.88	$Al_{4.5}FeSi$
7	62.30	15.12	12.75	9.82	$Al_{4.5}FeSi$
8	44.29	-	-	55.71	(Al) + Zn
9	1.15	-	-	98.85	Zn
10	40.44	-	-	59.56	(Al) + Zn
11	1.04	98.96	-	-	Si
12	87.13	12.87	-	-	Eutectic Al-Si

Figure 5.14 shows that several needle-shaped particles formed in the interface. Based on compositions found in Table 5.9 for Area 1, 5, 6 and 7 these particles were believed to be the ternary $Al_{4.5}FeSi$ phase despite detection of zinc. The particles display varying length and thickness, where the former is difficult to determine due to porosities in the interface. Detection of aluminum in all analyzed areas indicates that the galvanized layer has melted. However, areas between the particles show high percentage of zinc. Area 3 and 9, which in Figure 5.14 are areas within the interface with the highest brightness, show mainly detection of zinc. This implies incomplete melting of the galvanized layer and thus reduced diffusion of zinc. On the cast aluminum surface, there appears to be formation of large dark particles. These prevent a smooth transition from the cast aluminum surface to the reaction layer, thus also preventing optimal bonding. Area 11, representing one of these particles, show high concentration of silicon suggesting formation of silicon particles on the aluminum surface.

Casting N and S, as well as the second half of Casting O were tempered as an attempt to increase the formation of a metallurgical bond between aluminum and steel. An image of the castings after tempering is shown in Figure 5.15.

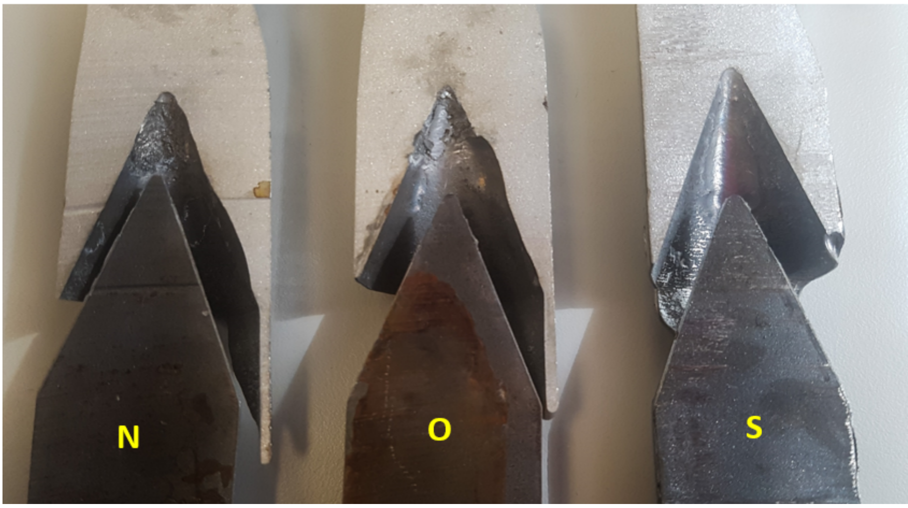

Figure 5.15: Image of Casting N, O and S after tempering. In all castings, the steel insert loosened from the cast aluminum.

As seen in Figure 5.15, for all three castings the steel insert loosened from the cast aluminum. Casting N and S loosened upon tempering, indicating that most likely only a mechanical bond had formed beforehand. Casting O only broke when human force was applied to it. However, this indicates that even though a bond might have formed, the bonding strength was not sufficient. Despite the castings loosening, possible reaction areas could still be observed on the steel insert and opposing aluminum part. Figure 5.16 shows the two separate metal parts for Casting N.

Figure 5.16: Image of cast aluminum and steel insert, from left to right respectively, for Casting N after tempering and breakage.

The cast aluminum part in Figure 5.16 shows a relative porous structure at the cone tip. By comparing the same area on the steel insert, it can be seen that both structure and color changes towards the tip. This could indicate that some melting of the galvanized layer has occurred. However, further down the cone, a somewhat smooth surface can be observed for both metal parts, except for some indentations in the aluminum part suggesting entrapment of gas upon casting. The smooth surfaces imply no reaction between aluminum and steel, and if bonding occurred it was only mechanical. This is most likely due to the temperature difference at the cone tip and further along the steel insert.

Similar observations were also made for Casting O after tempering. These can be seen in Figure 5.17.

Figure 5.17: Image of cast aluminum and steel insert, from left to right respectively, for Casting O after tempering and breakage.

As seen at the cone tip on the aluminum part in Figure 5.17, a piece of metal with different color is present. By comparing the same area on the steel insert, it appears as if the metal piece is from the galvanized layer. This implies that complete melting of the galvanized layer was not achieved as it still can be observed as a piece in the aluminum part. In addition, it indicates that the bonding between the galvanized layer and the cast aluminum is stronger than that between the layer and steel, as fracturing occurred in the latter upon applied force. The area on the steel insert adjacent to where the galvanized layer was removed, shows a porous structure. This suggests that some melting of the galvanized layer also occurred there. Remaining contact area between the two metal parts displays a smooth surface, implying only possibility for mechanical bonding believed to be due to the temperature difference, as also seen for Casting N.

5.3 Discussion

Various phenomena and observations will be subsequently presented under the following subsections.

5.3.1 Effect of Argon Gas

Flushing argon gas into the mold prior to casting was suggested as a method to reduce air, especially oxygen concentration in the mold cavity. It was believed that the argon gas, being heavier than air, would replace the latter in the mold. Thus, upon casting, less oxygen will be present which would reduce the oxide layer forming spontaneously on the liquid aluminum surface. This oxide layer will reduce wetting due to its thermodynamic stability, and therefore reduce chances of a metallurgical bond forming.

Table 5.3 shows that for Casting B and C, no bonding between the steel insert and cast aluminum was apparent. These were the only castings where no argon gas was used. For the castings using blunt steel inserts, no difference in bonding was observed by increasing flushing time prior to pouring. However, for the castings using cone-shaped steel inserts, better bonding was obtained when the flushing time increased. This can be seen by comparing Casting R with Casting S and T in Table 5.6, where the latter two had longer flushing time. However, it should be mentioned that Casting S and T also remained longer in the mold, which could have affected the results. Despite the increased bonding effect of argon, gas was still entrapped in the interface, as seen in Figure 5.4. It can thus be suggested that a continuous flushing of argon might remove oxygen to a greater extent, resulting in better bonding than achieved through this experiment. It is also worth noting that detection of argon was found in the cast aluminum in Casting I, seen in Figure 5.5. Although most of the gas will be pushed through the ventilation system, some argon atoms might diffuse into the liquid aluminum upon casting. The extent of argon diffusion is however so small that it will not affect the solidified aluminum structure.

5.3.2 Effect of Temperature on Blunt Steel Inserts

Comparing the process parameters in Table 5.2 with bonding results using blunt steel inserts in Table 5.3, no difference in bonding strength could be connected to metal pouring temperature. Preheating the steel inserts to temperatures varying from 100°C to 280°C, also proved to have no effect on final bonding properties. However, characterization of the galvanized layer on an unused steel insert, shown in Figure 5.7 and 5.5, showed formation of the binary $Zn_{13}Fe$ with remaining parts of the layer containing pure zinc. Zinc has a melting temperature of 460°C, while the peritectic temperature of $Zn_{13}Fe$ is 530°C as seen in the binary Fe-Zn phase diagram in Figure 2.6. Pouring temperatures of the liquid aluminum alloy exceeded both of these temperatures, which should cause melting of the galvanized layer. However, as observed for the line scans in Figure 5.6, similar structure and compositions as in the unused insert are detected for both Casting E and G, with and without flux coating respectively. Even though slight variations were measured for thickness of the galvanized layers, they were all within a 20μm range, which suggests that variations were caused during the galvanization process.

Based on density, steel has much higher heat capacity than aluminum. This implies that a high amount of energy will be needed to heat the steel insert. If the inserts are not preheated to a required extent, the massive insert front will cause aluminum to rapidly solidify upon contact. The temperature will therefore not be sufficient for the galvanized layer to melt and create metallurgical bonding. Although the melt temperature probably is higher at pouring than when in contact with the steel insert, the insufficient temperature of the steel insert will most likely be most detrimental to bonding.

5.3.3 Gas Entrapment in the Aluminum-Steel Interface

Figure 5.4 shows the different topographies observed for castings with various surface treatment and preheating temperature. In Casting E, representing the trend observed for all aluminum parts opposing a galvanized blunt steel insert, a large indentation covering approximately a third of the surface was observed. The indentation is believed to be entrapped air. During casting, molten metal will fill the mold and in the process push air or argon gas through the ventilation system. As such a large indentation can be seen in the aluminum-steel interface, it suggests that ventilation is not optimal and, as mentioned, that argon is not able to remove all air present in the mold. For Casting I, where the opposing steel insert had a flux coating in addition to being galvanized, several small pores were instead observed on the aluminum surface. NOCOLOK® Cs flux has a melting range of 558°C-566°C [73], at which temperature the binary ζ-phase found in the galvanized layer should start to dissolve. As discussed in the previous subsection, no melting of the galvanized layer had occurred. The flux layer is rather thin, and therefore it is possible that the temperature has been high enough for the flux to activate despite no evident melting of the galvanized surface. However, as the heat capacity of steel will cause immediate solidification of the cast aluminum, the flux will not be able to function properly. This can be seen by the pores scattered across the aluminum surface in Casting I. In Figure 5.5, showing a micrograph of this surface, a thin layer of flux could be seen in some areas. However, as given in Table 5.4, detection of flux elements was only found on the surface and there appears to be poor connection between the two. This could indicate that the flux indeed has melted, but not reacted properly, as also suggested by the oxygen present on the surface. Upon fracturing, it is likely that an amount of the flux remained on the aluminum surface despite no reaction with the surface oxides.

In Figure 5.4, Casting K differed from the other aluminum surfaces with an opposing steel insert without flux coating. Instead, the topography was more similar to that observed for Casting I, where a number of smaller pores were observed. Casting K was preheated in the mold for approximately an hour, making the steel insert temperature similar to the mold, 280°C. Upon casting, the higher heat of the insert will allow for slower solidification of the cast aluminum. Higher temperature could also cause better wettability of the steel surface and thus closer contact between the aluminum and the steel. Entrapped air would therefore have extended time to escape through the ventilation system. In addition, the closer proximity between the aluminum melt and the steel will make it more difficult for air to gather. Instead, smaller areas of air are left scattered on the surface. Overall, the amount of gas entrapped in Casting I and K is significantly lower than that observed for Casting E, suggesting that flux coating and higher preheating temperatures should be used.

5.3.4 Bonding Effect in Galvanized Cone-Shaped Steel Inserts

Table 5.6 showed that for castings with cone-shaped steel inserts with a galvanized layer, only one half of Casting S and T remained bound after cutting. However, these two parts showed almost defect-free interfaces as seen in Figure 5.8. The bonding effect of the galvanized cone-shaped steel inserts was investigated through Casting T. Upon further cutting of this casting, the steel insert, excluding the tip, loosened from the cast aluminum. As no melting of the galvanized layer or reaction with the aluminum contact area was observed, only mechanical bonding could have formed. When the liquid aluminum surrounding the steel insert solidifies, some shrinkage will occur which will apply a force around the insert and thus create a mechanical bond. This also implies that the temperature of the steel insert was not high enough, causing the liquid aluminum to solidify rapidly and the galvanized layer to remain intact.

The tip of the cone-shaped insert however, showed areas of local bonding with the cast aluminum as seen in Figure 5.13. Although several porosities and areas where the galvanized layer most likely had not melted were observed in the interface, the temperature is higher at the tip which would allow metallurgical bonding to occur. Figure 5.14 and Table 5.9 show that aluminum was present throughout the interface and that no characteristic structure from the galvanized layer was observed. However, several needle-shaped particles determined to be $Al_{4.5}FeSi$ were detected. Both particle density and porosities in the interface made it difficult to determine lengths of the particles. Despite the galvanized layer melting, rather high concentrations of zinc were detected in the interface. This could be due to the temperature being insufficient in order for zinc to properly diffuse into the aluminum melt. Instead, aluminum will start to nucleate rapidly after casting, causing zinc with a lower melting temperature, to segregate.

A silicon particle was detected on the cast aluminum surface. Several particles showing similar contrast and shape were also observed further along the surface, seen in Figure 5.14. When higher temperatures are used, zinc will diffuse into the aluminum melt and thus little can be detected in the interface. In this case, zinc might have diffused towards the cast aluminum, as noted by the high zinc concentrations in Table 5.9. However, due to rapid cooling of the cast aluminum resulting from low temperature in the steel insert, an undercooling effect could have been created in the interface between the reaction layer and the cast aluminum, causing silicon to nucleate. Regardless of formation of intermetallic phases, the placement of the silicon particles impairs the smooth transition from the reaction layer to the cast aluminum, thus diminishing the metallurgical bond. As these particles are brittle, there is a large chance that a fracture could occur in this interface. Formation of these silicon particles will therefore significantly reduce bonding strength.

5.3.5 Bonding Effect in Galvanized Cone-Shaped Steel Inserts With Flux Coating

From observations made after cutting, no conclusions of the use of flux coating on the cone-shaped steel inserts could be made. As seen in Table 5.6, Casting O displayed good bonding while Casting P broke. Both these castings had similar process parameters, which would indicate that only mechanical bonding had formed. Figure 5.8 shows that large cavities are present in the aluminum-steel interface. Upon casting, liquid aluminum melt will flow past the steel cone and fill the mold. Temperatures are high enough to melt the flux, which then might be brought along the steel surface during the further metal flow. This can result in areas where the flux concentration is not high enough to remove oxides of the aluminum melt and ensure proper wetting.

Further cutting of Casting O did not cause fracturing, as experienced for Casting T without flux coating. However, as seen in Figure 5.11, a large gap between the steel insert and the cast aluminum was observed from the section cut approximately at the middle of the steel cone. In addition, a uniform galvanization layer could still be observed on the steel surface implying no melting. When thickness of the steel insert increases, a higher temperature will be needed in order to form a metallurgical bond. Thicker steel sections will due to the high heat capacity of steel, cause a more rapid solidification of the cast aluminum and thus decrease the probability of melting. At the cone tip, temperature of the steel insert will be less detrimental to solidification rate of aluminum due to less density. In addition, liquid aluminum will continue to flow past this position in the mold, thus allowing the temperature to remain elevated for a longer period. This could explain why a uniform galvanization layer cannot be observed on the steel surface at the cone tip seen in Figure 5.9. The micrographs for the cone-tip and in the middle of the cone, seen in Figure 5.10 and 5.12 confirmed that the galvanized layer only melted at the tip.

Table 5.8 shows that formation of the binary Zn_7Fe formed on the steel surface in the galvanization layer in the sample cut from the middle of the steel cone. This phase was not observed in the characterization made on the blunt steel inserts. Upon casting, temperature of the steel insert might have increased high enough for solid state diffusion of iron atoms at the steel surface to occur, thus forming a thin layer of Zn_7Fe. However, this binary phase could also be a result of greater diffusion of iron atoms during the galvanization process due to locally higher temperatures as the cone thickness decreases. Table 5.8 also shows that a ZnO-layer has formed on the galvanized surface, which will further reduce wettability. Flux coating in this section has not been able to remove both oxides on the galvanized layer and the cast aluminum, thus no proper wetting could be achieved.

The interface at the cone tip, as seen in Figure 5.10, shows that although large porosities are present, an area of local metallurgical bonding is achieved. Compared to casting without flux in Figure 5.14, the transition from reaction layer to cast aluminum is more continuous when flux is used. However, formation of brittle $Al_{4.5}FeSi$ particles was also observed for Casting O. Lengths of the particles varied from 10μm to 112μm, where lengths were observed to increase with distance from the steel insert. This could be due to the temperature increasing with distance from the steel surface. When the galvanized layer melts, iron atoms will be present in the interface. As the liquid aluminum continues to flow, a temperature variance can arise with lower temperatures being detected at the steel surface. Diffusion of iron atoms will therefore be greater in the interface compared to the steel surface, as diffusion is temperature dependent. This could allow growth of the ternary particles. Formation of silicon particles could also be seen in the interface adjacent to ternary particles. Their close proximity could cause an increase in internal stress, due to varying particle shape and orientation, which will significantly decrease the interfacial strength.

5.3.6 Effect of Tempering

Tempering was performed at 540°C, which is above both melting temperature of pure zinc and peritectic temperature of $Zn_{13}Fe$ which formed in the galvanized layer as seen in Figure 5.7. Thus, melting of the galvanized layer would be expected to some extent. Both Casting N and S loosened upon removal from the furnace. If the surface of the galvanized layer started to melt during tempering and no metallurgical bond had formed upon casting, a somewhat molten interface would arise between the cast aluminum and the steel insert, making the mechanical bond loosen. Thus, through removal from the furnace a small force might be applied due to difference in material density, causing complete separation.

Casting S showed no sign of a reaction on either of the contact surfaces, while for Casting N differences in topography could be observed in the contact area around the cone tip. As seen in Figure 5.16, a porous structure formed on the aluminum surface at the cone tip. Variations in color and structure in the corresponding area on the steel insert suggest some melting of the galvanized layer. Remaining surface area of the two metal parts showed no sign of reaction, which most likely is due to insufficient preheating of the steel insert. However, it should be noted that Casting N and S went through a similar preheating process, but Casting N had lower metal pouring temperature. As Casting S had no flux coating, this suggests that the flux coating could be more beneficial than increasing pouring temperature.

Casting O did not loosen upon removal from the furnace, however it was easily fractured when a light human force was applied. Figure 5.17 shows that, as for Casting N, a reaction area was only observed at the cone tip, suggesting mechanical bonding in the thicker insert areas. At the tip, however, a small piece of the galvanized layer remained fastened in the aluminum surface, implying that the fracture occurred at the steel surface. This would indicate higher bonding strength at the cast aluminum/galvanized surface than at the steel surface/galvanized layer. For the section in Casting O shown in Figure 5.12, Zn_7Fe had formed at the steel surface. This phase is deemed to be brittle, thus more susceptible to fracture. Oxides are also detrimental to bonding strength. Fracture thus occurring in the galvanized layer could imply that for the specific area the flux removed the oxides and thus increased wetting and formation of a metallurgical bond. As no reaction between the cast aluminum and steel insert in Casting S was observed as a result of tempering, it is believed that the metallurgical bond in Casting O originated during casting.

5.4 Conclusions

Flushing argon gas in to the mold prior to casting improved bonding between the cast aluminum and the steel insert. However, entrapped air was still observed in the aluminum-steel interface. Therefore, a continuous flushing throughout the casting process is suggested to further improve bonding. Flux coating on the blunt steel inserts caused less air to remain in the interface. A similar effect without flux coating was observed when the insert was preheated to approximately 280°C. No preheating or flux coating caused a large air bubble to remain in the interface.

For castings using blunt steel inserts, only mechanical bonding was obtained. Insufficient heating of the steel inserts by liquid aluminum was found to be the main reason. Therefore, no melting of the galvanized layer occurred despite pouring temperatures of liquid A356 above the peritectic temperature of the binary $Zn_{13}Fe$ phase.

Using cone-shaped steel inserts, a mechanical bond formed in the majority of the castings. Poor metallurgical bonding could be observed at the cone tip both with and without flux coating. When using flux coated inserts areas of local metallurgical bonding were observed. The interface without flux coating showed high pore density. In both interfaces, formation of the brittle $Al_{4.5}FeSi$-phase and silicon particles occurred. Particle density was higher for the insert without flux coating. No melting of the galvanized layer was seen on a section with thicker steel insert.

Tempering proved detrimental to bonding, as all three castings separated. In one of the castings a piece of the galvanized layer remained on the aluminum surface after fracturing, indicating higher bonding strength between the cast aluminum and the galvanized layer compared to the steel surface and the galvanized layer.

Chapter 6

Low Pressure Die Casting of Copper Pipe in Aluminum A356

6.1 Process Parameters

Experimental procedures used for sample preparation and testing of the bimetallic aluminum-copper castings were provided in Chapter 3. Copper pipes used were made of commercially pure copper. Process parameters used under the low pressure die casting of aluminum-copper castings are presented in Table 6.1. Heat treatment was performed using the T6 process as described in Chapter 3.

Table 6.1: Process parameters for aluminum-copper low pressure die casting. Data was obtained from Benteler Automotive Farsund AS.

Casting	Pipe material	Pipe temperature [°C]	Flux coating	Metal pouring temperature [°C] (manually measured)	Heat treatment (T6)
37	Cu	>200	X	714	X
38	Cu	>200	X	714	-
39	Cu	>200	X	714	-
40	Cu	>200	X	712	-
42	Cu	>200	-	712	-
43	Cu	>200	-	712	-
44	Cu	>200	-	712	-
45	Cu	>200	-	712	-

6.2 Results

Parameters for the castings investigated were provided in Table 6.1. As some castings had similar process parameters and showed similar results, they will not be presented in this chapter. Instead, results from Casting 40, 42 and 45 can be found in Appendix A.

Characterization of the bimetallic aluminum-copper castings will be presented based on surface treatment. Other variations in process parameters will be specified in the given subsection. Precise hardness measurements across the aluminum-copper interface are provided in tables in Appendix B.

6.2.1 Effect of Flux Coating

For Casting 37, 38 and 39, the copper pipe was heated to approximately 200°C and flux coated prior to casting. Characterization of the copper-aluminum interface will be presented for each casting separately, while hardness measurements across the interface will be compared at the end of this subsection.

Casting 37 had a metal pouring temperature 714°C and was heat treated using the T6 process subsequent to casting. A macroscopic investigation of the casting was performed after grinding and polishing. An image is given in Figure 6.1.

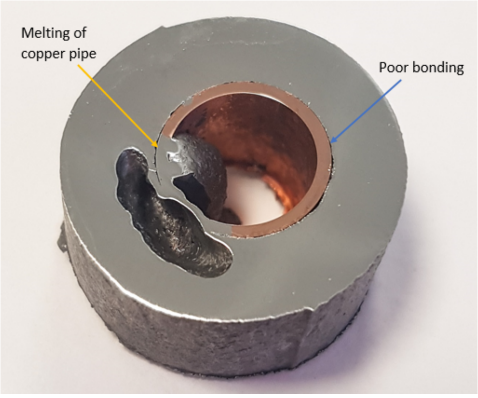

Figure 6.1: Image of Casting 37 after grinding and polishing. A large part of the copper pipe melted, as indicated by the yellow arrow. On the opposite side of the pipe, a blue arrow shows areas of poor bonding.

Figure 6.1 shows that a large section of the copper pipe has melted, leaving a significant cavity in the cast aluminum alloy. This is indicated by the yellow arrow. The remaining interface in the casting displays poor bonding as well as areas where no bonding appears to have occurred. The blue arrow indicates one such area.

In an area close to the melting cavity of the copper pipe, a reaction area was observed using an optical microscope. This is shown in Figure 6.2.

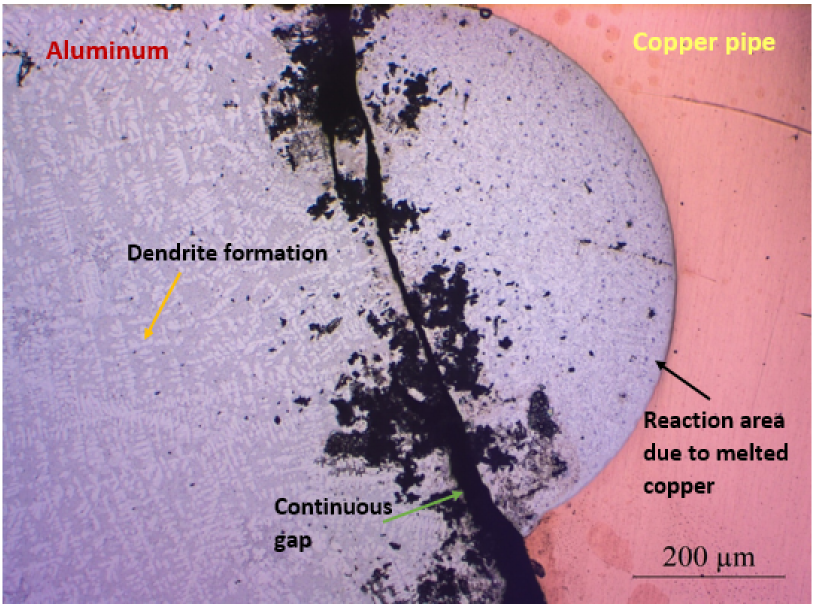

Figure 6.2: Optical micrograph of the aluminum-copper interface in Casting 37. Formation of a dendritic structure can be observed in the cast aluminum, as indicated by a yellow arrow. The black arrow shows a droplet-formed reaction area on the copper pipe surface. A continuous gap between the reaction area and cast aluminum is noted by the green arrow.

Figure 6.2 shows that a reaction area has formed on the copper surface in the given section of Casting 37. Both color and shape of the reaction area, indicate that the formation is due to local melting of the copper pipe. No specific structure or particle formation can be observed in the reaction area. However, a fine columnar dendritic structure has formed in the cast aluminum, as seen by the yellow arrow. This differs from the usually observed eutectic Al-Si structure. A continuous gap is observed between the cast aluminum and the reaction area, but as a reaction area formed it would imply that the crack has occurred upon solidification. A section further from the melting cavity of the copper pipe was also investigated using optical microscopy. This can be seen in the optical micrograph in Figure 6.3.

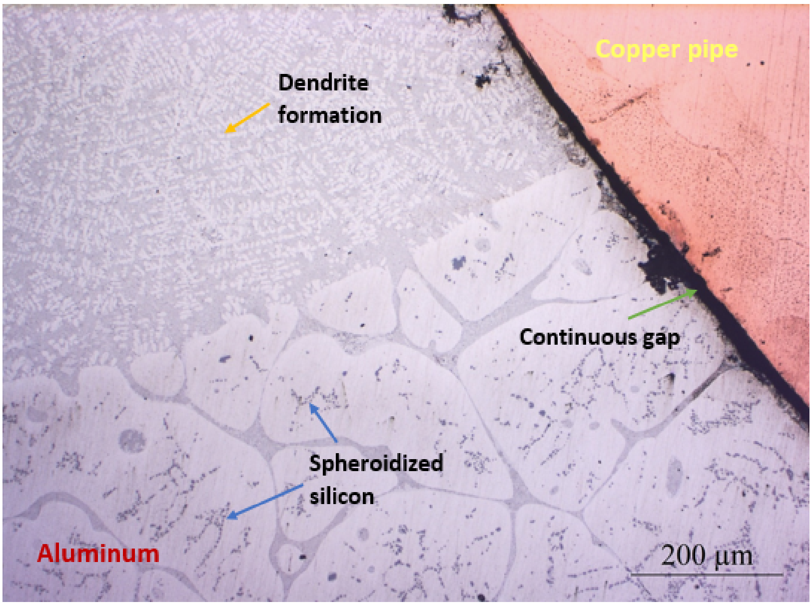

Figure 6.3: Optical micrograph of a section of the aluminum-copper interface in Casting 37. Formation of a dendritic structure can be observed in an area of the cast aluminum, as indicated by a yellow arrow. Another area of the cast aluminum shows spheroidized silicon in the eutectic Al-Si structure, indicated by the blue arrows. A green arrow shows a continuous gap separating the copper pipe and the cast aluminum.

The optical micrograph in Figure 6.3 shows that no reaction area formed in this section. Instead, a continuous gap, shown by the green arrow, separates the cast aluminum and the copper pipe. In the cast aluminum, two separate structures can be observed. A fine dendritic structure, similar to that found in Figure 6.2, can be observed in the upper part of the micrograph, as shown by the yellow arrow. However, a transition from this structure to the characteristic Al-Si eutectic structure occurs in this section of the casting. In the eutectic structure, silicon has spheroidized as a result of the heat treatment. Also, the grains observed are much larger than in a non-heat treated aluminum casting, which would imply remelting of grain boundaries and grain growth due to the heat treatment. This is shown by the blue arrows.

As a continuous gap was observed in both sections investigated using optical microscopy, a third section where potential bonding had occurred was further considered using SEM. A micrograph of this section is shown in Figure 6.4. Red circles indicate areas investigated using EDS. Results of the analysis are presented in Table 6.2.

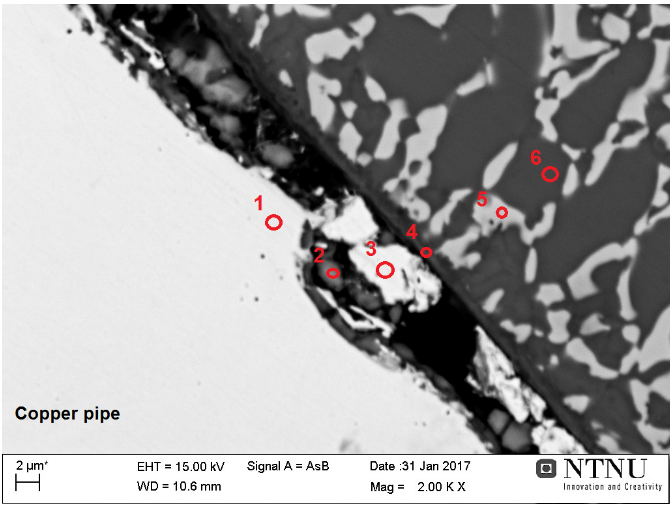

Figure 6.4: Micrograph of the aluminum-copper interface in Casting 37. Red circled areas were analyzed using EDS. Results from the analysis are presented in Table 6.2.

Table 6.2: Compositions and possible phases, analyzed using EDS, across the aluminum-copper interface in Casting 37 showed by red circled areas in Figure 6.4.

Area	Composition [at%]							Possible phase
	Al	Cu	Si	Mg	K	F	O	
1	-	100	-	-	-	-	-	Cu
2	15.84	6.35	-	-	24.79	40.17	12.85	Flux residue
3	-	100	-	-	-	-	-	Cu
4	56.03	8.25	3.64	28.67	3.41	-	-	Al-Cu-Mg or Al-Cu-Si-Mg
5	61.41	21.45	17.14	-	-	-	-	Al_2Cu + (Al) + Si
6	97.97	2.03	-	-	-	-	-	(Al)

Irregularities of the copper pipe surface seen in Figure 6.4, indicates that some melting has occurred. The compositions of Area 1 and 3 provided in Table 6.2 show detection of pure copper. In Area 2, high concentrations of potassium and fluoride imply flux residue. Oxygen is also detected in this area, suggesting that the flux has not functioned optimally.

A film appears to have formed on the cast aluminum surface, as seen by the slight contrast difference in Figure 6.4. Composition found for Area 4 suggests formation of a ternary Al-Cu-Mg or a quaternary Al-Cu-Si-Mg phase. The small concentration of potassium detected is most likely due to nearby flux residue. The brighter phase observed in the cast aluminum would, based on the composition found in Area 5, suggest a ternary Al-Cu-Si phase. However, as no such phase has been distinguished, the area is believed to be a combination of the binary Al_2Cu, (Al) and Si.

Casting 38 had a metal pouring temperature of 714°C, as seen in Table 6.1. An image of the casting was taken after grinding and polishing. This is shown in Figure 6.5.

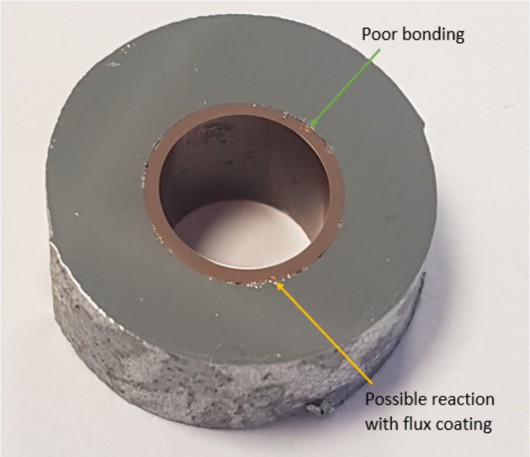

Figure 6.5: Image of Casting 38 after grinding and polishing. Green arrow shows an area with poor bonding, whereas the yellow arrow indicates an area where a possible reaction with the flux coating has occurred.

An area with poor bonding between the copper pipe and the cast aluminum alloy is noted by the green arrow in Figure 6.5. The yellow arrow shows an area with characteristics similar to that of porosity or small amounts of spatter. This could imply a possible reaction between the flux coating and the cast aluminum. To determine if any reaction had occurred, optical microscopy was used. An optical micrograph of Casting 38 is shown in Figure 6.6.

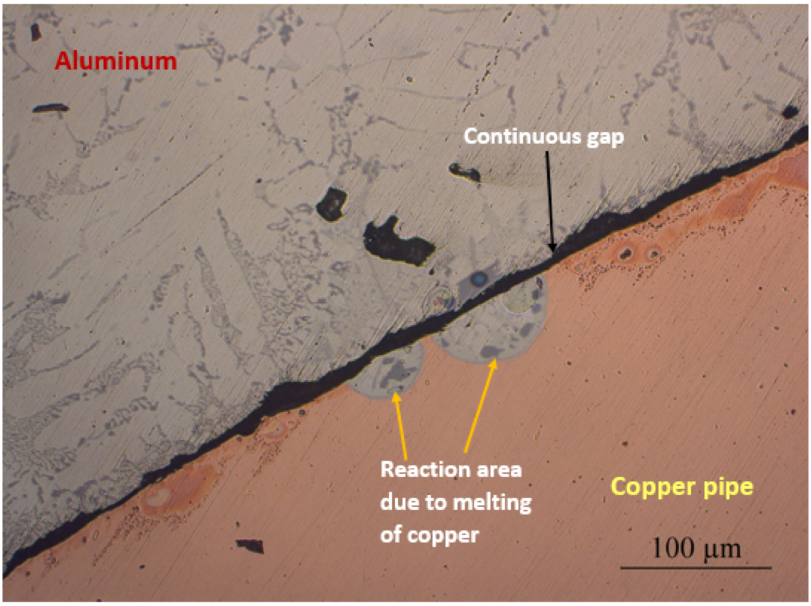

Figure 6.6: Optical micrograph of the aluminum-copper interface in Casting 38. Yellow arrows show two reaction areas where the copper pipe surface has melted. A continuous gap between the copper pipe and aluminum melt is indicated by a black arrow.

From the black arrow in Figure 6.6, a continuous gap between the copper pipe and the cast aluminum alloy can be seen. This indicates that there has been no bonding between the two. However, as shown by the yellow arrows, two reaction areas were observed. As these are found in the copper pipe, it is most likely due to local melting of the pipe surface. The gap between the reaction area and the cast aluminum would therefore have occurred after solidification of the liquid droplet. Both reaction areas have similar shape and structure, with formation of various intermetallic phases.

EDS was used to determine the composition of the reaction area observed in the optical microscope. Figure 6.7 shows the SEM structure of this area. Based on contrast, it is believed that several phases with different compositions have formed. Analysis of the areas marked with red circles in Figure 6.7 are shown in Table 6.3.

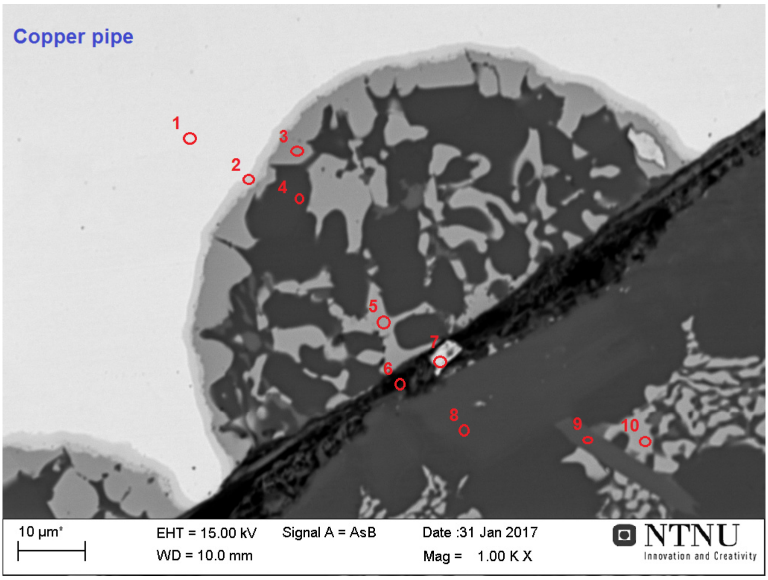

Figure 6.7: Micrograph of the aluminum-copper interface in Casting 38. Red circles indicate areas investigated by EDS. Results from the EDS analysis are presented in Table 6.3.

Table 6.3: Compositions and possible phases, analyzed using EDS, across the aluminum-copper interface in Casting 38 showed by red circled areas in Figure 6.7.

Area	Composition [at%]						Possible phase
	Al	Cu	Si	Mg	K	F	
1	-	100	-	-	-	-	Cu
2	37.17	62.83	-	-	-	-	Al_2Cu_3
3	69.18	30.82	-	-	-	-	Al_2Cu
4	1.14	0.82	98.04	-	-	-	Si
5	70.17	29.83	-	-	-	-	Al_2Cu
6	36.39	16.48	3.71	10.53	6.90	25.98	Flux residue + MgF_2
7	50.14	18.86	-	10.06	6.77	14.17	Flux residue
8	2.30	-	97.70	-	-	-	Si
9	57.58	0.82	24.82	16.78	-	-	Al-Cu-Mg-Si phase
10	70.34	28.30	1.37	-	-	-	Al_2Cu

Based on the EDS analysis presented in Table 6.3, several binary aluminum-copper phases can be determined. Area 2 lies within a film that appears to have formed on the exterior part of the droplet. Based on composition, this is a copper-rich phase, most likely Al_2Cu_3. Both Area 3 and 5 have similar compositions, with an aluminum-copper ratio of 2.3, implying formation of Al_2Cu. The same phase is also found in the cast aluminum alloy, specifically in Area 10, indicating copper diffusion into the aluminum melt and thus formation of Al-Al_2Cu eutectic. Area 6 and 7, which are measured in the appearing gap, show detection of magnesium, potassium and fluoride indicating flux residue. In Area 6 the magnesium and fluoride concentration could suggest formation of MgF_2 among the residue. Magnesium is also found in Area 9, along with high amounts of silicon and aluminum. Based on contrast from the micrograph in Figure 6.7, it appears as if this area is part of a particle forming adjacent to the Al_2Cu phase in Area 10. The composition would suggest formation of a quaternary Al-Cu-Mg-Si phase. However, it does not coincide with the known $Al_5Cu_2Mg_8Si_6$-phase.

From the micrograph in Figure 6.7, it can be seen that the contrast is somewhat brighter around Area 4 and 8. From the EDS analysis in Table 6.3, these two areas appear to be silicon particles. If the areas in the micrograph are compared to that observed in Figure 6.6, dark particles are seen in the same area for the optical micrograph. From the latter figure, it is also evident that silicon particles have formed in both reaction areas.

Casting 39 had identical process parameters compared to Casting 38. Figure 6.8 shows an image of the casting after grinding and polishing. The yellow arrows show areas of poor bonding with several gaps between the copper pipe and the cast aluminum. As indicated by the black arrow, a reaction has possibly occurred between the flux coating and the aluminum melt.

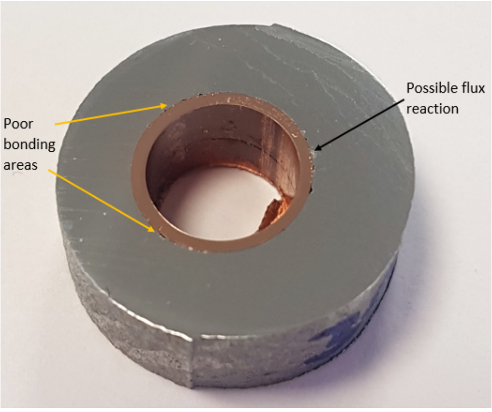

Figure 6.8: Image of Casting 39 after grinding and polishing. Yellow arrows show areas with poor bonding and multiple cavities, while the black arrow indicates a possible reaction area between the flux coating and the aluminum melt.

To determine if a bonding layer had formed, optical microscopy was used. An optical micrograph of the interface in Casting 39 is shown in Figure 6.9.

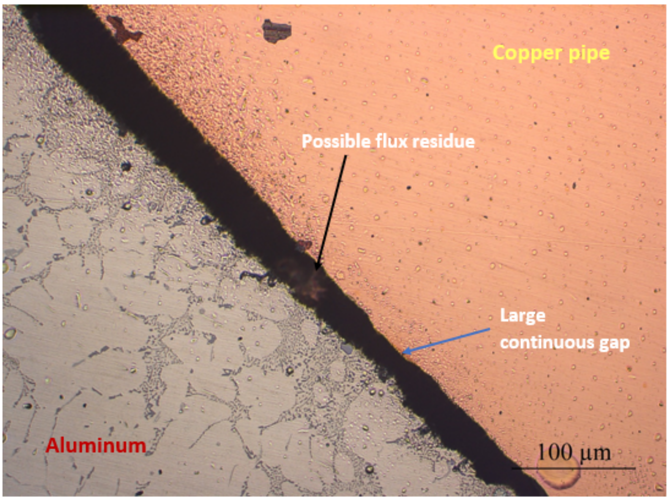

Figure 6.9: Optical micrograph of the aluminum-copper interface in Casting 39. The blue arrow shows a large continuous gap between the copper pipe and the cast aluminum, whereas potential flux residue in the gap is noted by the black arrow.

From Figure 6.9, a large continuous gap is observed between the copper pipe and the aluminum melt, thus indicating that no bonding layer was formed. This is shown by a blue arrow. However, as can be seen by the black arrow, an area in the gap is brighter than the rest, implying presence of a material reflected by light from the microscope. This could possibly be flux residue from an incomplete reaction with the aluminum melt. An EDS line scan was performed to further investigate the interface. The line scan is shown in Figure 6.10.

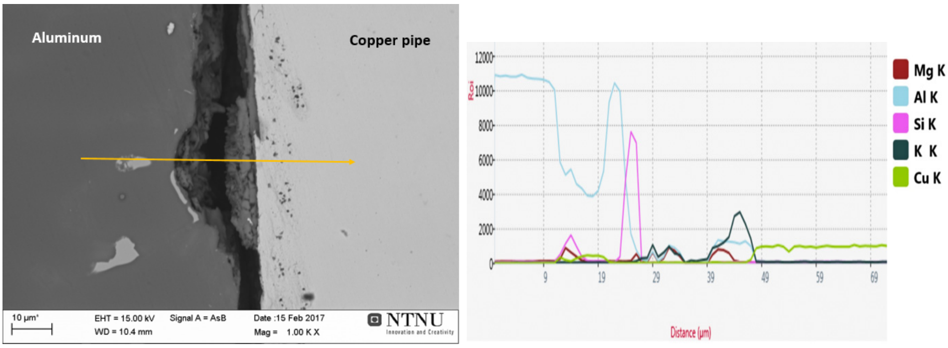

Figure 6.10: EDS line scan across the aluminum-copper interface in Casting 39. The scan follows the yellow line. X-axis gives distance from starting point, whereas y-axis shows intensity of element detected. Elements found are designated with different colours given in the graph.

As shown in Figure 6.10, there is a dark grey layer on the surface of the copper pipe. The dark blue-green line, representing potassium, has a peak in this area. This implies the presence of flux residue in the interface. Relatively high concentrations of potassium are also detected on the edge of the aluminum melt, alongside magnesium represented by a red line. A gap has formed between these two areas of flux residue. However, the light green line representing copper, shows that a small concentration of copper is detected in the cast aluminum alloy. This could suggest that the gap formed upon solidification, as copper has diffused into the aluminum melt.

A section without the appearing gap was investigated using SEM. An EDS analysis was performed on various areas of the interface in this section. These are given by red circles as shown in Figure 6.11. Table 6.4 presents EDS results for each area.

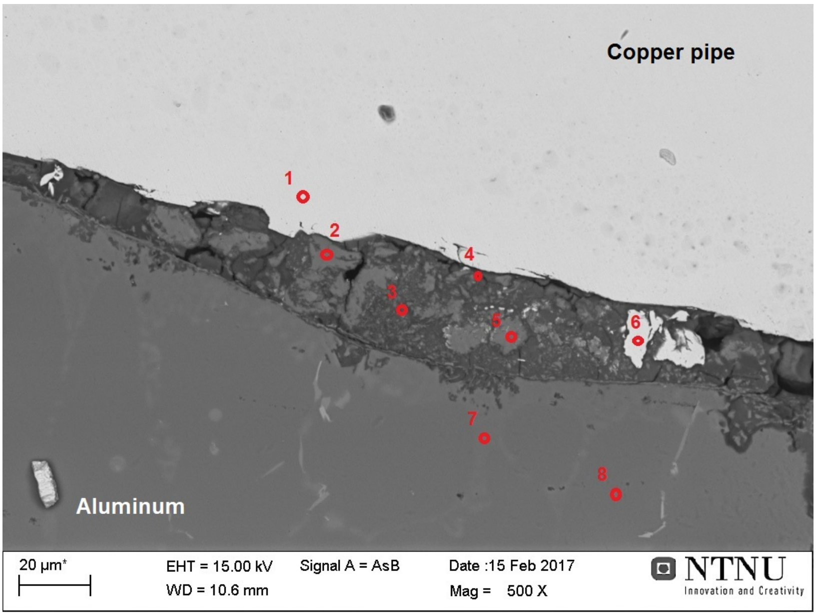

Figure 6.11: Micrograph of the aluminum-copper interface in Casting 39. Red circles indicate areas investigated by EDS. Results from the EDS analysis are presented in Table 6.4.

Table 6.4: Compositions and possible phases, analyzed using EDS, across the aluminum-copper interface in Casting 39 showed by red circled areas in Figure 6.11.

Area	Composition [at%]							Possible phase
	Al	Cu	Si	Mg	K	F	O	
1	-	100	-	-	-	-	-	Cu
2	97.26	-	2.74	-	-	-	-	(Al)
3	27.44	0.70	2.98	2.69	3.70	20.01	42.49	Flux residue + $KMgF_3$
4	17.09	7.18	-	-	11.61	9.22	54.91	Flux residue
5	64.29	1.37	22.15	-	-	-	12.20	(Al) + Si
6	-	100	-	-	-	-	-	Cu
7	68.08	-	31.92	-	-	-	-	Eutectic Al-Si
8	100	-	-	-	-	-	-	(Al)

As shown in Figure 6.11, the surface of the copper pipe has a higher contrast and displays irregularities, indicating a partial melting during casting. As seen in Area 2 in Table 6.4, high concentrations of aluminum are detected adjacent to the copper pipe surface. The darker layer between the copper and the cast aluminum, is suggested to be flux residue based on the detection of potassium and fluoride in Area 3 and 4. High concentrations of oxygen detected in these two areas show that the flux has not functioned optimally. In addition, the composition in Area 3 coincides with the possible formation of $KMgF_3$ among the flux residue. Copper content is either relatively low or not detectable in the interface, showing no diffusion of copper into the cast aluminum despite possible melting of the pipe surface. In Area 6 however, 100 at% copper was detected. Figure 6.11 shows that this area is part of a bright particle located in the interface, indicating incomplete melting of copper.

Micro-hardness tests were performed over the interface for each of the flux coated castings. Hardness were measured in Vickers. Figure 6.12 shows the interface in which hardness was measured as well as the results found for Casting 37, 38 and 39.

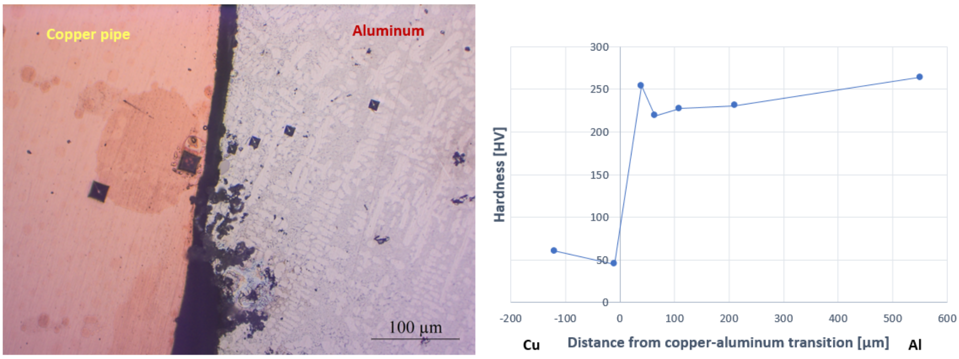

(a) Vickers hardness measured across the aluminum-copper interface in Casting 37. Copper-aluminum transition is set as transition from copper surface to cast aluminum.

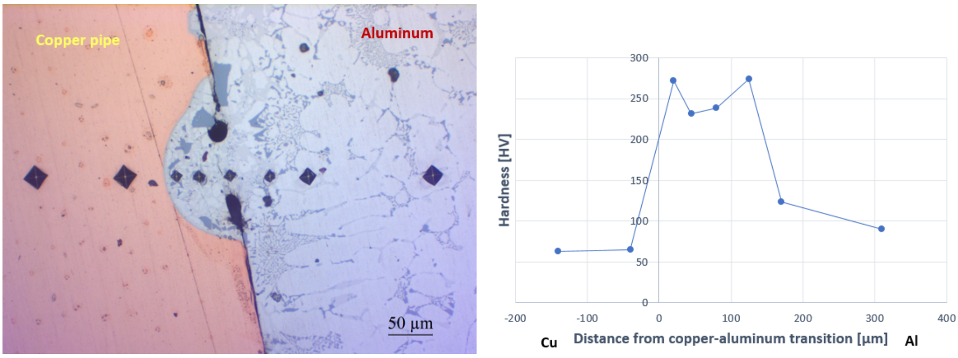

(b) Vickers hardness measured across the aluminum-copper interface in Casting 38. Copper-aluminum transition is set as transition from copper pipe to reaction area.

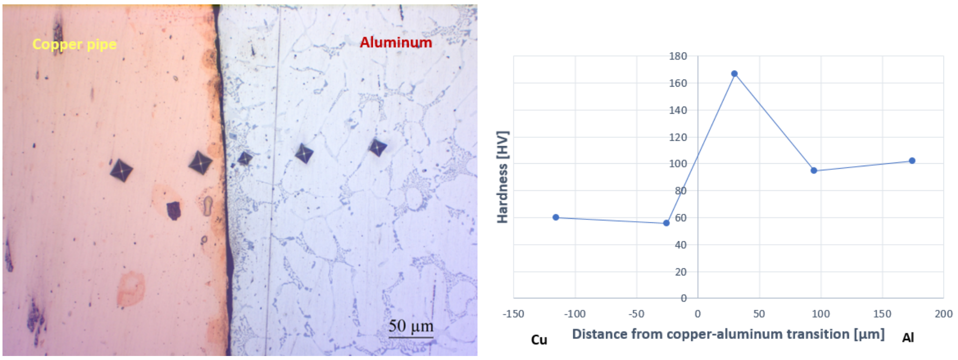

(c) Vickers hardness measured across the aluminum-copper interface in Casting 39. Copper-aluminum transition is set as transition from copper pipe to cast aluminum.

Figure 6.12: Vickers hardness measured across the aluminum-copper interface in Casting 37, 38 and 39.

As seen in Figure 6.12a, a gap had formed between the copper pipe and the cast aluminum. Therefore, no reaction area could be observed. However, it is worth noting that the hardness in the surface layer is higher than in the bulk of the cast aluminum. Compared to the results found for Casting 38 and 39, the hardness in the cast aluminum has increased by approximately a factor of two, implying that some copper has dissolved into the aluminum during remelting of the pipe upon heat treatment. No change was observed for the copper pipe, which displayed similar hardness in all three castings. Figure 6.12b shows that hardness measured in the reaction area of Casting 38 is over twice that of both the copper pipe and the adjacent cast aluminum. The reaction area also appears to stretch beyond the observed crack in Figure 6.12b, as the measured hardness of the first four values after the copper-aluminum transition are similar. For Casting 39, in Figure 6.12c, no reaction area was observed. However, the hardness measured approximately on the surface of the cast aluminum is significantly higher compared to those further in the melt. Based on the optical micrograph shown in Figure 6.12c, a higher concentration of eutectic silicon can be seen on the cast aluminum surface which could explain the increase in hardness.

6.2.2 Effect of No Surface Treatment

Casting 43 and 44 had identical process parameters, as shown in Table 6.1. The copper pipes were preheated to approximately 200°C and had no surface treatment except thorough cleaning in ethanol. A metal pouring temperature of 712°C was used in the casting process. Characterization of the aluminum-copper interface in the two castings will be presented separately in this subsection, followed by a comparison of hardness measurements.

An image of Casting 43 was taken after grinding and polishing to establish possible defects in the aluminum-copper interface. This is shown in Figure 6.13.

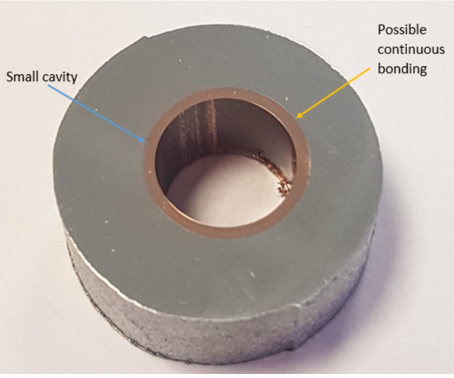

Figure 6.13: Image of Casting 43 after grinding and polishing. A small cavity was observed in the interface between the cast aluminum alloy and the copper pipe, as noted by the blue arrow. Potentially continuous bonding was seen for the remaining interface indicated by the yellow arrow.

From Figure 6.13, only a small cavity could be observed in the interface between the copper pipe and the cast aluminum. This is shown by the blue arrows. Throughout the remaining interface, what appeared to be continuous bonding was seen, as indicated by the yellow arrow. This bonding layer was further investigated using an optical microscope. Figure 6.14 shows an optical micrograph of the interface between the copper pipe and the cast aluminum.

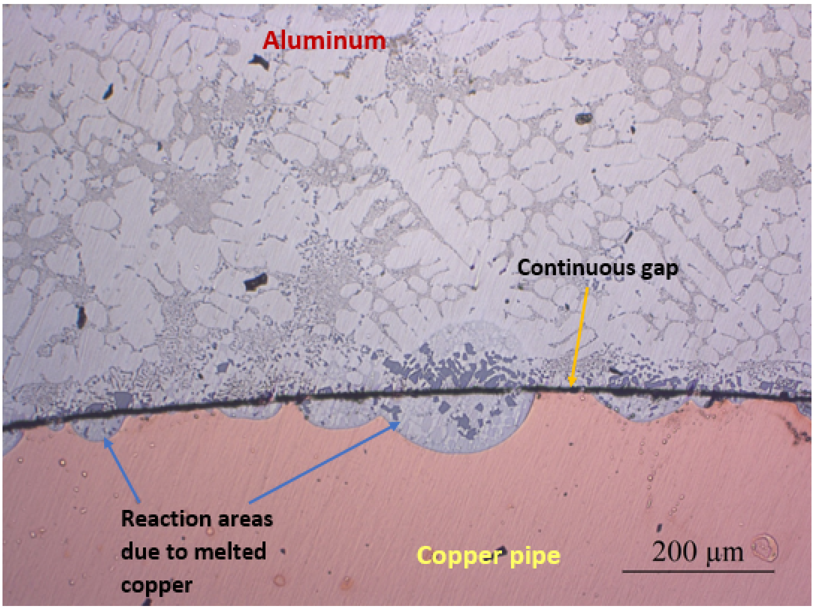

Figure 6.14: Optical micrograph of the aluminum-copper interface in Casting 43. A continuous gap is observed between the copper pipe and the cast aluminum, indicated by a yellow arrow. The blue arrows show several reaction areas formed by local melting of the copper pipe.

A continuous narrow gap can be seen between the copper pipe and the cast aluminum in Figure 6.14, shown by the yellow arrow. However, several reaction areas are observed on the copper surface, some of which are indicated by blue arrows. Shape and size of the reaction areas vary, but the structure appears similar. The color difference in the reaction area and the copper pipe shows that these areas have formed due to local melting of the copper pipe. This would imply that the gap has formed upon solidification.

SEM and EDS were used to determine the composition of different phases in one of the reaction areas. Figure 6.15 shows red circled areas which were investigated using EDS. Results of the analysis are presented in Table 6.5.

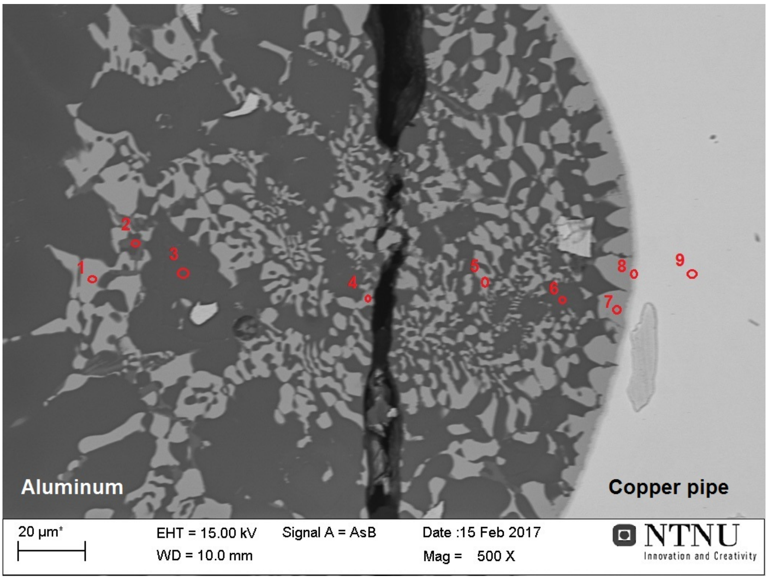

Figure 6.15: Micrograph of reaction area in Casting 43. Red circles indicate areas analyzed using EDS. Results from the analysis are presented in Table 6.5.

Table 6.5: Compositions and possible phases, analyzed using EDS, in a reaction area in Casting 43 showed by red circled areas in Figure 6.15.

Area	Composition [at%]					Possible phase
	Al	Cu	Si	Mg	O	
1	69.28	30.72	-	-	-	Al_2Cu
2	89.68	1.34	4.61	4.37	-	Al-Cu-Si-Mg phase
3	1.58	-	98.42	-	-	Si
4	74.80	13.68	1.65	-	9.87	Eutectic (Al)-Al_2Cu
5	94.08	5.92	-	-	-	Eutectic (Al)-Al_2Cu
6	31.69	1.82	66.50	-	-	(Al) + Si
7	68.59	31.41	-	-	-	Al_2Cu
8	-	100	-	-	-	Cu
9	-	100	-	-	-	Cu

From Figure 6.15 there are small areas where bonding is continuous, suggesting that cracking has occurred upon solidification. A eutectic structure is observed throughout the interface. Ratio between aluminum and copper in Area 1 indicates that this is the eutectic (Al)+ Al_2Cu. This can also be seen in Area 4 and 5, although the compositions here show higher concentration of aluminum, possibly as a result of the finer eutectic structure. In Area 4, a noteworthy oxygen content is detected, most likely due to closeness to the gap. Among the eutectic Al_2Cu, areas with contrast differing from both the aluminum and the

Al_2Cu can be seen, as shown in Figure 6.15. Area 2 marks one of these areas, and as seen in Table 6.5, magnesium is detected. The composition in this area would suggest formation of a quaternary Al-Cu-Si-Mg phase, although it does not coincide with the known $Al_5Cu_2Mg_8Si_6$-phase.

Although not very apparent by contrast, the high concentration of silicon found in Area 3 suggests formation of a silicon particle. By comparing the micrograph in Figure 6.15 to the optical micrograph in Figure 6.14, several dark particles can be observed in the interface in both the reaction areas and in the cast aluminum adjacent to the gap. These were previously recognized as silicon particles, and would therefore coincide with the composition found in Area 3.

On the edge of the reaction area, the contrast differs from both the Al_2Cu-phase in Area 7 and pure copper in Area 9. Even though this can be seen in Figure 6.15, Table 6.5 shows 100 at% in Area 8. This might be due to the section being too thin for EDS to detect at this magnification. The outer part of the reaction area was therefore zoomed in and further investigated. The resulting micrograph is shown in Figure 6.16 with EDS analysis results listed in Table 6.6.

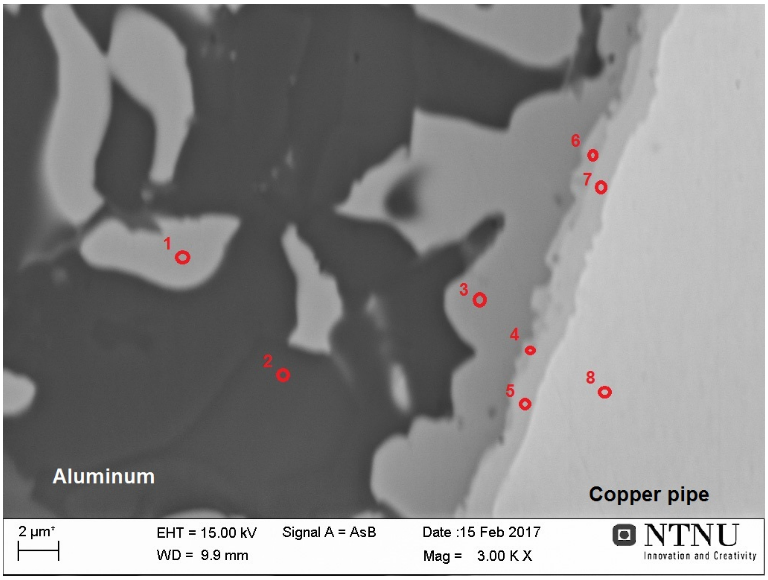

Figure 6.16: Micrograph of the reaction area-copper pipe interface in Casting 43. Red circles indicate areas analyzed using EDS. Results of the analysis are presented in Table 6.6.

Table 6.6: Compositions and possible phases, analyzed using EDS, across the reaction area-copper pipe interface in Casting 43 showed by red circled areas in Figure 6.16.

Area	Composition [at%]			Possible phase
	Al	Cu	Si	
1	70.23	29.77	-	Al_2Cu
2	2.26	0.83	96.91	Si
3	69.07	30.93	-	Al_2Cu
4	24.04	75.96	-	Al_4Cu_9
5	-	100	-	Cu
6	4.70	95.30	-	(Al) + Cu
7	-	100	-	Cu
8	-	100	-	Cu

From Table 6.6 it can be seen that Area 1 and 3 have similar composition. Both have an aluminum-copper ratio of approximately 2.3, indicating formation of Al_2Cu which was also seen in Figure 6.15. The high concentration of silicon in Area 2, alongside the weak outlines of a particle that can be observed around this area in Figure 6.16, suggests formation of a silicon particle. This was, as mentioned, also observed in both Figure 6.14 and Figure 6.15.

Based on contrast, there appears to be two thin intermetallic layers formed between the Al_2Cu-phase and the copper pipe, as seen in Figure 6.16. EDS results show that, despite the difference in contrast, both Area 5 and 7 which belong to the layer closest to the copper pipe have 100 at% Cu. This could be due to uncertainty in the analysis. The remaining layer has varying compositions, with both areas being copper-rich to different extents. In Area 6 the copper content is too high to coincide with any binary phase, and it is therefore suggested to be an area where aluminum has diffused into the copper. Area 4 has a copper content higher than that identified in the equilibrium phases stable at 500°C. However, as the surrounding matrix shows high concentrations of copper, the phase is most likely the copper-rich Al_4Cu_9-phase.

Casting 44 was also photographed after grinding and polishing. This is shown in Figure 6.17.

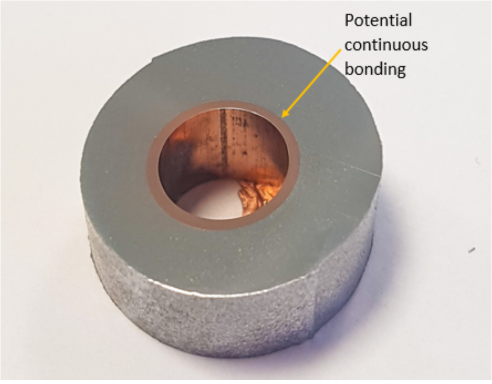

Figure 6.17: Image of Casting 44 after grinding and polishing. No defects were observed in the aluminum-copper interface. Instead, potentially continuous bonding had formed, as indicated by the yellow arrow.

From Figure 6.17 no defects in the interface between the copper pipe and the aluminum cast are visible. Instead, a continuous bonding layer is believed to have formed throughout the interface, as shown by the yellow arrow. An optical microscope was used to determine if any reaction zone had formed in the interface. The resulting micrograph is shown in Figure 6.14.

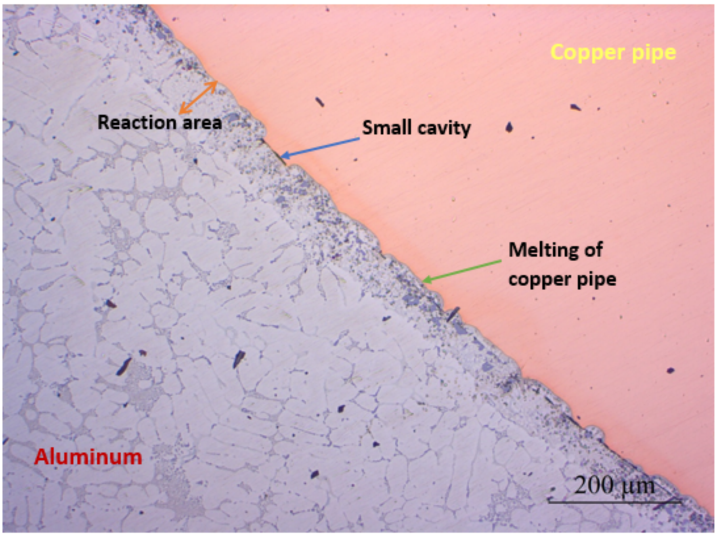

Figure 6.18: Optical micrograph of the aluminum-copper interface in Casting 44. A reaction layer has formed due to melting of the copper pipe. This is indicated by a green arrow, whereas layer thickness is noted by the orange arrow. The blue arrow shows a small interfacial cavity.

Continuous metallurgical bonding can be seen almost throughout the interface in Figure 6.18. Some areas however, show small cavities or cracks, as the one indicated by a blue arrow. Due to irregularities of the surface on the copper pipe, it is believed that local melting of the pipe surface has occurred. This is shown by the green arrow. Comparing structures throughout the cast aluminum alloy, a change from the characteristic Al-Si eutectic structure in the bulk to an interfacial layer with particles, suggests formation of a reaction layer. This is marked by an orange arrow, and appears to have somewhat uniform thickness throughout the optical micrograph.

A closer look at the reaction layer was performed using SEM, as shown in the micrograph in Figure 6.19. The reaction layer has a thickness of approximately 70μm. Some black areas indicate small cavities present close to the copper pipe. Compositions of the red circled areas were analyzed using EDS. Results from the analysis are presented in the following Table 6.7.

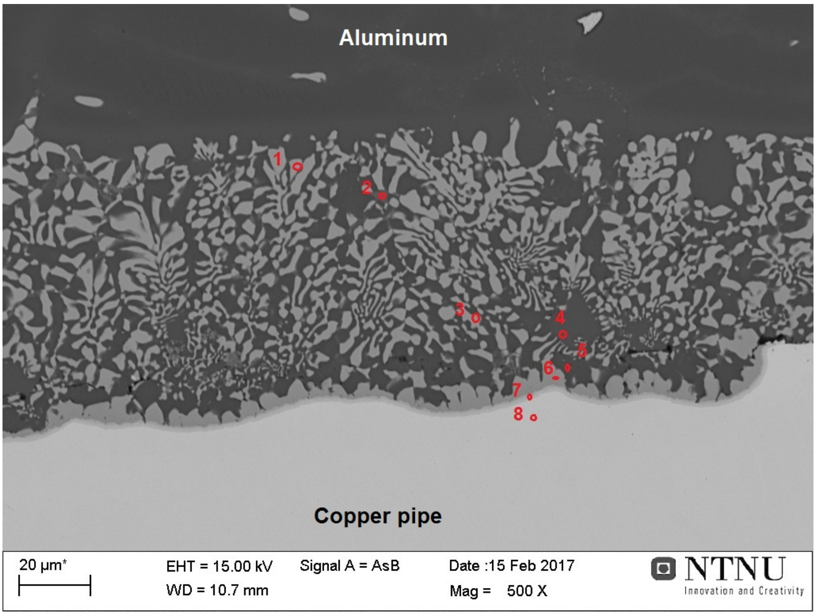

Figure 6.19: Micrograph of the aluminum-copper interface in Casting 44. Red circled areas were analyzed using EDS. Results from the analysis are presented in Table 6.7.

Table 6.7: Compositions and possible phases, analyzed using EDS, across the aluminum-copper interface in Casting 44 showed by red circled areas in Figure 6.19.

Area	Composition [at%]				Possible phase
	Al	Cu	Si	Mg	
1	85.82	4.13	5.07	4.98	Al-Cu-Si-Mg phase
2	53.31	2.10	25.60	18.99	Al-Cu-Si-Mg phase
3	71.58	28.42	-	-	Al_2Cu
4	1.74	0.71	97.55	-	Si
5	98.27	1.73	-	-	(Al) + Cu
6	69.55	30.45	-	-	Al_2Cu
7	69.49	30.51	-	-	Al_2Cu
8	-	100	-	-	Cu

As seen in Table 6.7, magnesium was detected in both Area 1 and 2. The latter has a much higher content of both magnesium and silicon which could explain the darker contrast in this area. Both areas are believed to be quaternary Al-Cu-Si-Mg phases, with varying compositions. As they differ from the known $Al_5Cu_2Mg_8Si_6$-phase, it is difficult to determine the the type of the phase. Compositions measured in Area 3, 6 and 7 are fairly similar, giving an average aluminum copper ratio of 2.36. This coincides with the binary aluminum-copper phase, Al_2Cu. This would imply that the structure observed in the reaction area is eutectic (Al)+Al_2Cu.

No significant difference in contrast can be observed around Area 4. However, the high concentration of silicon seen in Table 6.7, suggests formation of a silicon particle. In Area 5 no silicon is detected, implying that silicon particles are not found in all areas between the eutectic Al_2Cu. Based on contrast, a film with different composition than Area 6 and 7 appears to have formed on the copper surface. A micrograph zooming in on this area is shown in Figure 6.20. Red circles mark areas analyzed using EDS. The results are presented in Table 6.8.

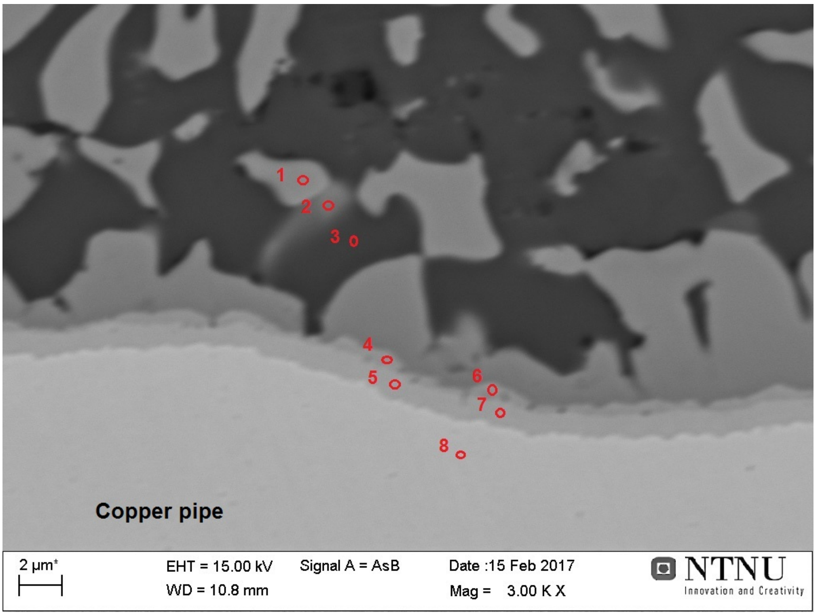

Figure 6.20: Micrograph of zoomed in section from Figure 6.19 in Casting 44. Red circles indicate sections analyzed using EDS. Results of the analysis are presented in Table 6.8.

Table 6.8: Compositions and possible phases, analyzed using EDS, across the reaction area-copper pipe interface in Casting 44 showed by red circled areas in Figure 6.20.

Area	Composition [at%]				Possible phase
	Al	Cu	Si	O	
1	73.71	26.29	-	-	Al_2Cu
2	74.92	25.08	-	-	Al_2Cu
3	92.36	7.64	-	-	(Al) + Cu
4	54.43	45.57	-	-	AlCu
5	37.40	62.60	-	-	Al_2Cu_3
6	64.83	31.41	1.21	2.55	Al_2Cu
7	40.45	59.55	-	-	Al_2Cu_3
8	-	100	-	-	Cu

Table 6.8 shows that Area 1 and 2 have similar compositions despite some contrast difference. For these two areas, the average aluminum-copper ratio is 2.9, making them most likely to be Al_2Cu. A high aluminum concentration in Area 3 suggests that the aluminum phase has a high copper content. The film observed on the surface of the copper pipe in Figure 6.19 appears to be subdivided into two thinner films based on the contrast observed in Figure 6.20. Area 5 and 7 in the layer adjacent to the copper pipe have an average

copper-aluminum ratio of 1.57, coinciding with the copper-rich phase Al_2Cu_3. The second layer however, shows different compositions, as seen in Area 4 and 6. In Area 4, the aluminum and copper concentration is relatively similar indicating formation of AlCu. Area 6 shows detection of oxygen and the aluminum-copper composition is more similar to the adjacent Al_2Cu phase.

Hardness measured for Casting 43 and 44, which had no surface treatment, is presented in Figure 6.21.

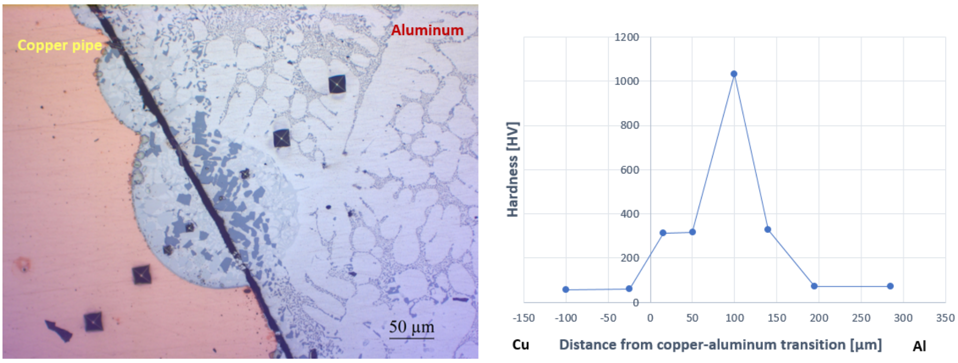

(a) Vickers hardness measured across the aluminum-copper interface in Casting 43. Copper-aluminum transition is set as transition from copper pipe to reaction area.

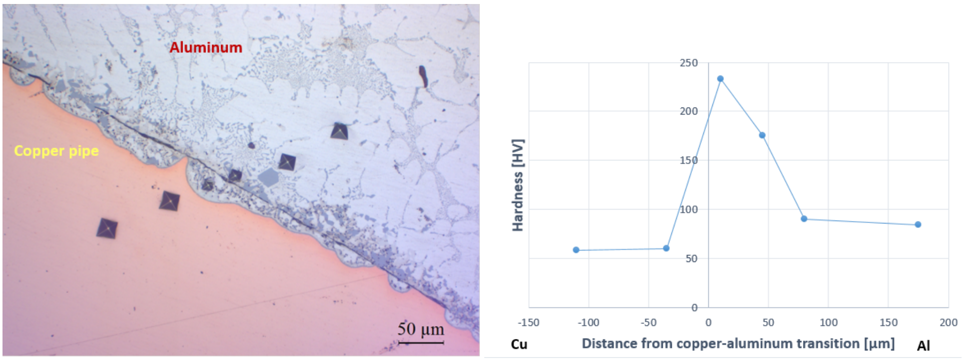

(b) Vickers hardness measured across the aluminum-copper interface in Casting 44. Copper-aluminum transition is set as transition from copper pipe to reaction area.

Figure 6.21: Vickers hardness measured across the aluminum-copper interface in Casting 43 and 44.

Figure 6.21 shows that the hardness in a reaction area is significantly higher than both the copper pipe and the cast aluminum. This is observed both for Casting 43 and 44. In Casting 43, the reaction area appears to have similar hardness throughout, as can be seen from the three measurements showing almost identical values. However, one measurement varies drastically, and showcases more than twice the hardness of the other indentations in the reaction area. By comparing the graph and the optical micrograph, it can be seen that this indentation is on a dark particle observed in the interface. These particles were previously recognized as silicon particles. Thus, it would imply that this hardness represents hardness of a silicon particle. For Casting 44, the hardness measured in the reaction area is slightly lower than that measured in Casting 43. Although dark particles also were observed in this casting, the density appears to be lower which could explain the comparatively reduced hardness.

6.3 Discussion

6.3.1 Effect of Untreated Copper Pipes

For Casting 43 and 44, no surface treatment was used on the copper pipes, except for cleaning by ethanol prior to casting. Identical process parameters were used for the two castings. Figure 6.13 and 6.17, for Casting 43 and 44 respectively, show that no large defects could be observed in the aluminum-copper interface. However, a closer look using optical microscopy, proved formation of dissimilar interfaces for the two castings. Figure 6.14 for Casting 43 shows formation of several reaction areas due to melting of the copper pipe. A continuous gap was observed between the reaction area and the cast aluminum. As local surface melting of the copper pipe was confirmed in Table 6.5, the gap must have formed upon solidification. Binary Al-Cu phases are known as brittle, and might upon solidification due to internal stress fracture in the interface. For Casting 44, Figure 6.18 shows that a continuous reaction layer has formed on the copper surface. Some small cavities and areas of poor wetting could be seen in the interface, but compared to Casting 43, overall bonding was significantly improved. As these castings had identical process parameters, the difference in interfacial bonding could be due to the extent of the ethanol cleaning prior to casting. If the surface is improperly treated, surface contaminants could decrease wettability between the copper pipe surface and aluminum liquid.

Copper atoms diffused from the pipe surface into the aluminum liquid and caused formation of a eutectic (Al)+Al_2Cu structure, as seen in Figure 6.15 and 6.19 for Casting 43 and 44 respectively. Further growth of the binary Al_2Cu-phase has occurred on the copper pipe. In addition, an intermetallic layer formed between the Al_2Cu-phase and the copper pipe. Tavassoli et al. suggested that this formation is due to solid state phase transformation resulting in formation of more copper-rich binary phases [30]. When increasing magnification to consider the Al_2Cu/copper pipe interface, it could be seen that two separate layers had formed. However, only the composition for one of the layers could be determined in each of the castings. Composition of the layer adjacent to Al_2Cu in Casting 43, seen in Figure 6.16, coincided with the binary Al_4Cu_9 phase, whereas only copper was detected in the second layer. As contrast clearly indicates a difference between the copper pipe and the adjacent layer, it is believed that some drifting of the X-ray beam has occurred during the EDS analysis. A similar incident might have occurred in Casting 44, where Table 6.8 shows formation of binary Al_2Cu_3 in the intermetallic layer adjacent to the copper surface. In the second layer, both AlCu and Al_2Cu were detected, suggesting some drifting of the X-ray in Area 6. Although compositions of the two intermetallic layers differed for Casting 43 and 44, formation of at least two copper-rich binary phases are believed to have formed in the Al_2Cu/copper pipe interface. Hardness measured for Casting 43 and 44 in Figure 6.21 shows that values in the interface display significantly increased hardness compared to both the copper and the cast aluminum, making it likely that fracturing is more prone to occur in the interface.

Adjacent to the eutectic Al_2Cu-phase, a phase with contrast varying both from the eutectic phase and the aluminum was observed for both castings, seen in Figure 6.15 and 6.19. Area 2 in Table 6.5 for Casting 43, shows detection of magnesium in this phase. A similar composition was found for the phase in Area 1 in Table 6.7 for Casting 44. Even though the aluminum concentration dominates these two areas, it is likely that a quaternary Al-Cu-Si-Mg phase has formed. However, Area 2 in Table 6.7 shows significantly higher silicon and magnesium content. It can be suggested that upon solidification of the eutectic Al_2Cu+(Al), magnesium and silicon in the melt will diffuse towards the Al_2Cu surface. However, as the temperature is not sufficient for precipitation of Mg_2Si, magnesium and silicon will instead combine with excessive aluminum and copper and thus form a quaternary phase. Although composition varied in the analyzed areas, it is believed that the quaternary phase formed is the same throughout the interface. The differce observed in Table 6.5 and 6.7 could be due to drifting of the X-ray beam or areas analyzed exceeding the phase so that detection of adjacent elements will be included in the results.

6.3.2 Effect of Flux Coated Copper Pipes

Images of Casting 38 and 39, in Figure 6.5 and 6.8, showed areas of poor interfacial bonding between the copper pipe and the cast aluminum. Compared to Casting 43 and 44, without flux coating, the images alone showed more defects in the interface with flux coating. In addition, some interfacial areas with appearance reminiscent to spatter were observed. This was believed to be due to occurence of a reaction between the oxides on the aluminum melt and the flux coating. However, as seen in Figure 6.6 and 6.9, for Casting 38 and 39 respectively, a continuous gap separated the cast aluminum and the copper pipe. Two reaction areas were observed in Casting 38, indicating that some wetting of the copper pipe had occurred. However, these reaction areas were significantly smaller than those found for Casting 43 and 44. No reaction between the copper pipe and the cast aluminum occurred in Casting 39. This indicates that the flux coating has prevented, instead of improved, wetting of the copper surface and aluminum melt. As copper has a relatively high conductivity, which could prevent the flux coating of reacting with oxides at the aluminum melt surface.

The micrograph of Casting 38 in Figure 6.7 shows that the gap observed in the optical micrograph is not as wide as assumed. Detection of potassium and fluoride was confirmed on the gap edges, suggesting flux residue. Both the line scan in Figure 6.10 and the micrograph in Figure 6.11 show flux residue in the interface. Potassium and fluoride are salts and thus brittle. If flux remains in the interface, it will significantly reduce bonding strength and will increase the risk of fracture. In addition, areas containing flux residue also showed detection of magnesium in most cases. Takemoto et al. reported that magnesium is highly reactive towards the flux and will create compounds with both potassium and fluoride that have higher melting points than the flux, thus decreasing its efficiency and the wettability [47]. It is therefore suggested that upon casting, the flux will melt in contact with the liquid aluminum alloy and start to dissolve surface oxides. Magnesium in the melt will then diffuse towards the flux and create compounds such as MgF_2 and $KMgF_3$ as possibly observed in Area 6 in Table 6.3 for Casting 38 and Area 3 in Table 6.4 for Casting 39, respectively. However, Garcia et al. reported that for aluminum alloys containing less than 0.5wt% Mg, which is the case for A356, an addition of 2.0% Cs would be sufficient to prevent formation of detrimental magnesium compounds [48]. NOCOLOCK$^{®}$ Cs flux contains a minimum of 1.5% Cs [73], implying that formation of the observed compounds should not occur. As high magnesium concentrations were detected in the aluminum-copper interface, there is a possibility that the cesium content in the flux was insufficient which could be due to the coating layer being too thin.

Eutectic Al_2Cu+(Al) was detected in the reaction area in Casting 38, seen in Figure 6.7 and Table 6.3. Similar distribution as in Casting 43 and 44 of binary Al-Cu phases adjacent to the copper pipe was also determined. Formation of eutectic Al_2Cu+(Al) was in addition observed in the cast aluminum, showing that copper atoms had diffused into the melt upon casting and also affirming the gap formation upon solidification. A phase varying in brightness compared to both Al_2Cu and aluminum was, as with the non-flux coated castings, observed adjacent to the eutectic Al_2Cu. Area 9 in Table 6.3 shows detection of silicon and magnesium similar to that observed in Area 2 in Table 6.7 for Casting 44, thus suggesting formation of the same quaternary Al-Cu-Si-Mg phase. It is believed that this phase has formed in Casting 38 in a similar manner as proposed in the previous subsection. However, the quaternary particle detected in Area 9 is much larger than observed in both Casting 43 and 44. This could be due to flux causing magnesium to diffuse to the surface, thus allowing the phase to grow.

6.3.3 Effect of Heat Treatment

The image of the heat-treated Casting 37, seen in Figure 6.1, shows that a large part of the copper pipe has been remelted during the heat treatment, causing large cavities in the casting. As seen in the binary Al-Cu phase diagram in Figure 2.3, the eutectic temperature in the system is 548.2°C. Temperature used under solution heat treatment of Casting 37 was 540°C, which is very close to the eutectic temperature. Once the furnace temperature exceeds the eutectic temperature, both aluminum and copper will start to remelt.

The optical micrographs of Casting 37, in Figure 6.2 and 6.3, show that a dendritic structure formed in the cast aluminum. A reaction area could also be observed in Figure 6.2, where the cast aluminum melted the copper pipe. This would also indicate that the crack outside the reaction area has occurred upon solidification, as contact between the cast aluminum and the copper pipe is necessary for melting to occur. However, the reaction area differs from those observed in Casting 38, 43 and 44. No particle formation is evident. Instead, outlines of the dendritic structure can be recognized in the reaction area as well. In Figure 6.3, the dendritic structure comes to an end and transitions into the characteristic eutectic Al-Si structure, where silicon has spheroidized as an effect of the heat treatment. In the micrograph in Figure 6.4, a section of the cast aluminum with dendritic structure is shown. Area 5 in Table 6.2 represents the brighter parts seen in the dendritic structure. Compositions here would coincide with a ternary Al-Cu-Si phase. However, as no such phase has been found, it is suggested that this area is a combination of Al_2Cu, (Al) and Si. Upon melting of the copper pipe, copper atoms will diffuse and mix into the A356 alloy, thus creating a composition similar to that of a copper-rich Al-Si-Cu alloy. During solidification, dendritic growth of aluminum will occur, pushing aside copper, silicon and excessive aluminum. Silicon can remain in solid solution with copper and aluminum. Due to quenching of the remelted aluminum-copper liquid, the solidification rate will significantly increase thus preventing formation of silicon particles and the Al_2Cu-(Al) eutectic structure which was observed in the non-heat treated castings. This would also explain the transition from dendritic to Al-Si eutectic structure within Casting 37.

As with the other flux coated castings, Casting 38 and 39, the bonding quality in Casting 37 was poor. Regardless of the copper pipe melting, the remaining interface seen in Figure 6.1 showed several cavities. Although a reaction area was observed in Figure 6.2, the dendritic structure observed in the reaction area suggests that it was formed upon heat treatment. Considering the EDS analysis in Table 6.2, substantial detection of both potassium and fluoride alongside oxygen, show that flux coating remains in the interface and thus prevents bonding. However, the irregularities on the copper pipe surface indicates that the flux might have reacted with oxides on the copper surface. Area 4 in Table 6.2 shows an immense concentration of magnesium. Material composition of A356 implies 0.25-0.45wt% magnesium. Therefore, an atomic percentage of 28.67 magnesium is unexpected. However, the flux is known for causing magnesium atoms to diffuse to the surface. Formation of the dendritic structure might have increased this effect due to elements, excluding aluminum, segregating between dendrite arms. This has caused a magnesium-rich film to form on the cast aluminum surface. Although the composition does not coincide with the known quaternary $Al_5Cu_2Mg_8Si_6$ phase, it is likely that a quaternary phase has formed. This phase appears to oppose the wetting effect of the flux coating.

Hardness measurements of Casting 37, given in Figure 6.12a, was performed over an interface with dendritic structure. Compared to Figure 6.12 and 6.21, the copper pipe showed no difference in hardness which could be expected for commercially pure copper. The cast aluminum however, showed hardness almost twice of that measured for the non-heat treated castings. It can also be noted that the dendritic structure had higher hardness compared to those found for the cast aluminum in the heat treated aluminum-steel castings in Figure 4.19.

6.3.4 Formation of Silicon Particles

Formation of silicon particles was found in Casting 38, 43 and 44, showing that flux coating did not interfere with the formation. Similar for these three castings, is melting of the copper pipe surface, thus creating a reaction area. Considering micrographs in Figure 6.7, 6.15 and 6.19 for Casting 38, 43 and 44 respectively, it can be seen that silicon particles are present both in the reaction area and in the cast aluminum surface outside the crack. Divandari and Golpayegani also observed formation of silicon particles in an aluminum-copper interface [20]. They suggested that the particles formed due to the cooling effect of copper. Copper has much higher heat capacity than aluminum based on density. This would increase the cooling rate of the cast aluminum on the copper surface which might cause an undercooling effect in the interface. This could create a nucleation site for silicon. In Casting 39, no reaction area or silicon particles formed. However, the optical micrograph in Figure 6.9 shows an excessive amount of eutectic silicon in the cast aluminum adjacent to the crack. This could imply that the cooling effect causes eutectic silicon to precipitate adjacent to the copper pipe, while nucleation of silicon particles cannot occur unless contact between the cast aluminum and copper pipe is achieved. Another possible reason for the formation of silicon particles, could be the phosphorous content present in the copper. This can form Al_3P, which can act as nucleation sites for silicon.

Silicon particles were, as mentioned, also observed in the reaction area. As seen in Figure 6.16 and Table 6.6 for Casting 43, formation occurred between the binary Al_2Cu growing from the copper pipe surface and the eutectic (Al)+Al_2Cu structure found in the interface. Upon casting, copper atoms will dissolve into the aluminum melt resulting in the formation of Al_2Cu. As seen in the binary Al-Cu phase diagram in Figure 2.3, Al_2Cu has a higher melting point than the eutectic temperature. This will cause the binary phase at the copper surface to solidify first, thus creating a liquid/solid interface where undercooling can lead to nucleation of excessive silicon in the aluminum alloy. Upon further cooling to eutectic temperature, silicon particles could form and grow.

Optical micrographs for Casting 38, 43 and 44, given in Figure 6.6, 6.14 and 6.18 respectively, show that the density of silicon particles formed, recognized by the dark grey color, is higher in Casting 43 and 44. This is most likely due to a larger contact area between the cast aluminum and the copper pipe. Hardness measurements for Casting 43 in Figure 6.21 shows hardness measured for a silicon particle. This value is over twice as high as the other values in the interface, and over six times higher than that found for copper and aluminum. As hardness often is associated with brittleness, this hardness value shows the disadvantageous effect formation of silicon particles, especially large particles, will have on interfacial bonding strength.

6.4 Conclusions

Flux coating of copper pipes caused poor interfacial bonding due to formation of magnesium compounds with higher melting temperatures than the flux. This prevented removal of surface oxides and decreased wettability. Without any surface treatment, except for ethanol cleaning of the copper pipes, several reaction areas formed thus creating metallurgical bonding between the cast aluminum and the copper pipe.

A eutectic Al_2Cu+(Al) structure was found in the reaction areas. In addition, formation of various binary phases with higher copper content such as AlCu, Al_9Cu_4 and Al_2Cu_3 occurred at the copper pipe surface. Hardness measurements throughout the interface showed that the eutectic structure was harder than both the copper pipe and the cast aluminum alloy.

Heat treatment caused local melting of the copper pipe due to the temperature exceeding eutectic temperature. A dendritic structure formed in the cast aluminum in the area of the melted copper pipe. The dendritic structure showed almost twice the hardness of what was measured for the cast aluminum in the non-treated castings. Other areas in the cast aluminum showed spheroidized silicon as a result of the heat treatment.

Silicon particles formed in the reaction areas. These were believed to form as a result of the high heat capacity of copper creating an undercooling effect in the cast aluminum-copper pipe interface and the liquid/solid interface in the eutectic structure. In addition, formation of Al_3P from phosphorus existing in copper will act as nucleation sites for silicon. Hardness measured for a silicon particle was over six times higher than that of copper and cast aluminum.

Chapter 7

Overall Conclusions and Future Prospects

Through characterization of both the aluminum-copper and the aluminum-steel interface, metallurgical bonding is possible to achieve using a compound casting process. However, surface treatment and temperature have significant effect on the properties in the interface.

The interfacial microstructure varied in different sections within a casting. This showed that local temperature variations which arise during the casting process, will affect the final microstructure. Better detection of the temperature at the interface is therefore suggested as a way of more precisely determining optimal pouring temperature of the liquid aluminum alloy.

In terms of surface treatment, the combination of a galvanized layer and flux coating showed improved bonding results in the low pressure die casting of A356 on steel pipes. No surface treatment showed poor bonding and high detection of oxygen in the interface. A thin zinc-layer on the steel pipes caused a thinner reaction layer, which overall will improve bonding strength due to less brittle intermetallic phases forming. Combining the zinc-layer, which also showed porsities, with flux coating, prevented continuous bonding as flux residue remained in the interface. A combination of flux coating and a thin galvanized layer could therefore be tested in a new casting experiment, in order to obtain a thinner reaction layer with proper wetting and thus improved bonding ability.

The brittle ternary $Al_{4.5}FeSi$-phase was found in the aluminum-steel interface both for the low pressure die casting process and in the lab scale shape casting experiment. Lengths of the particles varied, with the shortest particles being observed in the casting with the lowest metal pouring temperature. Formation of these particles can severely reduce interfacial strength. A suggested method to decrease the formation of the ternary phase is to increase the cooling rate. When heat treatment was applied subsequent to casting, no $Al_{4.5}FeSi$ was observed. Instead, a brittle Al_3Fe-layer formed on the steel surface, which resulted in higher hardness. Therefore, heat treatment using the T6 process is not recommended for these castings.

In the lab scale shape casting experiment, mainly mechanical bonding could be achieved between the cast aluminum and the steel insert. This was due to insufficient temperature of the steel inserts, causing the cast aluminum to rapidly solidify upon contact. A new experiment could therefore be conducted, where steel inserts with various thickness and preheating temperature are used. This way, the preheating temperature necessary for metallurgical bonding to occur for each thickness of the steel insert can be determined. In addition, argon gas flushed into the mold prior to casting was found to improve bonding. However, some entrapped gas was still observed in the aluminum-steel interface. To improve bonding further, a constant flush of argon throughout the casting process should be tested.

For the bimetallic aluminum-copper castings created under the low pressure die casting process, flux coating caused poor interfacial bonding. This was due to the formation of magnesium compounds with high melting points preventing further flux reaction. Instead, flux residue remained in the interface. Without surface treatment, bonding was achieved between the cast aluminum and the copper pipe. A eutectic Al_2Cu+(Al) structure formed in the interface. This showed higher hardness than both the cast aluminum and the copper pipe. Heat treatment caused local melting of the copper pipe, due to the temperature exceeding eutectic temperature. A different heat treatment process should therefore be used.

Several silicon particles also formed in the aluminum-copper interface. Hardness measured for a particle was over six times higher than that of both copper and cast aluminum. Formation of large silicon particles will therefore decrease bonding strength. It can be suggested to also increase cooling rate during the aluminum-copper casting process, as it might cause reduced growth of the particles. In addition, due to copper showing good bonding properties with A356, copper should be investigated as a possible coating of steel instead of a galvanization layer. This bond will possibly show improved conductivity properties compared to zinc, which could be beneficial in vehicle construction.

Bibliography

[1] V. D. G., D. Zhou, E. H. M. Ahmed, P. K. Dadhich, J. G. J. Olivier, H.-H. Rogner, K. Sheikho, and M. Yamaguchi, "Introductory Chapter," in *Climate Change 2014: Mitigation of Climate Change. Contribution of Working Group III to the Fifth Assessment Report of the Intergovernmental Panel on Climate Change*, O. Edenhofer, R. Pichs-Madruga, Y. Sokona, E. Farahani, S. Kadner, K. Seyboth, A. Adler, I. Baum, S. Brunner, P. Eickemeier, B. Kriemann, J. Savolainen, S. Schlömer, C. von Stechow, T. Zwickel, and J. C. Minx, Eds., Cambridge, United Kingdom and New York, NY, USA: Cambridge University Press, 2014, ch. 1, pp. 115–124.

[2] The Council of the European Union and The European Parliament, "DIRECTIVE 2009/30/EC OF THE EUROPEAN PARLIAMENT AND OF THE COUNCIL," *Official Journal of the European Union*, vol. L 140, no. April, pp. 88–113, 2009.

[3] W. Miller, L. Zhuang, J. Bottema, A. Wittebrood, P. De Smet, A. Haszler, and A. Vieregge, "Recent development in aluminium alloys for the automotive industry," *Materials Science and Engineering: A*, vol. 280, no. 1, pp. 37–49, 2000.

[4] R. Kumar Tayal, V. Singh, S. Kumar, and R. Garg, "Compound Casting - a Literature Review," 2012.

[5] K. J. M. Papis, J. F. Loeffler, and P. J. Uggowitzer, "Light metal compound casting," *Science in China, Series E: Technological Sciences*, vol. 52, no. 1, pp. 46–51, 2009.

[6] J. G. Kaufman and E. L. Rooy, "Aluminum Casting Alloys," in *Aluminum Alloy Castings - Properties, Processes, and Applications*, ASM International, 2004, ch. 2, pp. 7–10.

[7] J. K. Solberg, *Teknologiske Metaller Og Legeringer.* Trondheim: Norges Teknisk-naturvitenskapelige Universitet, 2014.

[8] D. Apelian, *Aluminum Cast Alloys: Enabling Tools for Improved Performance*. Wheeling, Illinois: North American Die Casting Association, 2009, pp. 5–17.

[9] H. Baker and H. Okamoto, "Binary Alloy Phase Diagrams," in *ASM Handbook, Volume 03 - Alloy Phase Diagrams*, ASM International, 1992, ch. 2, p. 206.

[10] X. Jian and Q. Han, “Formation of hypereutectic silicon particles in hypoeutectic Al-Si alloys under the influence of high-intensity ultrasonic vibration,” *China Foundry*, vol. 10, no. 2, pp. 118–123, 2013.

[11] H. Baker and H. Okamoto, “Binary Phase Diagrams,” in *ASM Handbook, Volume 03 - Alloy Phase Diagrams*, ASM International, 1992, ch. 2, p. 52.

[12] S. R. Wang, R. Ma, Y. Z. Wang, Y. Wang, and L. Y. Yang, “Growth mechanism of primary silicon in cast hypoeutectic Al-Si alloys,” *Transactions of Nonferrous Metals Society of China (English Edition)*, vol. 22, no. 6, pp. 1264–1269, 2012.

[13] H. Springer, A. Kostka, E. J. Payton, D. Raabe, A. Kaysser-Pyzalla, and G. Eggeler, “On the formation and growth of intermetallic phases during interdiffusion between low-carbon steel and aluminum alloys,” *Acta Materialia*, vol. 59, no. 4, pp. 1586–1600, 2011.

[14] G. Aylward and T. Findlay, *SI chemical data*, 5th. Milton: John Wiley & Sons Australia, 2002.

[15] Hadleighs Casting, “A356.0 Aluminum Casting Alloy (7Si-0.3Mg),” *Hadleigh Casting*, pp. 3–4, 2012.

[16] W. Jiang, Z. Fan, and C. Li, “Improved steel/aluminum bonding in bimetallic castings by a compound casting process,” *Journal of Materials Processing Tech.*, vol. 226, pp. 25–31, 2015.

[17] W. Jiang, Z. Fan, G. Li, and C. Li, “Effects of zinc coating on interfacial microstructures and mechanical properties of aluminum/steel bimetallic composites,” *Journal of Alloys and Compounds*, vol. 678, pp. 249–257, 2016.

[18] T. Liu, Q. Wang, Y. Sui, Q. Wang, and W. Ding, “An investigation into interface formation and mechanical properties of aluminum-copper bimetal by squeeze casting,” *Materials and Design*, vol. 89, pp. 1137–1146, 2016.

[19] G. R. Zare, M. Divandari, and H. Arabi, “Investigation on interface of Al/Cu couples in compound casting,” *Materials Science and Technology*, vol. 29, no. 2, pp. 190–196, 2013.

[20] M. Divandari and A. R. Vahid Golpayegani, “Study of Al/Cu rich phases formed in A356 alloy by inserting Cu wire in pattern in LFC process,” *Materials and Design*, vol. 30, no. 8, pp. 3279–3285, 2009.

[21] K. J. M. Papis, B. Hallstedt, J. F. Löffler, and P. J. Uggowitzer, “Interface formation in aluminium-aluminium compound casting,” *Acta Materialia*, vol. 56, no. 13, pp. 3036–3043, 2008.

[22] B. J. J. Zelinski, J. P. Cronin, M. Denesuk, and D. R. Uhlmann, “High-Temperature Wetting Behavior of Inorganic Liquids,” in *Wettability*, J. C. Berg, Ed., New York: Marcel Dekker, INC., 1993, ch. 8, pp. 465–498.

[23] M. Pinnel, H. Tompkins, and D. Heath, “Oxidation of copper in controlled clean air and standard laboratory air at 50°C to 150°C,” *Applications of Surface Science*, vol. 2, no. 4, pp. 558–577, May 1979.

[24] T. Kawano and F. U. Renner, “Tailoring Model Surface and Wetting Experiment for a Fundamental Understanding of Hot-dip Galvanizing,” *ISIJ International*, vol. 51, no. 10, pp. 1703–1709, 2011.

[25] N. Ebrill, Y. Durandet, and L. Strezov, “Dynamic reactive wetting and its role in hot dip coating of steel sheet with an Al-Zn-Si alloy,” *Metallurgical and Materials Transactions B*, vol. 31, no. October, pp. 1069–1079, 2000.

[26] A. P. Savitskii, “Diffusion Interaction between Two Metals, One of Which is in Liquid State,” *Materials Science Forum*, vol. 575-578, pp. 1477–1482, 2008.

[27] B. Hallstedt, J. Gröbner, M. Hampl, and R. Schmid-Fetzer, “Calorimetric measurements and assessment of the binary Cu–Si and ternary Al–Cu–Si phase diagrams,” *Calphad*, vol. 53, pp. 25–38, 2016.

[28] “Phase Diagrams,” in *ASM Specialty Handbook - Copper and Copper Alloys*, J.R Davis and Davis & Associates, Eds., Materials Park, Ohio: ASM International, 2001, ch. 23, p. 370.

[29] Y. Wei, J. Li, J. Xiong, and F. Zhang, “Investigation of interdiffusion and intermetallic compounds in Al–Cu joint produced by continuous drive friction welding,” *Engineering Science and Technology, an International Journal*, vol. 19, no. 1, pp. 90–95, 2016.

[30] S. Tavassoli, M. Abbasi, and R. Tahavvori, “Controlling of IMCs layers formation sequence, bond strength and electrical resistance in Al/Cu bimetal compound casting process,” *Materials and Design*, vol. 108, pp. 343–353, 2016.

[31] D. Moreno, J. Garrett, and J. D. Embury, “Technique for rapid characterization of intermetallics and interfaces,” *Intermetallics*, vol. 7, no. 9, pp. 1001–1009, 1999.

[32] E. Hug and N. Bellido, “Brittleness study of intermetallic (Cu, Al) layers in copper-clad aluminium thin wires,” *Materials Science and Engineering: A*, vol. 528, no. 22, pp. 7103–7106, 2011.

[33] U. Kattner and T. Massalski, *Binary Alloy Phase Diagram*, H. Baker, Ed. Material Park, OH: ASM International, 1990, p. 147.

[34] S. Kobayashi and T. Yakou, “Control of intermetallic compound layers at interface between steel and aluminum by diffusion-treatment,” *Materials Science and Engineering A*, vol. 338, no. 1-2, pp. 44–53, 2002.

[35] H. Springer, A. Kostka, J. F. dos Santos, and D. Raabe, “Influence of intermetallic phases and Kirkendall-porosity on the mechanical properties of joints between steel and aluminium alloys,” *Materials Science and Engineering A*, vol. 528, no. 13-14, pp. 4630–4642, 2011.

[36] K. Bouché, F. Barbier, and A. Coulet, “Intermetallic compound layer growth between solid iron and molten aluminium,” *Materials Science and Engineering: A*, vol. 249, no. 1-2, pp. 167–175, 1998.

[37] W. J. Cheng and C. J. Wang, “Effect of silicon on the formation of intermetallic phases in aluminide coating on mild steel,” *Intermetallics*, vol. 19, no. 10, pp. 1455–1460, 2011.

[38] T. Maitra and S. P. Gupta, “Intermetallic compound formation in Fe-Al-Si ternary system: Part II,” *Materials Characterization*, vol. 49, no. 4, pp. 293–311, 2003.

[39] S. Liu, F. Weitzer, J. C. Schuster, N. Krendelsberger, and Y. Du, “On the reaction scheme and liquidus surface in the ternary system Al-Si-Ti,” *International Journal of Materials Research*, vol. 99, no. 7, pp. 705–711, 2008.

[40] J. A. Taylor, “The Effect of Iron in Al-Si Casting Alloys,” *35th Australian Foundry Institute National Conference*, no. October 2004, pp. 148–157, 2004.

[41] S. Seifeddine, S. Johansson, and I. L. Svensson, “The influence of cooling rate and manganese content on the β-Al5FeSi phase formation and mechanical properties of Al-Si-based alloys,” *Materials Science and Engineering A*, vol. 490, no. 1-2, pp. 385–390, 2008.

[42] Z. Ma, A. M. Samuel, F. H. Samuel, H. W. Doty, and S. Valtierra, “A study of tensile properties in Al-Si-Cu and Al-Si-Mg alloys: Effect of β-iron intermetallics and porosity,” *Materials Science and Engineering A*, vol. 490, no. 1-2, pp. 36–51, 2008.

[43] S. G. Shabestari, “The effect of iron and manganese on the formation of intermetallic compounds in aluminum-silicon alloys,” *Materials Science and Engineering A*, vol. 383, no. 2, pp. 289–298, 2004.

[44] E. T. Akinlabi, E. Ogunmuyiwa, and S. A. Akinlabi, “Characterising the Effects of Sand Blasting on Formed Steel Samples,” *International Journal of Mechanical, Aerospace, Industrial and Mechatronics Engineering*, vol. 7, no. 11, pp. 1135–1138, 2013.

[45] P. Bansal and R. Gandhi, “Aspects of Shot Blasting Over Pickling for Metal,” *International Journal of Mechanical And Production Engineering*, vol. 2, no. 6, pp. 26–29, 2014.

[46] R. W. Gunkel, L. L. Podey, and T. N. Meyer, *Fluxing agent for metal cast joining*, 2002.

[47] T. Takemoto, A. Matsunawa, and T. Shibutani, “Chemical reaction of non-corrosive flux with magnesium containing aluminium alloys and the improvement of brazeability,” *Welding International*, vol. 1, no. 11, pp. 845–851, 1997.

[48] J. Garcia, C. Massoulier, and P. Faille, “Brazeability of Aluminum Alloys Containing Magnesium by CAB Process Using Cesium Flux,” *Society of Automotive Engineers*, pp. 1–11, 2001.

[49] N. L. Okamoto, D. Kashioka, M. Inomoto, H. Inui, H. Takebayashi, and S. Yamaguchi, “Compression deformability of Γ and ζ Fe-Zn intermetallics to mitigate detachment of brittle intermetallic coating of galvannealed steels,” *Scripta Materialia*, vol. 69, no. 4, pp. 307–310, 2013.

[50] S. Sepper, P. Peetsalu, P. Kulu, M. Saarna, and V. Mikli, “The role of silicon in the hot dip galvanizing process,” *Proceedings of the Estonian Academy of Sciences*, vol. 64, no. 3, pp. 1–9, 2015.

[51] P. Pokorny, J. Kolisko, L. Balik, and P. Novak, “Description of structure of Fe-Zn intermetalic compounds present in hot-dip galvanized coatings on steel,” *Metalurgija*, vol. 54, no. 4, pp. 707–710, 2015.

[52] P. R. Munroe, C. S. Laksmi, and B. Gleeson, “Effects of 0.1 and 0.2 wt.% aluminium addition to zinc on the interdiffusion between zinc and iron at 400°C,” *Materials Science and Engineering A*, vol. 251, pp. 87–93, 1998.

[53] P. Pokorny, J. Kolisko, L. Balik, and P. Novak, “Reaction Kinetics of the Formation of Intermetallic Fe–Zn During Hot-dip Galvanizing of Steel,” vol. 55, no. 1, pp. 111–114, 2016.

[54] J. G. Kaufman and E. L. Rooy, “Heat Treatment of Aluminum Castings,” in *Aluminum Alloy Castings - Properties, Processes, and Applications*, ASM International, 2004, ch. 7, pp. 61–68.

[55] M. Abou El-khair, “Microstructure characterization and tensile properties of squeeze-cast AlSiMg alloys,” *Materials Letters*, vol. 59, no. 8, pp. 894–900, 2005.

[56] K. A. Ragab, M. Bournane, A. M. Samuel, A. M. A. Al-Ahmari, F. H. Samuel, and H. W. Doty, “Mechanical characterisation and quality index of A356-type aluminium castings heat treated using fluidised bed quenching,” *Materials Science and Technology*, vol. 29, no. 4, pp. 412–425, 2013.

[57] L. Pedersen and L. Arnberg, “The Effect of Solution Heat Treatment and Quenching Rates.pdf,” *Metallurgical and Materials Transactions A*, vol. 32A, no. March, p. 525, 2001.

[58] Y. Birol, “Response to artificial ageing of dendritic and globular Al-7Si-Mg alloys,” *Journal of Alloys and Compounds*, vol. 484, no. 1-2, pp. 164–167, 2009.

[59] M. Zhe, O. Dezellus, B. Gardiola, M. Braccini, and J. C. Viala, “Chemical changes at the interface between low carbon steel and an Al-Si alloy during solution heat treatment,” *Journal of Phase Equilibria and Diffusion*, vol. 32, no. 6, pp. 486–497, 2011.

[60] P. Aloke, T. Laurila, V. Vuorinen, and S. V. Divinski, “Interdiffusion and the Kirkendall Effect in Binary Systems,” in *Thermodynamics, Diffusion and the Kirkendall Effect in Solids*, Springer International Publishing, 2014, ch. 6, pp. 239–298.

[61] C.-Y. Chen and W.-S. Hwang, “Effect of Annealing on the Interfacial Structure of Aluminum-Copper Joints,” *Materials Transactions*, vol. 48, no. 7, pp. 1938–1947, 2007.

[62] C.-Y. Chen, H.-L. Chen, and W.-S. Hwang, “Influence of Interfacial Structure Development on the Fracture Mechanism and Bond Strength of Aluminum/Copper Bimetal Plate,” *Materials Transactions*, vol. 47, no. 4, pp. 1232–1239, 2006.

[63] W.-B. Lee, K.-S. Bang, and S.-B. Jung, “Effects of intermetallic compound on the electrical and mechanical properties of friction welded Cu/Al bimetallic joints during annealing,” *Journal of Alloys and Compounds*, vol. 390, no. 1, pp. 212–219, 2005.

[64] L. Y. Sheng, F. Yang, T. F. Xi, C. Lai, and H. Q. Ye, “Influence of heat treatment on interface of Cu/Al bimetal composite fabricated by cold rolling,” *Composites Part B: Engineering*, vol. 42, no. 6, pp. 1468–1473, 2011.

[65] R. F. Egerton, “The Scanning Electron Microscope,” in *Physical Principles of Electron Microscopy - An Introduction to TEM, SEM, and AEM*, Springer US, 2005, ch. 5, pp. 125–153.

[66] J. Hjelen, *Scanning elektron-mikroskopi*. Trondheim: SINTEF, Avdeling for metallurgi, Metallurgisk institutt, NTH, 1986.

[67] R. F. Egerton, “Analytical Electron Microscopy,” in *Physical Principles of Electron Microscopy - An Introduction to TEM, SEM, and AEM*, Springer US, 2005, ch. 6, pp. 155–175.

[68] J. R. Davis and ASM International. Handbook Committee., *Metals handbook*. ASM International, 1998.

[69] K. Herrmann, “The fundamentals of hardness testing,” in *Hardness testing - Principles and Applications*, K. Herrmann, Ed., ASM International, 2010, ch. 1, pp. 1–24.

[70] F. Campbell, “Hardness testing,” in *Inspection of metals*, F. Campbell, Ed., ASM International, 2013, ch. 5, pp. 85–116.

[71] J. Pelleg, “Mechanical Testing of Materials,” in *Mechanical Properties of Materials*, Springer Netherlands, 2013, ch. 1, pp. 1–84.

[72] T. Polzin, “Hardness Measurements of Metals - Static Methods,” in *Hardness testing - Principles and Applications*, K. Herrmann, Ed., ASM International, 2010, ch. 2, pp. 25–65.

[73] Solvay Fluor GmbH, *NOCOLOK Cs flux product information*. [Online]. Available: `http://www.solvay.com/en/binaries/NOCOLOK_Cs_Flux-product-information-179822.pdf`.

[74] MatWeb Material Property Data, *ASTM A283 Steel, grade A*. [Online]. Available: `http://matweb.com/search/DataSheet.aspx?MatGUID=67e1b53cedc944b19ae5a9d46cef3096`.

[75] MatWeb Material Property Data, *ASTM A284 Steel, grade C*. [Online]. Available: `http://matweb.com/search/DataSheet.aspx?MatGUID=045930e40a0f43ec8b0935acd039761d`.

[76] Ovako, *Material data sheet Steel grade S355J2*, 2017. [Online]. Available: `https://steelnavigator.ovako.com/steel-grades/s355j2/?acceptCookies=true&variantIDs=246`.

Appendix A

Results from Casting 40, 42 and 45 are presented in summary in this appendix. Process parameters for the castings are given in Table 6.1.

Casting 40

An image of Casting 40 after grinding and polishing is shown in Figure 7.1a. A closer look at the aluminum-copper interface can be seen in the optical micrograph in Figure 7.1b.

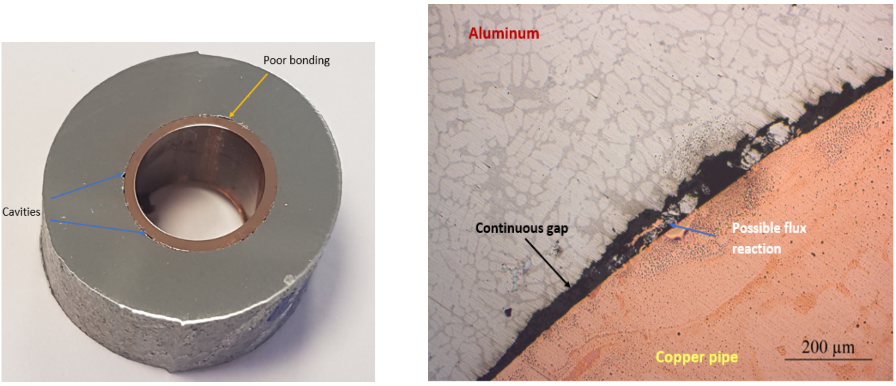

(a) (b)

Figure 7.1: Images of Casting 40.
(**a**) Image of Casting 40 after grinding and polishing. A yellow arrow shows an area of poor bonding, whereas interfacial cavities are indicated by a blue arrow.
(**b**) Optical micrograph of the aluminum-copper interface in Casting 40. A continuous gap can be seen between the cast aluminum and copper pipe, indicated by a black arrow. An area of possible flux reaction is shown by a blue arrow.

In Figure 7.1a interfacial cavities are shown by a blue arrow, whereas an area of poor bonding is indicated by a yellow arrow. A continuous gap has formed between the cast aluminum and the copper pipe, as indicated by the black arrow in Figure 7.1b. Similar observations were made for Casting 39 in Figure 6.9. An area where a flux reaction might have occurred is shown by the blue arrow. Further detection of the possible flux reaction was made using SEM and EDS. Red circled areas in the micrograph in Figure 7.2 were analyzed using EDS. Results of the analysis are presented in Table 7.1.

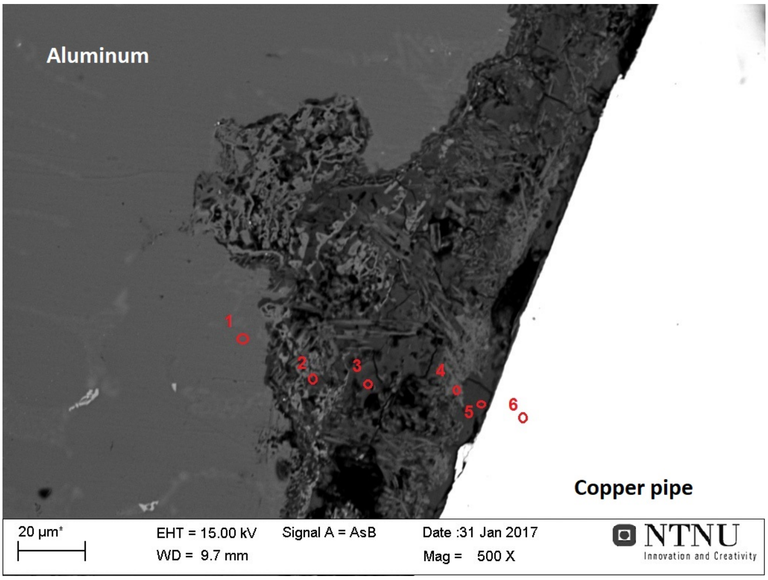

Figure 7.2: Micrograph of the aluminum-copper interface in Casting 40. Red circled areas were analyzed using EDS. Results of the analysis are presented in Table 7.1.

Table 7.1: Compositions and possible phases formed across the aluminum-copper interface in Casting 40 given in Figure 7.2, analyzed using EDS.

Area	Composition [at%]							Possible phase
	Al	Cu	Mg	K	Cs	F	O	
1	100	-	-	-	-	-	-	(Al)
2	18.87	-	10.08	8.74	1.30	47.97	13.05	Flux residue
3	24.65	-	-	4.58	-	44.88	25.89	Flux residue
4	25.61	0.63	2.79	21.58	-	42.74	6.65	Flux residue
5	24.25	0.29	-	3.82	-	45.04	26.40	Flux residue
6	-	100	-	-	-	-	-	Cu

Compositions found in Table 7.1 show that, as for Casting 38 and 39, large amounts of flux residue remain in the aluminum-copper interface. The micrograph in Figure 7.2 indicates that a reaction between the flux and the cast aluminum has occurred based on the observed structure.

Casting 42

An image of Casting 42 after grinding and polishing is shown in Figure 7.3.

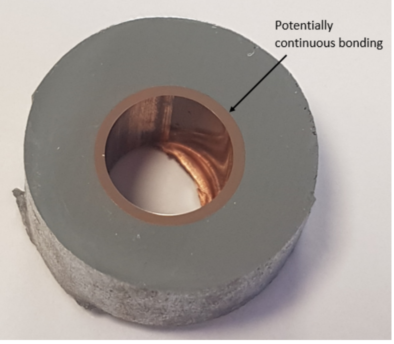

Figure 7.3: Image of Casting 42 after grinding and polishing. No defects were observed in the interface, instead potentially continouos bonding was observed, as indicated by the black arrow.

As with Casting 44, no defects are macroscopically visible in the aluminum-copper interface of Casting 42, seen in Figure 7.3. Instead, a potentially continuous bond has formed. Further investigation of the interface can be seen in the optical micrograph in Figure 7.4.

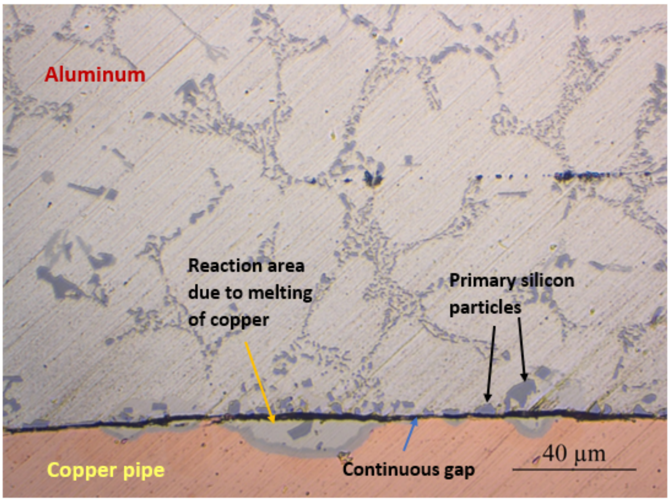

Figure 7.4: Optical micrograph of the aluminum-copper interface in Casting 42. A reaction area due to melting of the copper pipe is indicated by a yellow arrow. Between the reaction area and cast aluminum, a gap has formed that continues on the copper surface, shown by the blue arrow. Primary silicon particles were also observed, shown by the black arrows.

The interface in Figure 7.4 shows formation of reaction areas due to local melting of the copper pipe surface. One of these areas is indicated by a yellow arrow. A gap can be observed between the copper pipe and the cast aluminum, noted by the blue arrow. As the gap separates the reaction area and the cast aluminum, it is believed to have occurred upon solidification. Dark particles were recognized as silicon particles and were also found adjacent to the reaction areas in Casting 43 and 44. These are shown by the black arrows.

A micrograph of the reaction area is given in Figure 7.5. Red circled areas were analyzed using EDS. Results of the analysis are given in Table 7.2.

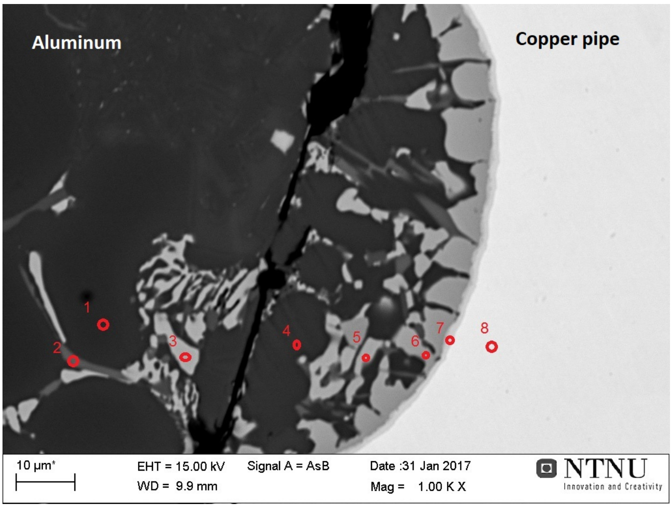

Figure 7.5: Micrograph of the aluminum-copper interface in Casting 42. Red circled areas were analyzed using EDS. Results of the analysis are presented in Table 7.2.

Table 7.2: Compositions and possible phases formed across the aluminum-copper interface in Casting 42 given in Figure 7.5, analyzed using EDS.

Area	Composition [at%]				Possible phase
	Al	Cu	Si	Mg	
1	99.06	0.94	-	-	(Al)
2	49.41	20.93	6.39	23.26	Al-Cu-Si-Mg phase
3	69.99	30.01	-	-	Al_2Cu
4	98.12	1.88	-	-	(Al)
5	83.86	16.14	-	-	Eutectic Al_2Cu + (Al)
6	69.71	24.49	5.80	-	Eutectic Al_2Cu + (Al)
7	-	100	-	-	Cu
8	-	100	-	-	Cu

Figure 7.5 and Table 7.2 show that the previously observed eutectic Al_2Cu + (Al) structure, also formed in Casting 42. In addition, a quaternary Al-Cu-Si-Mg phase formed adjacent to the eutectic Al_2Cu, as observed in Casting 43 and 44.

Casting 45

An image of Casting 45 after grinding and polishing is shown in Figure 7.6.

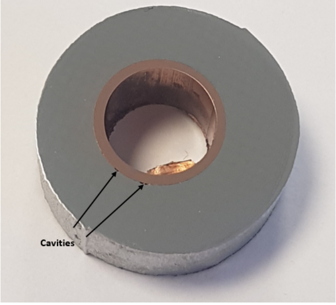

Figure 7.6: Image of Casting 45 after grinding and polishing. Small cavities were observed in the interface, as shown by the black arrow.

Figure 7.6 shows that overall the interface of Casting 45 displays good bonding, except for some small cavities indicated by the black arrow. Further investigation of the interface can be observed in the optical micrograph in Figure 7.7.

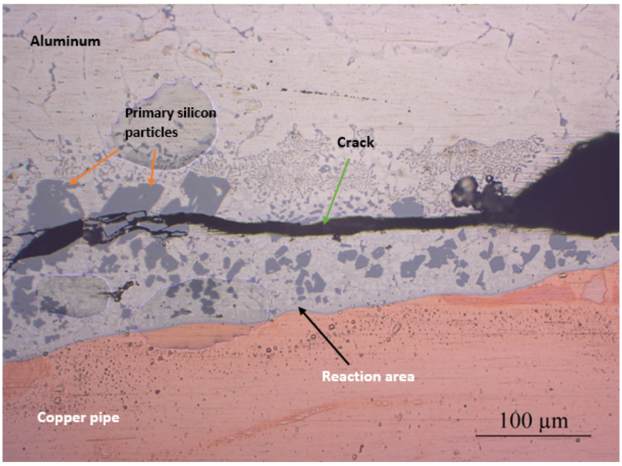

Figure 7.7: Optical micrograph of the aluminum-copper interface in Casting 45.

A reaction area has occurred in Casting 45, as seen by the black arrow in Figure 7.7. A similar reaction area was also observed in Casting 44. Large dark particles, shown by the orange arrows, are recognized as silicon particles. A crack, indicated by a green arrow, propagates through the area of the large silicon particles. This is most likely due to their brittleness as seen from the hardness measurements in Casting 43.

A micrograph of the reaction area is given in Figure 7.8. Red circled areas were analyzed using EDS. Results of this analysis is presented in Table 7.3.

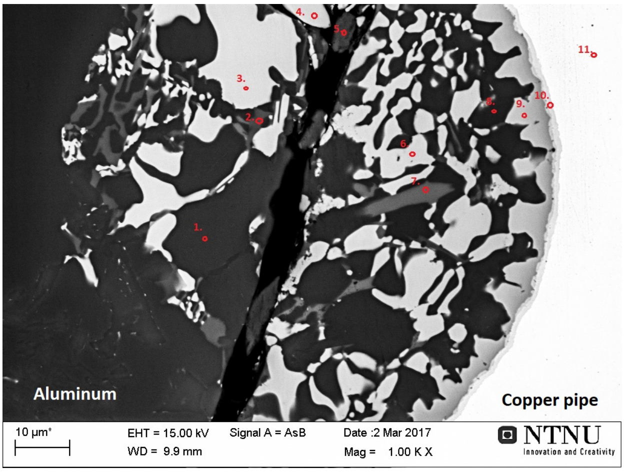

Figure 7.8: Micrograph of the aluminum-copper interface in Casting 45. Red circled areas were analyzed using EDS. Results of the analysis are presented in Table 7.3.

Table 7.3: Compositions and possible phases formed across the aluminum-copper interface in Casting 45 given in Figure 7.8, analyzed using EDS.

Area	Composition [at%]					Possible phase
	Al	Cu	Si	Mg	O	
1	98.35	1.65	-	-	-	(Al)
2	66.26	25.40	4.38	3.96	-	Al-Cu-Si-Mg phase
3	69.79	28.35	1.86	-	-	Al_2Cu
4	69.17	-	4.25	5.02	8.45	(Al)
5	76.91	0.93	4.23	-	17.93	(Al) + O
6	75.12	24.88	-	-	-	Al_2Cu
7	96.47	1.81	1.72	-	-	(Al)
8	70.29	3.41	21.08	5.21	-	Al-Cu-Si-Mg phase
9	70.04	29.96	-	-	-	Al_2Cu
10	39.24	60.76	-	-	-	Al_2Cu_3
11	-	100	-	-	-	Cu

Table 7.3 shows that the eutectic Al_2Cu+(Al) structure was observed in the reaction area, as in Casting 43 and 44. Adjacent to the copper pipe, Al_2Cu_3 formed. Quaternary Al-Cu-Si-Mg phases with various compositions formed adjacent to the eutectic Al_2Cu-phase. These observations were also made for Casting 43. Area 4 and 5 show detection of oxygen, believed to be due to the close proximity to the crack.

Hardness measurements
Hardness measurements for Casting 40, 42 and 45 are shown in Figure 7.9. Precise measurements are given in Appendix B.

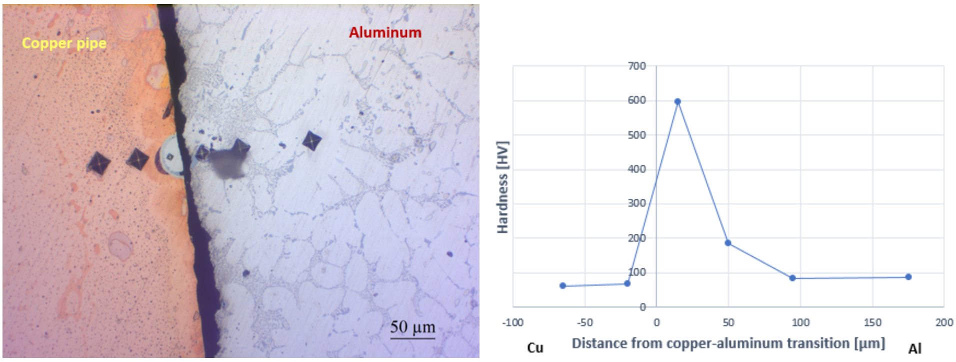

(a) Vickers hardness measured in the interface of Casting 40. Copper-aluminum transition is set as transition from copper pipe to reaction area.

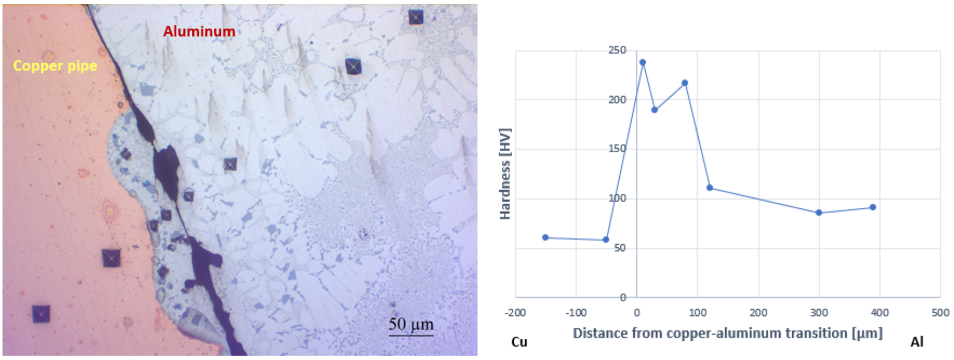

(b) Vickers hardness measured in the interface of Casting 42. Copper-aluminum transition is set as transition from copper pipe to reaction area.

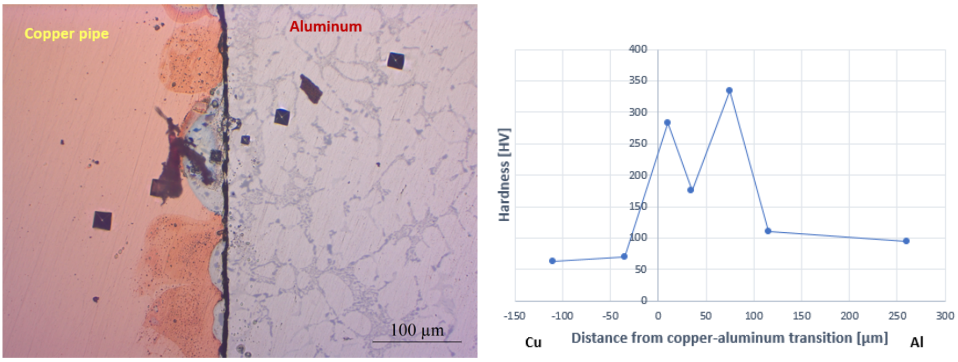

(c) Vickers hardness measured in the interface of Casting 45. Copper-aluminum transition is set as transition from copper pipe to reaction area.

Figure 7.9: Vickers hardness measured across the aluminum-copper interface in Casting 40, 42 and 45.

Appendix B

Hardness measurements across the interface of the low pressure die cast aluminum A356-steel and aluminum A356-copper are presented in this appendix. Hardness for each section is presented by order of appearance.

Hardness Measurements From Low Pressure Die Cast Aluminum A356-Steel

Hardness measurements across the steel-aluminum interface in Casting 17 and 32 are presented in Table 7.4 and 7.5, respectively.

Table 7.4: Micro-hardness measured across the interface in Casting 17.

Distance from the steel-Al transition [μm]	Hardness [HV]
-80	158
-50	161
-10	217
15	50.4
60	67.3
100	69.4

Table 7.5: Micro-hardness measured across the interface in Casting 32.

Distance from the steel-Al transition [μm]	Hardness [HV]
-130	164
-60	165
-10	151
10	836
25	1187
55	800
70	676
95	348
135	157
165	295
275	129
370	115

Hardness measured across the interface in Casting 15 and 16 are presented in Table 7.6 and 7.7, respectively. Optical micrographs of the measured interfaces are shown in Figure 4.19.

Table 7.6: Micro-hardness measured across the interface in Casting 15.

Distance from the steel-Al transition [μm]	Hardness [HV]
-130	153
-80	152
-30	166
5	1083
20	1165
45	786
50	534
100	107
130	96.8

Table 7.7: Micro-hardness measured across the interface in Casting 16.

Distance from the steel-Al transition [μm]	Hardness [HV]
-85	169
-50	156
-25	176
5	211
50	73.4
95	83.8
135	79.9

Hardness measurements across two different sections of the interface in Casting 14 are presented in Table 7.8 and 7.9, while measurements for Casting 28 are presented in Table 7.10. These interfaces are shown in Figure **??**.

Table 7.8: Micro-hardness measured across a section of the interface Casting 14 where the galvanized layer remained unmelted.

Distance from the steel-Al transition [μm]	Hardness [HV]
-235	172
-180	163
-125	188
-80	329
-55	203
-20	170
35	115
85	112
135	103

Table 7.9: Micro-hardness measured across a section of the interface Casting 14 where the galvanized layer melted.

Distance from the steel-Al transition [μm]	Hardness [HV]
-120	163
-70	159
-30	187
35	298
75	248
115	268
175	80.4
245	79.9
310	82.1

Table 7.10: Micro-hardness measured across a section of the interface in Casting 28 where the galvanized layer melted.

Distance from the steel-Al transition [μm]	Hardness [HV]
-130	163
-60	165
-20	167
20	284
45	454
110	132
180	203
260	107
315	105

Hardness Measurements From Low Pressure Die Cast Aluminum A356-Copper

Hardness measurements across the aluminum-copper interface of Casting 37, 38 and 39 are presented in Table 7.11, 7.12 and 7.13 respectively. Optical micrographs of these interfaces are shown in Figure 6.12.

Table 7.11: Micro-hardness measured across the interface in Casting 37.

Distance from the Cu-Al transition [μm]	Hardness [HV]
-120	60.2
-10	45.2
40	254
65	219
110	228
210	231
550	264

Table 7.12: Micro-hardness measured across the interface in Casting 38.

Distance from the Cu-Al transition [μm]	Hardness [HV]
-140	62.5
-40	64.7
20	272
45	231
80	238
125	274
170	123
310	90.2

Table 7.13: Micro-hardness measured across the interface in Casting 39.

Distance from the Cu-Al transition [μm]	Hardness [HV]
-120	60.2
-10	45.2
40	254
65	219
110	228
210	231
550	264

Hardness measurements across the interface in Casting 43 and 44 are presented in Table 7.14 and 7.15. Optical micrographs of the interfaces are shown in Figure 6.21.

Table 7.14: Micro-hardness measured across the interface in Casting 43.

Distance from the Cu-Al transition [μm]	Hardness [HV]
-100	57.0
-25	60.2
15	311
50	318
100	1033
140	329
195	72.6
285	70.3

Table 7.15: Micro-hardness measured across the interface in Casting 44.

Distance from the Cu-Al transition [μm]	Hardness [HV]
-110	58.1
-35	60.4
10	233
45	175
80	89.8
175	84.6

Hardness measured across the interface of Casting 40, 42 and 45 are presented in Table 7.16, 7.17 and 7.18 respectively.

Table 7.16: Micro-hardness measured across the interface in Casting 40.

Distance from the Cu-Al transition [μm]	Hardness [HV]
-65	62.6
-20	66.7
15	597
50	186
95	85.2
175	85.6

Table 7.17: Micro-hardness measured across the interface in Casting 42.

Distance from the Cu-Al transition [μm]	Hardness [HV]
-150	60.4
-50	58.2
10	238
30	190
80	217
120	111
300	85.6
390	91.6

Table 7.18: Micro-hardness measured across the interface in Casting 45.

Distance from the Cu-Al transition [μm]	Hardness [HV]
-110	62.7
-35	69.6
10	283
35	176
75	334
115	110
260	94.2